Multichannel Analysis of Medium Grazing Angle Sea Clutter for Airborne Microwave Radar Systems

DISSERTATION
zur Erlangung des Grades eines Doktors
der Ingenieurwissenschaften

vorgelegt von
Dipl.-Ing. Valeria Gracheva

eingereicht bei der Naturwissenschaftlich-Technischen Fakultät
der Universität Siegen
Siegen 2015

1. Gutachter: Prof. Dr.-Ing. Joachim Ender
2. Gutachter: Prof. Dr.-Ing. Otmar Loffeld
Tag der mündlichen Prüfung: 18.01.2016

Acknowledgements

Die Entstehung dieser Arbeit wäre nicht möglich gewesen, ohne die Hilfe von einigen Personen. Hier würde ich gerne die Gelegenheit nutzen diesen besonderen Menschen zu danken.
Vor allem danke ich natürlich meinem Doktorvater Prof. Dr.-Ing. Joachim Ender dafür, dass ich so viel von ihm lernen durfte. Ich danke ihm für die vielen Diskusionen, die motivierenden Gespräche, die Korrekturen meiner Rechnungen, dafür dass er immer die Zeit vergaß wenn wir über meine Arbeit redeten und dafür dass er nie an mir oder am Gelingen meiner Arbeit zweifelte. Ganz besonders möchte ich Herrn Ender dafür danken, dass er immer einen hohen Anspruch an mich hatte, aber auch immer Nachsicht hatte, wenn ich diesen Ansprüchen nicht genügte.
Ich danke Prof. Dr.-Ing. Ottmar Loffeld für die Aufnahme in das Promotionsprogramm „IPP Multi Sensorics“ am Zentrum für Sensorsysteme (ZESS), für die hilfreichen Gespräche bei den Fall Presentations und für die guten Ratschläge bei der Zwischenprüfung.
Ich danke dem Leiter der Abteilung „Array-gestützte Radarbildgebung“ Dr.-Ing. Andreas Brenner dafür, dass er es mir ermöglicht hat meine Promotion in seiner Abteilung zu schreiben. Ganz besonders danke ich Herrn Brenner für die Finanzierung meiner Experimente und für das Vertrauen, dass er mir bei der Planung der Kampagnen stets entgegenbrachte.
Natürlich danke ich auch meinem Teamleiter Dr.-Ing. Wolfram Bürger, dessen Tür für mich immer offen stand. Ich möchte ihm nicht nur für das Beantworten meiner fachlichen Fragen danken, sondern auch für die vielen persönlichen Gespräche, die mich immer wieder aufgebaut haben.
Ganz besonders möchte ich Herrn Dr.-Ing. Ludger Prünte danken, dessen Tafel immer Platz für meine mathematischen Probleme hatte. An einigen Stellen in meiner Arbeit wusste ich nicht weiter, aber die Diskussionen mit Ludger und seine Ideen haben mich immer wieder voran gebracht.
Ich danke Herrn Dr.-Ing. Patrick Berens und Herrn Dr.-Ing. Ingo Walterscheid für die vielen Hilfestellungen bei meiner Promotion und natürlich für die netten Gespräche.
Ich würde auch gerne Herrn Dr.-Ing. Christoph Gierull danken, dessen Ideen und Ergänzungen erheblich zur Verbesserung meiner Arbeit beigetragen haben.
Ein wichtiger Teil dieser Arbeit bestand aus der Analyse von realen Daten. Die Messkampagnen zur Akquisition dieser Daten wären nicht gelungen ohne das große Engagement

von Dipl.-Ing. Thomas Arrenbrecht, Dipl.- Ing. Olaf Peters und Dr.-Ing. Patrick Berens. Mein ganz besonderer Dank gilt auch Dipl.-Ing. (FH) Björn „Adele“ Papke, der für die Bootexperimente alles aus sich rausgeholt hat. Ich danke der PAMIR-Gruppe für die tolle Zeit auf den Messkampagnen. Auch ein großes Dankeschön an die Wehrtechnische Dienststelle (WTD 61) in Manchingen, ohne die unserer Experimente nicht stattgefunden hätten. An dieser Stelle würde ich auch gerne ganz besonders den Piloten Peter „Piet“ Koch und Robert „Robs“ Hierl für deren Engagement danken und natürlich auch für die schöne Zeit.
Ein ganz großes Dankeschön an meinen Freund Thorsten Rey für den Rund-um-die-Uhr Notfalldienst für mathematische Fragen jeglicher Art zu denen er immer eine Antwort wusste.
Ganz besonders würde ich gerne meinem Mann Martin danken, der mich immer über all die Jahre unterstützt hat, sowohl moralisch als auch kulinarisch.
Ich würde gerne meinen Großeltern Valeria und Jurij und meinen Tanten Ludmilla und Anna danken, die immer für mich da waren. Vor allem möchte ich aber meiner Mutter danken. Liebe Mama, ohne dich wäre das alles nicht möglich gewesen.

Kurzfassung

Piraterie, Schmuggel und illegale Fischerei gefährden die allgemeine Sicherheit auf Ozeanen und Meeren. Um diese Bedrohungen einzudämmen, müssen kleine Boote auf ausgedehnten Gebieten entdeckt und beobachtet werden. Flugzeuggetragene Radarsysteme können große Flächen überwachen und sind dieser Herausforderung daher gewachsen. Aufgrund der niedrigen Radarquerschnittsfläche (RCS) der kleinen Boote, ist die Detektion dieser Ziele jedoch immer noch ein ungelöstes Problem. Zusätzlich wird bei höher fliegenden Plattformen durch den steigenden Streifwinkel mehr Leistung von der Rückstreuung des Wassers, dem sogenannten Seeclutter, empfangen. Es müssen somit Ziele mit einem niedrigen Signal-zu-Clutter plus Rausch Verhältnis (SCNR) detektiert werden. Um ein geeignetes Verfahren zur Detektion von kleinen Booten mit flugzeuggetragenen Radarsystemen zu finden, wurden in dieser Arbeit reale Messdaten verarbeitet. Diese wurden während mehrerer Experimente über der Nordsee mit dem mehrkanaligen Radarsystem PAMIR und einem kleinen kooperativen Boot aufgenommen. Die Analyse dieser Daten zeigt zum einen, dass traditionelle Signalverarbeitungsmethoden nicht ausreichen, um das Ziel zu entdecken. Zum anderen wird demonstriert, dass mit dem sogenannten space-time adaptive processing (STAP) eine deutlich bessere Detektionsfähigkeit erreicht werden kann.
Es ist wünschenswert die zu erreichbare Detektionsleistung bei Anwendung von STAP auf maritime flugzeuggetragene Radarsysteme im Voraus zu kennen. Da für diese Berechnung aber die mehrkanaligen Eigenschaften des Seeclutters bekannt sein müssen, wird in dieser Arbeit ein theoretisches und ein Simulationsmodell hergeleitet. Zusätzlich werden die Spektraldichtematrix, das Raum-Zeit-Filter und die Kanalkorrelation des Seeclutters analysiert. Es wird verdeutlicht, dass durch die Bewegung des Wassers und durch mehrere Streuerarten die mehrkanaligen Eigenschaften von Land- und Seedaten unterschiedlich sind. Eine wichtige Auswirkung ist die Verbreiterung der Kerbe des Raum-Zeit-Filters bei Seedaten in Abhängigkeit vom Seegang.
Um die hergeleiteten Eigenschaften zu validieren, wurden insgesamt drei Messkampagnen mit dem flugzeuggetragenen Radarsystem PAMIR durchgeführt, wobei reale mehrkanalige Seedaten für unterschiedliche Dünnungsrichtungen, bei zwei unterschiedlichen Streifwinkeln und bei deutlich unterschiedlichen Wetterbedingungen gesammelt wurden. In dieser Arbeit wurden Berechnungen und Simulationen hergeleitet, die die Reproduzierbarkeit der realen mehrkanaligen Eigenschaften des Seeclutters bei verschiedenen Seegängen demonstrieren.

Abstract

Piracy, smuggling and illegal fishery threaten the overall security on oceans and seas. These threats typically arise from small and agile boats and are distributed over large areas. To control them, small maritime targets have to be detected and observed. Maritime airborne radar systems are capable of monitoring large areas and are therefore suitable to accomplish this challenge. The detection of small boats, however, is still an unresolved task due to the small radar cross section (RCS) of these boats. Additionally, the RCS of sea clutter rises for high altitude platforms due to the higher grazing angle, hence targets with low signal-to-clutter plus noise ratios (SCNR) have to be detected.
In order to investigate the appropriate processing to detect small boats from airborne radars, data from experiments over the North Sea with the multichannel radar system PAMIR and a small cooperative boat is evaluated in this thesis. This analysis demonstrates on one hand that traditional processing is not sufficient to detect these maritime targets, and on the other hand that with space-time adaptive processing (STAP) superior detection performance is achieved.
To apply STAP to a maritime airborne radar system, it is desirable to know its performance in advance. To accomplish this, the multichannel characteristics of sea clutter have to be understood. This thesis derives theoretical and simulation multichannel models by analyzing the spectral density matrix, the space-time filter and the channel correlation of sea clutter. Different multichannel properties for sea clutter compared to land clutter are demonstrated, which are due to the varying motion of sea echoes and due to different sea scattering types. An important implication of this difference is the broadening of the space-time filter notch in dependence on the sea condition.
To confirm the predicted properties, three measurement campaigns with the airborne radar system PAMIR were performed, where real multichannel sea data was acquired for different swell directions, two different grazing angles and significantly varying sea states. This thesis demonstrates the reproducibility of sea clutter multichannel characteristics of real data for different sea conditions with the help of calculations and simulations, which are introduced in this analysis.

Contents

Chapter 1

Introduction and Overview

Maritime radar systems can be traced back as far as 1904, when Christian Hülsmeyer presented the first demonstration of a radar system by detecting a ship from the Hohenzollern Bridge in Cologne. Ever since, maritime monitoring has been an important application of radar. During World War II it was noted that sea echo, often referred to as sea clutter, places severe limits on the detectability of ships [1]. Since then several attempts have been made to find theoretical explanations for the behavior of sea clutter [2]. One goal was to understand the physics of sea clutter by utilizing the studies of oceanography.
In 1955 a breakthrough in this field was achieved by Crombie, where he evaluated the Doppler spectrum of sea clutter collected with a HF-radar. This Doppler spectrum contained two pronounced peaks at Doppler frequencies which corresponded to the phase velocity of a water wave with the wavelength of one-half of the incident wavelength of the radar system [3]. In [4] and [5] sea scattering was theoretically calculated with a boundary perturbation approach. This calculation confirmed that contributions from the sea surface are only received by the radar system from water waves whose wavelength equals one-half of the radar wavelength divided by the cosine of the grazing angle. Further, these results illustrated how the measured radar cross section (RCS) is directly related to the spatial sea surface spectrum, hence conclusions on the sea surface itself can be made by measuring the RCS with a radar system.

State of the Art in Ocean Monitoring

The achieved results motivated several research activities in the area of ocean monitoring with synthetic aperture radar (SAR) [6, 7, 8]. Particularly important topics in this area are on one hand how water waves, which have much longer wavelengths than the ones from which scattering is received, influence the measured RCS [9], [10], [11]. On the other hand special interest was dedicated to how azimuth resolution of a SAR image is limited due to the movement of sea scatterers, which is measured by the so-called coherency time, defined as the time during which the echos from the scatterers stay coherent [12, 13, 14, 15].

In 1987 Goldstein and Zebker proposed a new application of ocean monitoring with radar systems [16]. They implied the ability to measure ocean surface currents by using interferometric SAR. This publication triggered a significant amount of experiments, where the along track interferometry phase was used to estimate current velocities of a certain area [17, 18, 19, 20]. In some experiments, however, the estimated current velocity did not correspond to the actual current velocity, which was measured with in-situ measurements [21]. These deviations forced again to have a closer look at studies of oceanography, where it was realized that several different velocities are present on the sea surface. The sum of these velocities is measured by the Doppler shift, hence the estimated velocity is not exclusively determined by the surface current [22].

State of the Art in Maritime Moving Target Indication

In parallel to the described research activities to monitor the ocean surface with radar, a different challenge regarding maritime radar systems emerged. Since the 90's, a considerable threat due to piracy has evolved. Additionally, illegal fishing, killing of endangered species, and smuggling of drugs have become a significant danger to the public. These threats have in common that they operate on small and agile boats, hence targets with low RCS have to be detected. Additionally, to monitor these boats over large areas, airborne radar systems are of great interest. The moving high altitude platform causes, however, a strong sea clutter return, which is spread over several Doppler frequencies.
While for maritime radar systems as demonstrated by Christian Hülsmeyer, where big ships have to be detected from a stationary low platform, no challenging signal processing is needed, these methods are no longer sufficient if small boats have to be detected within strong clutter. This motivated several research activities in the field of improving the detection of small targets with maritime radar systems. In [23] cell-averaging techniques were proposed to choose the threshold for a detector more appropriately and in [24] and [25] detectors were derived which consider the different statistics of sea clutter as compared to land clutter. Coherent single-channel data sets, where sea clutter was filtered prior to the actual detection, were shown in [26] and [27]. To suppress the clutter in [26], a temporal covariance matrix was estimated and in [27] the clutter was removed in the Doppler domain.

Research Objectives

If a time adaptive filter is applied prior to the actual detection, targets with low signals are at risk of being suppressed by the corresponding filter. To detect ground moving targets, superior performance can be achieved for certain scenarios if space-time adaptive processing (STAP) is utilized rather than time adaptive processing only [28, 29, 30]. For small maritime targets the STAP performance is however not known, because to our knowledge such experiments were not carried out yet. For this work we were able to collect multichannel sea data with the radar system PAMIR [31], where a small cooperative boat

was present inside the observed scene. One objective of this work is to use the acquired data to evaluate if the performance of space-time adaptive processing is superior to time adaptive processing only.
To apply STAP to a maritime radar system, it is desirable to know in advance which theoretical performance of STAP can be expected for that system. This allows for example to decide if the additional cost of building a multichannel system is justified or how the parameters of a multichannel system have to be chosen to achieve the desired performance. To evaluate the STAP performance for a radar system, the multichannel properties of the clutter have to be known. For land clutter the multichannel characteristics were derived in [32] and [33], allowing to calculate or simulate measures which model the STAP performance. In [34] simulations were performed for a displaced phased center antenna (DPCA) for a clutter type whose velocity is unequal to zero, and in [35] different multichannel characteristics were observed for sea clutter as compared to land clutter. A conclusive model to describe the multichannel properties of sea clutter is however still missing, but for maritime radar systems such a model is essential if STAP is to be applied.
The objective of the presented work is therefore to derive a theoretical multichannel model for sea clutter. The multichannel statistical description of land clutter is revised to include the properties of sea clutter. To understand the nature of sea clutter, once again studies of oceanography and physics of sea scattering have to be applied. To verify the theory, simulations of multichannel sea data sets are performed and analyzed. A specialty of this work is the availability of real multichannel sea data, which was collected with the PAMIR system. Sea data sets are available for different grazing angles, different swell directions, and different sea states. To our knowledge such experiments were not performed before. These data sets allow to compare the performed simulations with real data and analyze how well they match. To emphasize the difference between land and sea clutter, also simulations and experiments of a homogeneous land scene are presented.
The goal of this work is to gain further insight into the multichannel properties of sea clutter and to create a theoretical and simulation model, where the multichannel characteristics match the ones of real data for different sea conditions. The purpose of such a model is the possibility to predict STAP performance for future maritime radar systems.
The properties of sea clutter change significantly for different sea states. A meaningful statement of the STAP performance to suppress sea clutter can therefore only be made in dependency of some parameters of the sea surface. Further objectives of this work are therefore to determine these parameters as well as to estimate them from real multichannel data. An additional application of these estimations is to obtain information about the sea surface, allowing to perform some monitoring of the ocean conditions.

Major Contributions

The main contributions of this work are:

- Derivation of statistical multichannel sea clutter properties.

- Treatment of clutter physics and oceanography to explain the impact of sea clutter nature on multichannel measures and application of this knowledge for moving target indication (MTI) of maritime targets.
- Creation of a mathematical basis to calculate the multichannel properties of sea clutter and predict the MTI performance over water.
- Acquisition and analysis of real multichannel sea data and its comparison to simulated sea data to demonstrate the reproduction of multichannel properties for different sea states and swell directions.
- Validation of theoretically derived statistical measures with real data and demonstration of different land and sea clutter properties.
- Theoretical derivation and simulation of the impact of wave breaking on multichannel properties and confirmation with real data.
- Development of an estimator for the radial sea scatterer velocity variance to gain information about the sea state and to predict the MTI performance.
- Demonstration of the need to use space-time adaptive processing (STAP) to detect small maritime targets reliably using real sea data with a cooperative boat.

Previous Publications of Thesis Results

Some results have been presented at various conferences. In [36] different multichannel properties of sea clutter compared to land clutter are demonstrated. STAP performance in dependence of the swell direction is analyzed in [37]. Single channel and multichannel processing is applied to real sea data with a small cooperative boat in [38], where a significant improvement of the signal-to-clutter plus noise ratio (SCNR) with STAP is shown. The multichannel properties of sea clutter are derived in [39] and in [40] the channel correlation of different sea data sets is evaluated and compared to a theoretically calculated channel correlation. A journal paper has been submitted [41], where the multichannel properties of sea clutter are derived, the impact of wave breaking is analyzed and validation with real data is performed.

Thesis Outline

This work is organized as follows: In chapter 2 the radar fundamentals, which were used for this analysis, are summarized. The specialties of airborne radar systems are outlined and the multichannel properties of land clutter are described. The characteristics of sea clutter are presented in chapter 3. Here for one the oceanographic aspects of describing water waves and the sea surface are specified, and for another some results of the physics of the received echo from the sea surface are summarized. Chapter 4 describes

the PAMIR system and the experiments, which were performed with the PAMIR system to collect multichannel land and sea data. Additionally, some first evaluations of sea clutter are presented. The theoretical multichannel model for sea clutter is derived in chapter 5. In this chapter, the impact of sea clutter characteristics on multichannel properties is theoretically evaluated. Several measures, which are important to model the STAP performance, are altered to consider the nature of sea clutter. To validate the proposed model, simulations are performed in chapter 6. Several multichannel measures of simulated and real land and sea data sets are compared and analyzed, where the sea data is evaluated for several different sea conditions. In chapter 7 an experiment with a small cooperative boat is described, the collected data is evaluated, and a comparison of the detection performance between space-time adaptive and time adaptive processing only is demonstrated. Chapter 8 gives a conclusion and an outlook of the presented work.

Chapter 2

Radar Fundamentals

The statistical properties of multichannel land clutter are summarized in this chapter to be revised in the following chapters to consider the properties of sea clutter. Section 2.1 establishes the signal model of a coherent single channel radar system. This signal model is extended to multichannel radar systems in section 2.3. The need to use multichannel systems for moving target indication (MTI) with airborne radar systems is illustrated in section 2.2.

2.1 Signal Model

Consider a coherent microwave pulsed radar system, as described in [42], which transmits the signal $s_0(t)$ in the baseband frequency domain. The received normalized signal reflected by a single object in the baseband frequency domain can then be described as

$$s(t,T) = D(\mathbf{u}(T))s_0\left(t - \frac{2r(T)}{c}\right)\exp\left\{-j2\pi f_r \frac{2r(T)}{c}\right\}. \tag{2.1}$$

Here f_r denotes the carrier frequency, c is the speed of light, and $r(T)$ is the distance from the platform of the radar system to the object, from which an echo is received. The two time scales are described by the fast time t, which is the sampling time of one received pulse, and the slow time T, which denotes the pulse-to-pulse time. The antenna gain is considered by the two-way antenna pattern $D(\mathbf{u}(T))$, where $\mathbf{u}(T)$ is the line-of-sight vector (LOS vector).
The signal is assumed to be range compressed, and only one range resolution cell is considered. With $f_r = \frac{c}{\lambda_r}$, where λ_r is the carrier wave length of the radar system, and the described assumptions, the baseband range compressed signal equals

$$s(T,\mathbf{u}(T)) = D(\mathbf{u}(T))\exp\left\{-j\frac{4\pi}{\lambda_r}r(T)\right\}. \tag{2.2}$$

In the following analysis, only a short time interval is investigated, which allows to assume a constant LOS vector during the observed coherent processing interval (CPI). To

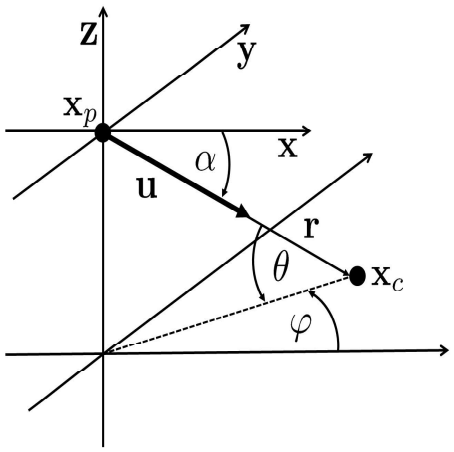

Figure 2.1: Radar geometry

consider moving objects, the distance $r(T)$ is defined as

$$r(T) = r_0 + v_{rel}T, \tag{2.3}$$

where v_{rel} is the constant relative radial velocity

$$v_{rel} = \mathbf{u}^H \left(\mathbf{v}_c - \mathbf{v}_p\right), \tag{2.4}$$

with $\mathbf{v}_c$ being the velocity vector of the echo, in the following referred to as clutter, and $\mathbf{v}_p$ the platform velocity vector. If the relative radial velocity is nonzero, then the phase of the signal described in equation (2.2) changes with time. This implies a varying frequency, which is defined as the Doppler frequency. Using the stop and go approximation [43], which states that the velocity of an object does not change between transmitting and receiving a pulse, the Doppler frequency can be calculated as

$$\begin{aligned}\mathcal{F}(v_{rel}) &= \frac{1}{2\pi}\frac{d}{dT}\left(-\frac{4\pi}{\lambda_r}r(T)\right) \\ &= \frac{1}{2\pi}\frac{d}{dT}\left(-\frac{4\pi}{\lambda_r}\left(r_0 + v_{rel}T\right)\right) \\ &= -\frac{2}{\lambda_r}v_{rel}.\end{aligned} \tag{2.5}$$

Figure 2.1 visualizes the geometry which is used in this analysis. The distance vector $\mathbf{r}$ can be calculated from the platform position vector $\mathbf{x}_p$ and the clutter position vector $\mathbf{x}_c$ as $\mathbf{r} = \mathbf{x}_c - \mathbf{x}_p$. The LOS vector is a unit vector, which equals

$$\mathbf{u} = \frac{\mathbf{x}_c - \mathbf{x}_p}{||\mathbf{x}_c - \mathbf{x}_p||}. \tag{2.6}$$

Using polar coordinates, this vector can also be expressed as

$$\mathbf{u} = \left(\cos\varphi\cos\theta, \sin\varphi\cos\theta, -\sin\theta\right)^T, \tag{2.7}$$

where φ is the azimuth angle and θ the grazing angle. Here the flat earth assumption is used, the grazing angle is therefore equal to the depression angle. The angle between the x-axis and the LOS-vector is denoted by α. This is the so-called cone angle. The relationship between the cone, azimuth and grazing angle is $\cos\alpha = \cos\varphi\cos\theta$.
Using the assumption of a short CPI and equations (2.2) and (2.5), the normalized radar clutter signal can be described as

$$\begin{aligned} s(T,u) &= D(u)\exp\left\{-j\frac{4\pi}{\lambda_r}v_{rel}T\right\} \\ &= D(u)\exp\left\{j2\pi\mathcal{F}(v_{rel})T\right\}. \end{aligned} \tag{2.8}$$

Here the constant phase term due to r_0 is neglected. Further, a linear array antenna is assumed, where the antenna elements are positioned along the x-axis. This allows to consider only the x-component of the LOS-vector, which is equal to $u = \cos\varphi\cos\theta$.

2.2 MTI for Airborne Radar Systems

For a stationary radar, the relative radial velocity is only nonzero if an echo from a moving object is received. If, however, the radar system is mounted on an airborne platform, the velocity v_{rel} is in general nonzero due to the movement of the platform. Different objects are then received at different Doppler frequencies, because they are viewed from different directions. If the clutter velocity is assumed to be zero, as this is the case for land clutter, and the platform is defined to move along the x-axis of the chosen coordinate system, the Doppler frequency can be stated as

$$\mathcal{F}(u) = \frac{2}{\lambda_r}v_p u. \tag{2.9}$$

A distinct difference between a ground-based and an airborne radar system can be realized by analyzing the clutter power. The received clutter signal can be calculated by integrating over all echo contributions of the observed area [2]. Here the integration is performed in polar coordinates, where the substitution $u = \cos\varphi\cos\theta$ is utilized. The clutter signal is here calculated for a constant range and a small intervall of look directions allowing to neglect terms resulting from the coordinate transformation from Cartesian to polar coordinates. A small intervall of look directions is justified, because for moving target indication (MTI) application with airborne radar systems, generally narrow beam antennas are used. The resulting integral describing the clutter signal of an observed area is therefore equal to

$$c(T) = \int_{\Omega} A(u)s(T,u)\,du. \tag{2.10}$$

Here $s(T,u)$ is the normalized radar clutter signal, which is described by equation (2.8), Ω is a set of visible look directions and $A(u)$ is the complex echo amplitude of the ground

from direction u. If a wide range of look direction is considered, $\frac{1}{\sqrt{1-u^2}}$ has additionally to be included inside the integrand in equation (2.10). The impact of this term on the subsequent derivations is however small. The complex echo amplitude is modeled as a random variable. It is assumed to be zero mean and its variance is denoted by σ_c^2. Due to the randomness of the amplitude, the clutter signal is regarded as a stochastic process and is assumed to be stationary. The Fourier transform of the clutter signal can be calculated as

$$\begin{aligned} C(F) &= \int_{-\infty}^{\infty} \int_{\Omega} A(u)D(u) \exp\left\{j2\pi(\mathcal{F}(u) - F)T\right\}\, du\, dT \\ &= \int_{\Omega} A(u)D(u) \int_{-\infty}^{\infty} \exp\left\{j2\pi(\mathcal{F}(u) - F)T\right\}\, dT\, du \\ &= \int_{\Omega} A(u)D(u)\delta(F - \mathcal{F}(u))\, du, \end{aligned} \tag{2.11}$$

where $\delta(F - \mathcal{F}(u))$ is the Dirac delta function. For the Fourier transform the time length is assumed to be infinite. In practice a long time length cannot be used for MTI applications. The outcome of the Fourier transform results then in a sinc-function rather than a Dirac delta function. As described in [44], windowing has to be applied to mitigate this effect. In this analysis a Hamming window is used.
The Dirac delta function states, that only those frequencies contribute to the clutter signal which are equal to the Doppler frequency. Due to the unique relationship between the Doppler frequency and the look direction from equation (2.9), the directional cosine is equal to

$$u(F) = \frac{F\lambda_r}{2v_p}. \tag{2.12}$$

This implies that for each frequency only one look direction has to be considered, which reduces equation (2.11) to

$$C(F) = A(u(F))D(u(F)). \tag{2.13}$$

The mean clutter power in the frequency domain can then be calculated as

$$\begin{aligned} P_c(F) &= E\left\{C^H(F)C(F)\right\} \\ &= \sigma_c^2 \left|D\left(u(F)\right)\right|^2, \end{aligned} \tag{2.14}$$

where $E\{\cdot\}$ is the expected value. Equation (2.14) shows that the clutter power is a scaled version of the two-way antenna pattern. Clutter power, which is positioned in the Doppler frequency range of $\pm\frac{v_p}{L_{tx}}$, where L_{tx} is the length of the transmit antenna, is referred to as clutter band. In this interval the clutter power drops from maximum to -4 dB.
Figures 2.2(a) and 2.2(b) show simulated clutter plus target power for different Doppler frequencies and different range bins. In figure 2.2(a) the simulation is performed for a ground-based radar and in figure 2.2(b) for an airborne radar. The moving target is

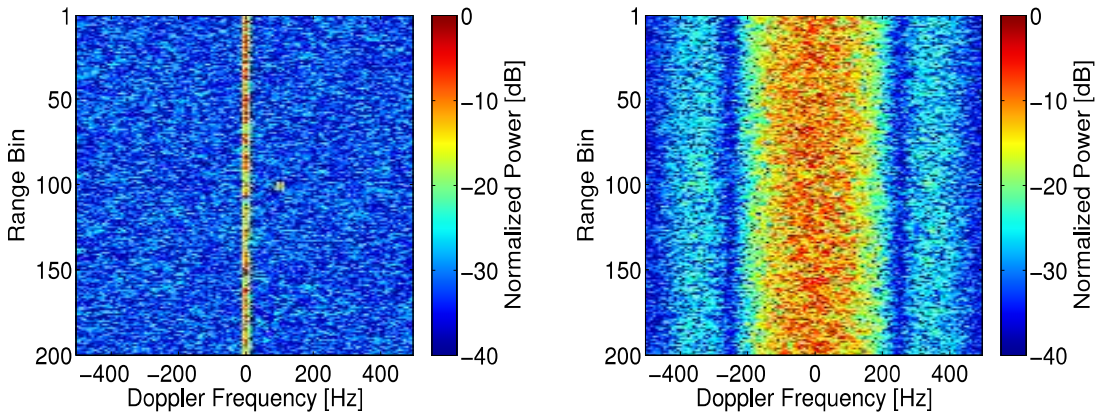

(a) Ground-based radar system

(b) Airborne radar system

Figure 2.2: Simulated clutter plus target power

injected at range bin 100 and Doppler frequency 100 Hz. The purpose of these figures is to demonstrate the difficulty of MTI with airborne radar systems as opposed to the ground-based ones. Figure 2.2(a) shows that it is not difficult to detect the moving target with a ground-based radar, because it has a from zero different Doppler frequency, while the clutter is only located at 0 Hz. It is therefore an easy task to discriminate between the clutter power and the power of the moving target. With an airborne radar system, however, the clutter power is spread over several Doppler frequencies, because of the clutter power distribution in dependency of the frequency, which is calculated in equation (2.14). Here the moving target has to compete with echoes of the clutter, which are both received at the same Doppler frequency. Figure 2.2(b) shows that for airborne radar the target cannot be detected without any processing, because it is masked by the clutter.
To detect moving targets reliably with airborne radar systems, an appropriate filter has to be applied. With single-channel MTI the cell under test can only be compared to the estimated mean power of the corresponding frequency. The best achievable filter for single-channel radar systems is therefore equal to

$$w(F) = \frac{1}{\sigma_c^2 \left|D(u(F))\right|^2 + \sigma_n^2}. \tag{2.15}$$

This filter is referred to as the time-adaptive filter (TAP). Noise is assumed to be white Gaussian noise with variance σ_n^2. Equation (2.15) shows that the best achievable filter for single-channel radar systems is approximately the inverse of the scaled two-way antenna pattern. Hence targets, which are positioned inside the clutter band, are attenuated by this filter. If the signal-to-clutter plus noise ratio (SCNR) of a slow target is low, it will be suppressed by the TAP filter, preventing a detection. To reliably detect such targets, multichannel radar systems have to be applied, which are described in the next section.

2.3 Multichannel Processing

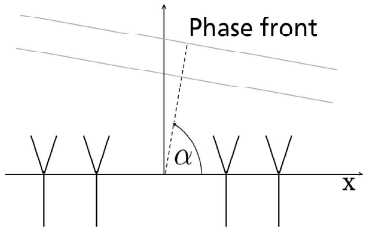

Figure 2.3: Multichannel radar system

The concept of multichannel systems is described in figure 2.3. A signal is received with several channels, whose phase centers are separated. Each channel is a subaperture with several elements, which form a phased array antenna. As denoted by figure 2.3, the position of channel n is defined as x_n and α is the angle between the x-axis and the antenna look direction, where $u = \cos\alpha$. The phase center positions of the channels are assumed to be along the x-axis, and only linear arrays are considered.
Ideally, all channels receive the same echoes, hence the received reflectivity is assumed to be identical for each channel. Due to the different phase center positions, the phase of the received signal is however different for each channel. These phase differences are considered by the direction-of-arrival vector (DOA vector). For channels aligned along the x-axis, the DOA vector can be stated as

$$\mathbf{d}(u) = \left(D_n(u) \exp\left\{ j\frac{2\pi}{\lambda_r} x_n u \right\} \right)_{n=1}^{N}, \tag{2.16}$$

where $D_n(u)$ denotes the two-way antenna pattern of channel n and the number of available channels is equal to N. The phase center of the transmitting antenna is assumed to be positioned at the origin of the coordinate system.
To describe the received signal of a multichannel system, the DOA vector has to be incorporated into the normalized radar clutter signal of equation (2.8)

$$\mathbf{s}(T, u) = \exp\left\{ j2\pi\mathcal{F}(u)T \right\} \mathbf{d}(u). \tag{2.17}$$

Here the Doppler frequency of an airborne radar system for land clutter is used. Note that this signal is now a vector.
A filter is considered to be optimal if it maximizes the SCNR. Such a filter can be derived by using the pre-whiten and match principle, which is described for example in [28]. The pre-whiten and match principle is performed by first whitening the signal with the square root of the clutter plus noise spectral density matrix, where this matrix is assumed to be positive definite and Hermitian, and then matching the expected signal times the square root of this spectral density matrix. The optimal filter in the frequency domain can be stated as

$$\mathbf{w}(u, F) = \mathbf{C}_z^{-1}(F)\mathbf{d}(u), \tag{2.18}$$

where $\mathbf{C}_z(F)$ is the spectral density matrix of the clutter plus noise signal

$$\mathbf{C}_z(F) = \mathbf{C}_c(F) + \mathbf{C}_n(F). \tag{2.19}$$

The noise vector is assumed to be white Gaussian and its spectral density matrix is therefore defined as $\mathbf{C}_n(F) = \sigma_n^2 \mathbf{I}_{N\times N}$, where $\mathbf{I}_{N\times N}$ is the identity matrix with the dimensions $N \times N$ and σ_n^2 is the noise variance.
Equation (2.18) shows that the filter is two-dimensional and suppresses the clutter not only in dependence of the frequency, but also in dependence of the look direction. With this filter the SCNR of a target, which is received with the amplitude a_t and from the look direction u_t, can be calculated as

$$\text{SCNR}(F) = |a_t|^2 \mathbf{d}^H(u_t)\mathbf{C}_z^{-1}(F)\mathbf{d}(u_t). \tag{2.20}$$

A useful measure to evaluate the performance of a multichannel radar system to detect targets after clutter suppression is the filter gain, which is introduced in [32]. This measure is here defined as

$$\gamma(u, F) = \frac{\mathbf{d}^H(u)\mathbf{C}_z^{-1}(F)\mathbf{d}(u)}{||\mathbf{d}(u)||^2}. \tag{2.21}$$

To gain further insight into the properties of this measure, the spectral density matrix has to be analyzed. To calculate the clutter spectral density matrix, as in [33], the properties of land clutter are assumed. This matrix can be evaluated from the Fourier transform of the clutter covariance matrix, which is equal to

$$\begin{aligned}\mathbf{R}_c(\tau) &= E\left\{\mathbf{c}(T+\tau)\mathbf{c}^H(T)\right\} \\ &= E\left\{\int_\Omega A(u)\mathbf{s}(T+\tau, u)\, du \int_\Omega A^H(u')\mathbf{s}^H(T, u')\, du'\right\}. \end{aligned}\tag{2.22}$$

The reflectivity is assumed to be spatially white, which reduces equation (2.22) to

$$\mathbf{R}_c(\tau) = E\left\{\int_\Omega A(u)A^H(u)\mathbf{s}(T+\tau, u)\, \mathbf{s}^H(T, u)\, du\right\} \tag{2.23}$$

$$= \int_\Omega E\left\{A(u)A^H(u)\right\}\mathbf{s}(T+\tau, u)\, \mathbf{s}^H(T, u)\, du \tag{2.24}$$

$$= \sigma_c^2 \int_\Omega \mathbf{s}(T+\tau, u)\mathbf{s}^H(T, u)\, du. \tag{2.25}$$

The Fourier transform of the covariance matrix equals

$$\begin{aligned}\mathbf{C}_c(F) &= \sigma_c^2 \int_{-\infty}^{\infty}\int_\Omega \mathbf{s}(T+\tau, u)\mathbf{s}^H(T, u)\, du\ \exp\left\{-j2\pi F\tau\right\} d\tau \\ &= \sigma_c^2 \int_\Omega \mathbf{d}(u)\mathbf{d}^H(u) \int_{-\infty}^{\infty} \exp\left\{j2\pi(\mathcal{F}(u) - F)\tau\right\} d\tau\, du \\ &= \sigma_c^2 \int_\Omega \mathbf{d}(u)\mathbf{d}^H(u)\delta(F - \mathcal{F}(u))\, du. \end{aligned}\tag{2.26}$$

As already described in section 2.2, due to the Dirac delta function, for each frequency the integral is only nonzero at one look direction, which is given by equation (2.12).

$$\mathbf{C}_c(F) = \sigma_c^2 \mathbf{d}(u(F))\mathbf{d}^H(u(F)), \tag{2.27}$$

as demonstrated in [33]. Equation (2.27) shows that the spectral density matrix is a rank one matrix, because it is only spanned by the vector $\mathbf{d}(u(F))$. The eigenvector of this matrix is a multiple of this vector, and the eigenvalue is equal to

$$\lambda_1(F) = \sigma_c^2 ||\mathbf{d}(u(F))||^2. \tag{2.28}$$

Due to this property, the clutter is only located in a one-dimensional subspace.
To calculate the spectral density matrix in equation (2.27), it is assumed that a pulse repitition frequency (PRF) is chosen, which is still sufficient to neglect alliasing, because otherwise the clutter subspace dimension would increase, as described in [32]. It is additionally assumed that a sufficient time length of the coherent processing interval (CPI) in combination with windowing, spectral leakage can be neglected. If spectral leakage has to be considered, an increase in the subspace dimension must be accounted for, as discussed in [44]. Especially, there will arise an additional contribution to the second eigenvalue which is dependent on the used Fourier filters in a deterministic waya and can easily be compensated for.
Figure 2.4 shows the space-time filter gain of equation (2.21), calculated with the clutter spectral density matrix described in equation (2.27). The filter gain indicates the amount of power by which a received signal is attenuated for each frequency and each look direction, where 0 dB means no attenuation. The displayed filter gain shows a notch along a diagonal line. The received signal is only attenuated where the look direction corresponds to the Doppler frequency given by equation (2.12).
A simulated filter gain at $u = 0$ is demonstrated in figure 2.5 to emphasize the difference between a single-channel and a multichannel system. In this figure the blue line indicates the best achievable filter with single-channel processing, and the green line shows the optimal filter evaluated with space-time adaptive processing (STAP). Both filters suppress the clutter. The TAP filter, however, also attenuates the target power at all Doppler frequencies of the clutter band. At significantly fewer frequencies, target attenuation needs to be feared with a STAP filter.
In practice, the spectral density matrix of real data is not known and has to be estimated. If the spectral density matrix equals the covariance matrix in the frequency domain, a maximum likelihood estimator can be derived. The received target free signal is assumed to be zero-mean and have a Gaussian distribution. Further, the different range bins are expected to be independent and identically distributed, so the maximum likelihood estimator of the spectral density matrix can be calculated as

$$\hat{\mathbf{C}}_z(F) = \frac{1}{L} \sum_{i=1}^{L} \mathbf{Z}(n_i, F)\mathbf{Z}^H(n_i, F). \tag{2.29}$$

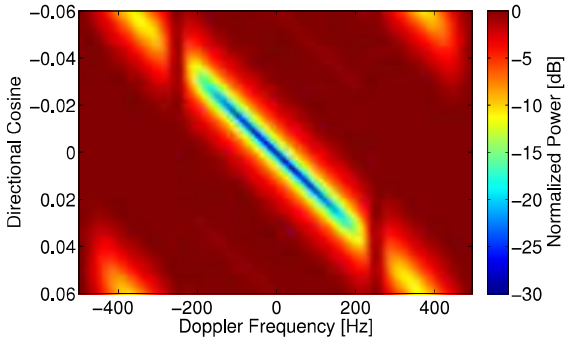

Figure 2.4: Calculated space-time filter gain with equations (2.21) and (2.27)

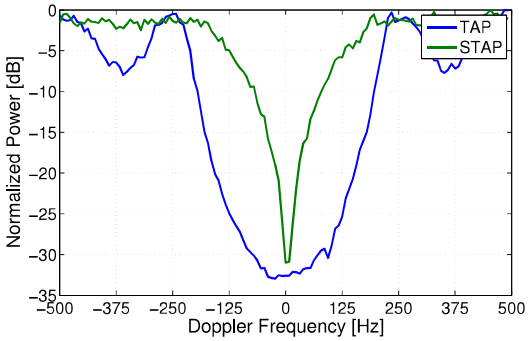

Figure 2.5: Simulated filter gain at $u = 0$ for single- and multichannel systems

Here L is the amount of available range bins, and $\mathbf{Z}(n_i, F)$ denotes the received multichannel signal at range bin n_i and frequency F. The derivation of this estimator can be found in [29].

The multichannel properties of land clutter are well known. For sea clutter, however, they are still ill understood. To derive these properties, the general characteristics of sea clutter have to be considered. They are described in the next chapter.

Chapter 3

Sea Clutter

During the 1960s, a revolutionary thinking about the origins of sea clutter developed. Several publications derived a direct relationship between clutter physics and oceanography ([9, 45, 1]), which suggests that an understanding of marine hydrodynamics is crucial to model sea clutter. In section 3.1 this chapter provides therefore a basic introduction to relevant topics of oceanography. The relationship between sea clutter physics and oceanography is illustrated in section 3.2, where the magnetic scattering field received by a radar from the sea surface is described. An important measure to evaluate the clutter properties is the Doppler frequency, which is evaluated in section 3.3 for sea clutter. Section 3.2 analyzes the scattering of capillary waves, but echoes are also received from breaking waves. Section 3.4 describes the origin of these events and investigates its scattering.

3.1 Water Waves

There are basically two types of surface water waves, capillary waves and gravity waves, depending on whether surface tension or gravity is the dominant restoring force. Capillary waves supply the surface fine structures, while gravity waves make up the larger and more visible surface elevations. Figure 3.1 visualizes the described water wave types. In order to arouse the surface to its fully developed or equilibrium state, the wind must blow for a sufficient time over a sufficient distance. As the wind starts to blow over a smooth sea surface, at first fluctuations of the atmospheric pressure induce capillary waves. With increasing wind velocity, waves grow and gravity forces are sufficient to support the wave motion, hence gravity waves develop.
The simplest way to mathematically describe gravity waves is by using the linear wave theory (or Airy wave theory after its publisher [46]). Here the elevation function of a regular single wave can be described as

$$\eta(\mathbf{x}, t) = \frac{H_s}{2} \cos\left(\mathbf{k}_s^H \mathbf{x} - 2\pi f_s t\right), \tag{3.1}$$

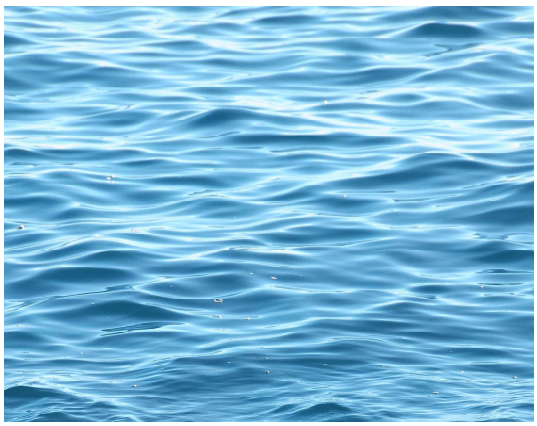

(a) Capillary waves

(b) Gravity waves

Figure 3.1: Two types of water waves

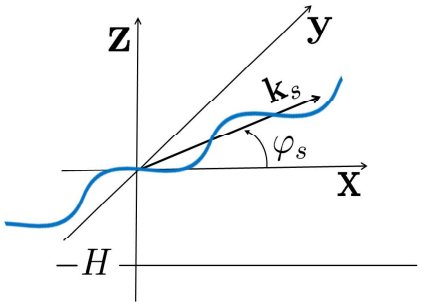

Figure 3.2: Assumed model for water wave

where H_s is the height, f_s the frequency and $\mathbf{k}_s$ the wave vector of the water wave. The position vector in the x-y-plane is denoted by $\mathbf{x} = (x, y)^T$. The described wave is shown in figure 3.2. Here the water depth is described by H. The coordinate system is chosen in such a way that the elevation of the water wave is centered around $z = 0$.
This wave moves with a certain velocity, called the phase velocity

$$\mathbf{c}_p = \frac{2\pi f_s}{||\mathbf{k}_s||} \frac{\mathbf{k}_s}{||\mathbf{k}_s||}. \tag{3.2}$$

However, also a velocity field is generated by this wave, due to which water particles, and anything else which is on the wave, are also in movement. If the velocity field can assumed to be irrotational, a velocity potential can be defined. The relationship between the velocity field and the potential is that the velocity field equals the divergence of the velocity potential. Assuming further that the flow is incompressible, the velocity potential can be used to form the Laplace equation. To solve the Laplace equation, appropriate boundary conditions have to be defined. For this calculation, three boundary conditions are determined. The first one is known as the bottom boundary condition. It states that

Figure 3.3: Orbital velocity for deep water assumption. Particle moves along a constant circle in dependency of the position on the gravity wave. The wave moves in the right direction.

the vertical velocity at the bottom has to be zero. The second boundary condition applies to the surface and is called the kinematic boundary condition. It results from the observation that water particles on the surface always stay on the surface, if wave breaking is not considered. The dynamic boundary condition, which is the third one, states that the pressure at the surface must be equal to the atmospheric pressure. The pressure at the surface is further calculated by using the Bernoulli equation. The calculation of the velocity field from the Laplace equation and the described boundary conditions is a well known problem, which is for example described in [47, 48, 49]. For the sake of completeness, the boundary conditions are summarized in appendix A. With the described boundary conditions, the velocity potential and hence the velocity field can be calculated as

$$\mathbf{v}_{orb}(\mathbf{x}, z, t) = \frac{\pi H_s f_s}{\sinh(||\mathbf{k}_s||H)} \begin{pmatrix} \cosh(||\mathbf{k}_s||(z+H)) \cos\left(\mathbf{k}_s^H \mathbf{x} - 2\pi f_s t\right) \cos\varphi_s \\ \cosh(||\mathbf{k}_s||(z+H)) \cos\left(\mathbf{k}_s^H \mathbf{x} - 2\pi f_s t\right) \sin\varphi_s \\ \sinh(||\mathbf{k}_s||(z+H)) \sin\left(\mathbf{k}_s^H \mathbf{x} - 2\pi f_s t\right) \end{pmatrix}, \tag{3.3}$$

where φ_s is the azimuth angle between the x-axis and the travelling direction of the water wave. The integration of this velocity vector shows that the fluid elements move in elliptical orbits. This velocity field is therefore usually referred to as the orbital velocity. If the water depth approaches infinity, the fractions with the hyperbolic functions reduce to $\exp\{||\mathbf{k}_s||z\}$.
If only waves at $z = 0$ are analyzed, the velocity vector reduces to

$$\mathbf{v}_{orb}(\mathbf{x}, t) = \pi H_s f_s \begin{pmatrix} \cos\left(\mathbf{k}_s^H \mathbf{x} - 2\pi f_s t\right) \cos\varphi_s \\ \cos\left(\mathbf{k}_s^H \mathbf{x} - 2\pi f_s t\right) \sin\varphi_s \\ \sin\left(\mathbf{k}_s^H \mathbf{x} - 2\pi f_s t\right) \end{pmatrix}. \tag{3.4}$$

This simplification is referred to as the deep water assumption. In practice, the deep water assumption is used if $H \geq \frac{\lambda_s}{2}$ is valid, where λ_s is the wave length of the water wave. This assumption is applied in this analysis. Equation (3.4) shows that in deep water the water particles move in closed orbital paths. This is demonstrated in figure 3.3, where a particle moves along a constant circle in dependency of where it is positioned on the water wave.
Water particles on real non-linear waves do not move in closed paths. There is a slow mean drift in the propagation direction, which is called the Stokes drift [50]. To consider

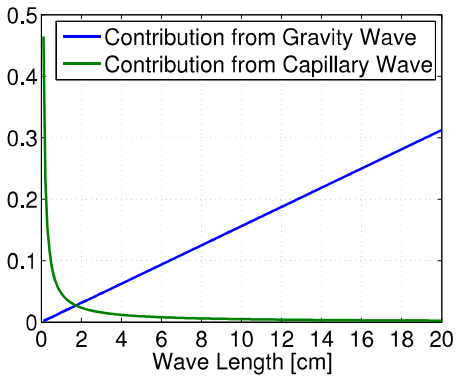

Figure 3.4: First and second addend of phase velocity in dependency of the wave length

the capillary waves, the dynamic boundary condition has to be changed, where the pressure on the surface is not considered to be constant any more, but is changed due to the surface tension [51]. Then the modified dynamic and the kinematic boundary conditions can be used to derive the dispersion relation for water waves

$$f_s = \pm\frac{1}{2\pi}\sqrt{g||\mathbf{k}_s|| + \frac{\nu}{\rho}||\mathbf{k}_s||^3}, \tag{3.5}$$

where g is the gravity constant and $\frac{\nu}{\rho} = 74 \cdot 10^{-6}\frac{\mathrm{Nm}^2}{\mathrm{kg}}$ is the surface tension-to-density ratio. Here also the deep water assumption is used, allowing to neglect the hyperbolic functions. Equation (3.5) is very important, because it states a direct relationship between the frequency and the wave length of a water wave. With equation (3.5) the magnitude of the phase velocity can be calculated as

$$c_p = \sqrt{\frac{g}{||\mathbf{k}_s||} + \frac{\nu}{\rho}||\mathbf{k}_s||}. \tag{3.6}$$

For a certain wave length, the phase velocity consists of a contribution from a gravity wave, which is the first addend, and a contribution from a capillary wave, given by the second addend. In figure 3.4 both contributions are evaluated in dependency of the wave length. This graph shows, that the contribution from a capillary wave is only significant for wave lengths up to 2 cm, while the contribution from a gravity wave can be neglected for these wave lengths. A wave is therefore considered to be a capillary wave if $\lambda_s \leq 2$ cm is satisfied. Waves having wave lengths where both contributions are significant are referred to as gravity-capillary waves.
A look at the sea reveals that the sea surface is random in space and time. A very useful description of the sea surface can therefore be achieved by statistical measures. One important measure is the spectral density of water waves

$$\tilde{C}_w(F) = E\left\{H(F)H^*(F)\right\}, \tag{3.7}$$

where $H(F)$ is the Fourier transform of the elevation function at a fixed point

$$H(F) = \int_{-\infty}^{\infty} \eta(0,t) \exp\left\{-j2\pi Ft\right\}\ dt. \tag{3.8}$$

Note that additionally the elevation function is assumed to be a stationary stochastic process, due to which

$$E\left\{H(F)H^*(F')\right\} = \delta(F-F')\tilde{C}_w(F) \tag{3.9}$$

is valid [52], where $\delta(\cdot)$ denotes the Dirac delta function. With the spectral density of water waves, many parameters describing the sea surface can be calculated. An important parameter for this analysis is the orbital velocity variance. Due to the deep water assumption, the variances of the horizontal and vertical orbital velocity components are assumed to be equal. The vertical velocity can be calculated from the time derivative of the elevation function, due to the kinematic boundary condition (see appendix A). The orbital velocity variance at a fixed point is therefore equal to

$$\sigma_{orb}^2 = E\left\{\frac{\partial\eta(0,t)}{\partial t}\cdot\frac{\partial\eta^*(0,t)}{\partial t}\right\}. \tag{3.10}$$

Exploiting the inverse Fourier transform of the elevation function results in

$$\begin{aligned}\sigma_{orb}^2 &= E\left\{\frac{\partial}{\partial t}\int_{-\infty}^{\infty} H(F)\exp\left\{j2\pi Ft\right\}dF\cdot\frac{\partial}{\partial t}\int_{-\infty}^{\infty} H^*(F)\exp\left\{-j2\pi Ft\right\}\ dF\right\}\\ &= \int_{-\infty}^{\infty}(2\pi F)^2 E\left\{H(F)H^*(F)\right\}\ dF\\ &= \int_{-\infty}^{\infty}(2\pi F)^2\tilde{C}_w(F)\ dF.\end{aligned} \tag{3.11}$$

For water waves usually only positive frequencies are observed [53]. Because $\eta(0,t)$ is a real function, also its covariance is real and $\tilde{C}_w(F)$ is therefore an even function, which allows to use the following definition

$$C_w(F) = \begin{cases} 2\tilde{C}_w(F) & F \geq 0 \\ 0 & F < 0 \end{cases}. \tag{3.12}$$

Equation (3.11) then reduces to

$$\sigma_{orb}^2 = \int_0^{\infty}(2\pi F)^2 C_w(F)\ dF. \tag{3.13}$$

To calculate the orbital velocity variance, the spectral density has to be known. Several empirical spectral densities for wind waves are available, the most popular one being the Pierson-Moskowitz spectrum [54]

$$C_{pm}(F) = \frac{2\pi\kappa g^2}{(2\pi F)^5}\exp\left\{-\chi\left(\frac{g}{2\pi FU_w}\right)^4\right\}. \tag{3.14}$$

Here κ and χ are constants with $\kappa = 8.1 \cdot 10^{-3}$ and $\chi = 0.74$. The wind velocity is denoted by U_w, which is measured at 19.5 m. This spectrum is considered valid for gravity waves and fully developed sea conditions. To calculate the velocity variance for a given scene of the sea surface, an integration over the waves, which contribute to the velocity variance, has to be performed [12]. The upper limit of this integration is not critical [13], therefore only the lower limit has to be evaluated

$$\sigma_{pm}^2 = \int_{F_L}^{\infty} (2\pi F)^2 C_{pm}(F)\, dF, \tag{3.15}$$

where F_L is the frequency of the longest wave which has to be taken into account. Performing the integration and using the gravity wave part of equation (3.5) to calculate the wave length of the longest wave results in

$$\sigma_{pm}^2 = \sqrt{\frac{\pi}{\chi}} \frac{\kappa}{4} U_w^2 \text{erf}\left(\frac{g\sqrt{\chi}\lambda_L}{2\pi U_w^2} \right), \tag{3.16}$$

where $\text{erf}(\cdot)$ is the error function. In general, however, λ_L is not known. If $\lambda_L \to \infty$ is assumed, as was done in [55], equation (3.16) reduces to

$$\sigma_{pm}^2 = \sqrt{\frac{\pi}{\chi}} \frac{\kappa}{4} U_w^2. \tag{3.17}$$

This equation corresponds to the highest possible orbital velocity variance for a certain wind velocity, if the Pierson-Moskowitz spectrum is used.

3.2 Scattering from Sea Surface

To gain some insight into the physical properties of sea clutter, the scattering mechanisms are described in this section. The detailed calculations of the sea surface scattering field are for example performed in [56]. In this section some main results are summarized, which are crucial for the assumptions and the understanding of the following analysis.
The scattering field can be calculated from the Stratton-Chu equations [57]. These equations can be derived from the Helmholtz equations, incorporating a Green's function and then simplifying the integrals with Green's theorem of the second kind.
To simplify the calculation, it is assumed that water is a perfect conductor. The electrical field on the sea surface is then zero, and the magnetic scattering field at the platform position $\mathbf{x}_p$ can be stated as

$$\mathbf{B}_s(\mathbf{x}_p) = -\iint_A (\mathbf{n}(\mathbf{x}_c) \times \mathbf{B}(\mathbf{x}_c)) \times \nabla G(\mathbf{x}_p, \mathbf{x}_c)\, dA. \tag{3.18}$$

Here $\mathbf{n}(\cdot)$ is the normal vector, $\mathbf{B}(\mathbf{x}_c)$ the magnetic field at the position of the scattering, $G(\cdot,\cdot)$ the Green's function, ∇ the nabla operator, and $\times$ denotes the cross product. To

calculate this field, the clutter position vector is chosen as $\mathbf{x}_c = (x, y, \eta(x, y))^T$, where $\eta(x, y)$ is the elevation function of the sea surface at a certain time instant and is assumed to be near the origin of the coordinate system. With this vector the normal vector $\mathbf{n}(\mathbf{x}_c)$ and the area element dA can be calculated. For the following calculations, an appropriate Green's function has to be chosen. In this analysis the free space Green's function is applied. Additionally, the magnetic field at position $\mathbf{x}_c$ has to be known to calculate the scattering magnetic field $\mathbf{B}_s(\mathbf{x}_p)$. Here the Kirchhoff assumption is used, which states that this magnetic field is twice the field which is transmitted by the radar system. This assumption is only valid if the sea surface is almost a tangent plane, hence multi-scatterings and shadowing effects can be neglected. Assuming only waves with small amplitudes on the surface and utilizing the described evaluations, the magnetic scattering field can be calculated as

$$\mathbf{B}_s(\mathbf{x}_p) = \frac{-\mathbf{B}_0 \exp\{jk_r||\mathbf{x}_p||\}}{\pi||\mathbf{x}_p||} k_{rz}^2 \iint_A \eta(x, y) \exp\{-2j(k_{rx}x + k_{ry}y)\}\ dx\ dy. \quad (3.19)$$

Here $\mathbf{B}_0$ is the amplitude vector of the magnetic field transmitted by the radar system and $\mathbf{k}_r = (k_{rx}, k_{ry}, k_{rz})^T$ defines the wave vector of this field. The detailed calculations to derive equation (3.19) are summarized in appendix B and can also be found in [58].
If the area over which the integration is performed can assumed to be big enough, the integral in equation (3.19) is a two-dimensional spatial Fourier transform of the sea surface elevation function, which is defined as

$$H(k_x, k_y) = \int_{-\infty}^{\infty} \int_{-\infty}^{\infty} \eta(x, y) \exp\{-j(k_x x + k_y y)\}\ dx\ dy. \quad (3.20)$$

Therefore equation (3.19) can be rewritten as

$$\mathbf{B}_s(\mathbf{x}_p) = \frac{-\mathbf{B}_0 \exp\{jk_r||\mathbf{x}_p||\}}{\pi||\mathbf{x}_p||} k_{rz}^2 H(2k_{rx}, 2k_{ry}). \quad (3.21)$$

This equation is of major importance, because for one it states a direct relationship between the scattering, which is received by the radar, and the sea surface elevation. For another, this equation shows that echoes are only received from water waves, whose wave lengths are related to the radar wave length by $\lambda_s = \frac{\lambda_r}{2\cos\theta}$. Hence, there is a direct relationship between the radar and water wave length. For X-band medium grazing angle radar systems, scattering is received from water waves in the range of $\lambda_s = 1.5$ cm - 2.1 cm. As described in the previous section, these water wave lengths correspond to capillary waves. An important conclusion is therefore, that for the following analysis the physical properties of capillary rather than gravity waves have to be considered.
For medium grazing angles, the assumption that the sea surface is almost a tangent plane and a perfect conductor is not valid. To derive satisfying solutions, multi-scatterings have to be considered, for example by using the perturbation method, and boundary conditions have to be applied. These calculations are performed in [4] and [5]. The results

yield polarization dependent scatterings, which are also observed in experimental data (see for example [2]). Furthermore, it is proposed in [9] and [45] that also the influence of gravity waves has to be considered, because due to these waves the grazing angle and the polarization changes locally. An overview of existing models to calculate scatterings from the sea surface can be found in [59] and [60]. The modified calculations of the scattering field, however, do not change the fact that for X-band radars only echoes from capillary waves are received.

3.3 Doppler Frequency of Sea Scatterers

While for land clutter the scatterers are assumed to be stationary, for sea clutter this assumption is not valid. The scatterers are themselves in motion, hence a certain clutter velocity has to be considered. It is assumed that echoes are received from capillary waves, due to the results of the previous section. The capillary waves have themselves a phase velocity, but they ride on gravity waves and are therefore additionally moved by the surface, which is identified in section 3.1 to be the orbital velocity, but also currents contribute to a further movement. The resulting velocity of the received scatterers at a certain time instant is therefore a sum of several different velocities

$$\mathbf{v}_c(\mathbf{x}) = \mathbf{v}_{cur} + \mathbf{c}_p + \mathbf{v}_{orb}(\mathbf{x}). \tag{3.22}$$

Here $\mathbf{v}_{cur}$ denotes the velocity of any currents, $\mathbf{c}_p$ is the phase velocity of the capillary waves, which have the wave length $\lambda_s = \frac{\lambda_r}{2\cos\theta}$, and $\mathbf{v}_{orb}(\mathbf{x})$ is the orbital velocity. The current velocity is usually assumed to be constant. The magnitude of the phase velocity of the capillary waves can be calculated as

$$c_p = \pm\sqrt{\frac{1}{4\pi}\frac{g\lambda_r}{\cos\theta} + \frac{\nu}{\rho}\frac{4\pi\cos\theta}{\lambda_r}}. \tag{3.23}$$

For X-band radar and medium grazing angles, this velocity is around ± 0.23 m/s. The orbital velocity can be calculated from equation (3.4). This velocity varies for different positions in dependence of where the capillary waves are positioned on the long waves.
In figure 3.5 the Doppler spectra of a stationary radar of land and sea clutter are presented to visualize the difference. For land clutter, power is only received at 0 Hz, because the clutter and platform velocities are zero. For sea clutter, however, echos from scatterers with different velocities are received, and the clutter power is therefore spread over different Doppler frequencies. The scatterer velocity changes due to a varying orbital velocity. The Doppler centroid is not at 0 Hz because of constant velocities and the constant shift of orbital velocities [22]. Note that for HF radars, where the phase velocity of the waves from which echoes are received is much higher, Doppler spectra with two peaks are expected. For microwave radars, however, the separation of the two peaks is quite small and they are broadened due to orbital velocities, so that two peaks are only visible for certain conditions, as analyzed in [61].

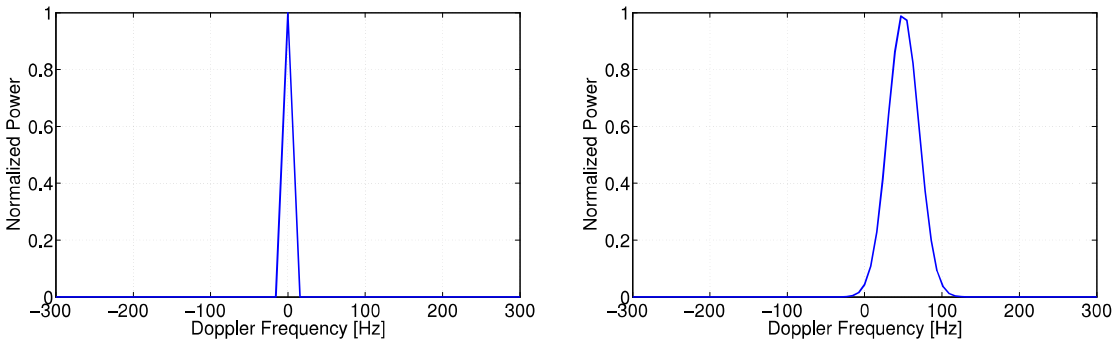

(a) Land clutter (b) Sea clutter

Figure 3.5: Normalized clutter power of a stationary radar system in dependency of the Doppler frequency for land and sea clutter

3.4 Scattering from Breaking Waves

It is shown in several publications, like in [2] and [56], that the sea surface RCS deviates from the scattering model derived for capillary waves. This observation suggests another scattering source, which is believed to be due to wave breaking.
Wave breaking occurs if the orbital velocity of the particles on the crest of a wave exceeds the phase velocity of the wave. Then the crest outruns the form of the underlying wave, causing wave breaking. This condition is called the kinematic breaking criterion. Further breaking criteria are summarized in [62] or [63].
The scattering properties of breaking waves are different from the ones of capillary waves. The Doppler shift of these scattering events is higher than the ones of scatterings from capillary waves, because the velocity of these particles has to be in the order of the phase velocity of the gravity wave. In [64] this is confirmed with experimental data, where Doppler spectra of breaking events in a water tank are analyzed. The results show a good fit between the radial velocity of these scatterers and $c_p \cos\theta$. This observation further suggests that the velocity of the described scatterers is mainly of horizontal nature.
How the scattering properties of capillary and breaking waves relate to each other is analyzed in [65]. This publication determines that scatterings of both wave types are independent of each other, due to which the resulting radar cross section of the sea surface can be calculated as a sum of the separate contributions.
For medium grazing angles, it is proposed in [56] and [66] that scatterings from breaking waves are mostly generated by the white foam which is present after such events. This scattering type can be modeled analog to the scattering of capillary waves, but with a much rougher surface, and is often referred to as whitecap scattering.
Wave breaking and its radar scattering is still ill understood and is an area of ongoing research. A summary of current problems can be found in [67].
In this analysis the scatterers from breaking waves are referred to as “fast scatterers” and

the scatterers from capillary waves are called “slow scatterers”, because the echoes of breaking waves have much higher velocities.

Chapter 4

Experiments with PAMIR

Three measurement campaigns were performed with the radar system PAMIR in the context of this thesis to validate the developed theory with real data. Section 4.1 summarizes the main parameters of this system and provides an overview of its special features. The radar and sea parameters and the flight paths of the corresponding experiments are illustrated in section 4.2. First evaluations of the collected data are provided in section 4.3, where some differences between land and sea clutter are demonstrated.

4.1 PAMIR System

New processing methods need to be validated with real data. For this purpose a multifunctional radar system, called PAMIR (Phased Array Multifunctional Imaging Radar) was developed at FHR [31]. A picture of the PAMIR system is shown in figure 4.1. Table 4.1 summarizes the main parameters of the PAMIR system. It is an airborne radar system, where the Transall is the carrier platform. The system operates at X-band and due to the phased array, the steering of the antenna beam in azimuth is performed electronically. This allows great flexibility to steer the antenna beam during an experiment. Additionally, an IMU (Inertial Measuring Unit) and a DGPS (Differential Global Positioning System) are implemented inside the PAMIR system. Due to these devices, the position and the orientation angles of the platform are known at any time instant. The roll-pitch-yaw angles are considered by the steering of the phased array antenna, hence the desired scene is always observed.
A special feature of the PAMIR system are the 9 autonomous and reconfigurable subgroups, of which the antenna consists. This allows to have up to 5 parallel receive antennas, where the positions of the phase centers can be chosen flexibel. For interferometry applications, an alignment in the across-track direction is selected, where up to 3 receive antennas can be used. For MTI applications an along-track alignment is possible, where also 3 receive antennas are available.

Carrier platform	Transall C-160
Polarization	VV
Center frequency	9.45 GHz (X-Band)
Bandwidth	Up to 3.6 GHz
Transmit power	240 W
Antenna	Active phased array
Antenna length in azimuth	0.79 m
Steering angle	$\pm$ 45°
Number of receive antennas for MTI	3
Phase center separation	0.2656 m

Table 4.1: Main parameters of PAMIR system

Figure 4.1: PAMIR system

4.2 Experiments

To validate the developed theory, several sets of multichannel data were collected with the PAMIR system during several experiments. To compare the multichannel properties of sea clutter with land clutter, an experiment over land was performed. This land data was acquired near Nuremberg in Germany, as shown in figure 4.2, in March 2012. Sea data was collected over the North Sea, near Heligoland. The water depth at the observed scene was approximately 40 m. A total of three sea experiments were performed, where the first two experiments took place in March 2012 and the last one in October 2012. For all sea experiments, the flight path was a square, where at each side of the square, data of the same scene was collected. This allowed to observe the same sea clutter at different swell directions in reference to the radar. The flight path of the third sea experiment is shown in figure 4.3. Here the track of the plane was rotated by $30°$ from the north, east, south and west direction. The track of the first two experiments was headed exactly towards the north, east, south and west direction.
All experiments were performed in a spotlight mode and all three channels in along-track direction were used to receive the data. For the sea experiments, it was possible to collect the data with depression angles of $15°$ and $35°$. The radar parameters of the land and sea experiments are summarized in table 4.2.

Figure 4.2: Flight path of land experiment

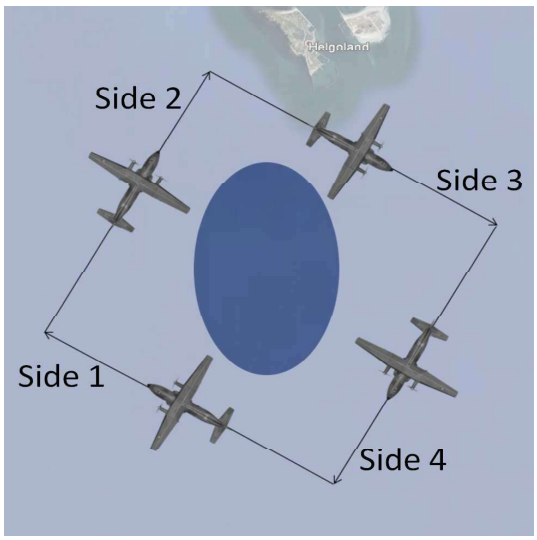

Figure 4.3: Flight path of sea experiment

Land Experiment	
Pulse repetition frequency (PRF)	3000 Hz
Range resolution	3.75 m
Nearest center slant range	6085 m
Platform velocity	100 m/s
Depression angle	20°
Slant swath	4500 m
Sea Experiment	
Pulse repetition frequency (PRF)	2000 Hz
Range resolution	3.75 m
Nearest center slant range	5222 m
Platform velocity	88m/s - 106 m/s
Depression angle	15°/35°
Slant swath	4500 m

Table 4.2: Radar parameters of performed experiments

The sea states varied quite strongly during the different data acquisitions over the North Sea. The sea was quite smooth during the first experiment, slightly rougher during the second one and very rough at the time of the last experiment. During the sea experiments, several weather stations, which were located near the observed scene, were used to collect information about the sea state. The weather stations recorded measured data approximately once an hour. These weather conditions are summarized in table 4.3. The wind and swell directions are evaluated in an east-north-up coordinate system (ENU). The significant wave height corresponds to the mean third maximum wave. The cur-

Experiment 1	
Significant wave height	0.3 m - 0.5 m
Mean water wave frequency	0.18 Hz - 0.21 Hz
Wind velocity	2 m/s - 4 m/s
Wind direction (ENU)	315°
Swell direction (ENU)	295° - 298°
Current velocity	0.1 m/s - 0.3 m/s
Current direction (ENU)	240° - 315°
Experiment 2	
Significant wave height	0.6 m - 0.8 m
Mean water wave frequency	0.25 Hz - 0.27 Hz
Wind velocity	7 m/s - 8 m/s
Wind direction (ENU)	0°
Swell direction (ENU)	129° - 140°
Current velocity	0.3 m/s - 0.5 m/s
Current direction (ENU)	315° - 350°
Experiment 3	
Significant wave height	2.3 m - 2.4 m
Mean water wave frequency	0.18 Hz
Wind velocity	10 m/s - 14 m/s
Wind direction (ENU)	84° - 96°
Swell direction (ENU)	77° - 95°
Current velocity	0.3 m/s
Current direction (ENU)	350°

Table 4.3: Weather conditions of sea experiments

rent velocities and directions were calculated by the BSH, Federal Maritime and Hydrographic Agency of Germany. With this data, the sea conditions of the first experiment can be assigned to sea state 2 on the Douglas Scale or 2 - 3 on the Beaufort Scale, the sea conditions of the second experiment correspond to sea state 3 on the Douglas Scale and 3 - 4 on the Beaufort Scale and during the last experiment, sea state 4 was reached on the Douglas Scale and 5 - 6 on the Beaufort Scale.

4.3 First Analysis

Figures 4.4 - 4.6 show the clutter power in the synthetic sum channel of different sea data sets in dependence of the Doppler frequency and slant range. Here a coherent processing interval (CPI) of 256 pulses is chosen to perform a Fourier transform, and 200 range bins are selected where maximum clutter power is present. The visualized signal is normalized to noise power and the centroid is shifted to 0 Hz.
Figure 4.4 shows two coherent processing intervals of the third experiment, collected with a $15°$ grazing angle. The data set in figure 4.4(a) was collected while the plane was flying on side 3 and in figure 4.4(b) data from side 4 is presented. Due to the collected weather data, the sea surface is assumed to move up swell in reference to the radar at side 3, and cross swell at side 4. The two CPIs in figure 4.4 are quite different. The clutter power is much more inhomogeneous for the up swell direction as compared to the cross swell direction. Additionally, in figure 4.4(a) many scatterers outside of the clutter band are evident at positive Doppler frequencies. These scatterers are due to wave breaking, which is more frequently present in the up swell direction than in the cross swell direction. More homogeneous sea clutter in the cross swell direction is for example also observed in [56].
Figure 4.5 shows the clutter power of the third experiment collected with a grazing angle of $35°$. Here higher clutter power is evident due to bigger resolution cells on the ground, resulting from a higher grazing angle. Additionally, the radar cross section of sea clutter is higher for higher grazing angles, as observed for example in [68] or [69]. Again, figure 4.5(a) shows a data set at the assumed up swell direction, and figure 4.5(b) shows a CPI at the assumed cross swell direction. Also here the clutter power is more inhomogeneous for the down swell direction, and several fast scatterers are evident. An analysis of the clutter power for different grazing angles and different swell directions can be found in [36].
In figure 4.6 two CPIs, collected from two different sides, of the first experiment are presented. Here a much lower clutter-to-noise ratio is evident. This is due to a lower RCS of the sea scatterers for smoother sea surfaces, as for example is also observed in [70] and [71]. The distribution of the clutter power is quite homogeneous for both data sets, without any fast scatterers.
If the Doppler shift resulting from the movement of the platform is removed, the centroid of land clutter is centered around 0 Hz. This is different for sea clutter, because here an additional Doppler shift due to the movement of the scatterers is present. To evaluate this Doppler shift, the Doppler frequency due to the platform velocity has to be calculated from equation (2.9). This calculation can be performed, because the track and the roll-pitch-yaw angles of the platform, which were present during the experiments, are known from the IMU. With this information, the platform coordinate system can be rotated to the earth coordinate system, where equation (2.9) can be applied. The mean radial velocity of the sea scatterers can then be calculated from the difference between the Doppler frequency of the actual clutter power centroid and the Doppler shift due to the platform

velocity. In this analysis the Doppler frequency of the centroid is estimated by correlating the Doppler spectrum with a Gaussian function, which has the same bandwidth as the Doppler spectrum, and searching for the maximum power. Note that radial sea scatterer velocity can also be evaluated by using the along-track-interferometry phase, as was done in several publications (for example [16, 20, 18]).
Figure 4.7 visualizes the estimated mean radial clutter velocity of sea data, collected during experiment 3. This experiment is chosen because the wind direction approximately corresponds to the swell direction and because the different swell directions were best captured during this experiment. The mean clutter velocity is evaluated dependent on the azimuth angle between the x-axis (East direction) and the center position in ENU coordinates. If the vector $\mathbf{x}_c = (x_c, y_c, z_c)^T$ denotes the center coordinates of the observed area, then this angle is defined as

$$\varphi_{\text{ENU}} = \begin{cases} \arccos\left(\frac{x_c - x_p}{\sqrt{(x_c-x_p)^2+(y_c-y_p)^2}}\right), & y_c - y_p \geq 0 \\ 360^\circ - \arccos\left(\frac{x_c - x_p}{\sqrt{(x_c-x_p)^2+(y_c-y_p)^2}}\right), & y_c - y_p < 0 \end{cases}. \tag{4.1}$$

Figure 4.7(a) shows the mean radial velocity of the sea scatterers at side 1. Here the sea clutter is assumed to move in the down swell direction. The estimated radial clutter velocity is always positive. In figure 4.7(c) this velocity is estimated for azimuth angles, where the up swell condition is assumed. For these angles a negative velocity was estimated for both grazing angles. Figures 4.7(b) and 4.7(d) show the estimated mean radial clutter velocity for assumed cross swell conditions. Here the sign of the radial velocity changes and the magnitude is around zero. The estimated radial sea clutter velocities collected with different grazing angles mostly match each other. Differences between different data sets are due to some randomness of the sea surface, changing sea conditions between the data takes (the time difference between data acquisitions of same sides but different grazing angles was around 1 hour), and the fact that the radial velocity is dependent on the grazing angle.

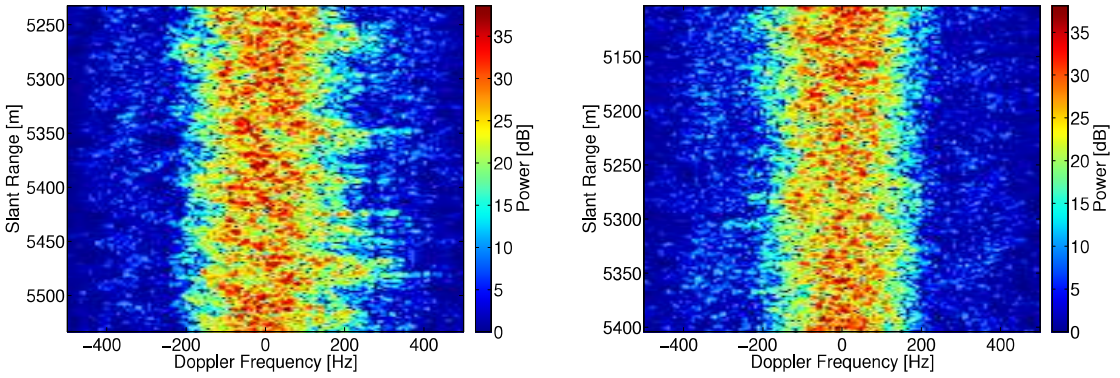

(a) Side 3 (b) Side 4

Figure 4.4: Clutter power in dependence of slant range and Doppler frequency, normalized to noise power. Experiment 3, grazing angle $15°$

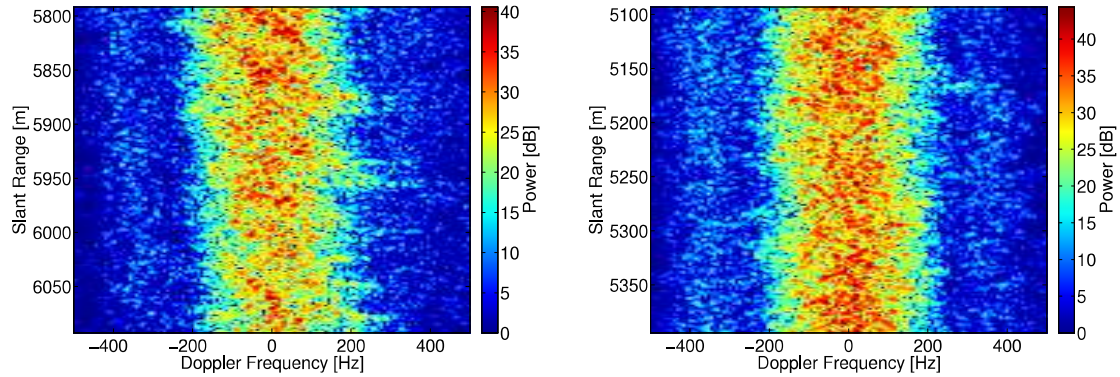

(a) Side 3 (b) Side 4

Figure 4.5: Clutter power in dependence of slant range and Doppler frequency, normalized to noise power. Experiment 3, grazing angle $35°$

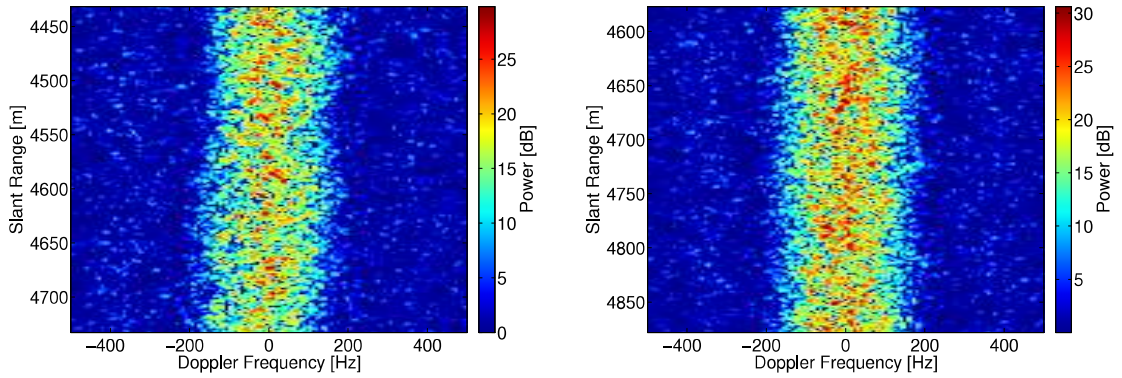

(a) Side 3 (b) Side 4

Figure 4.6: Clutter power in dependence of slant range and Doppler frequency, normalized to noise power. Experiment 1, grazing angle 15°

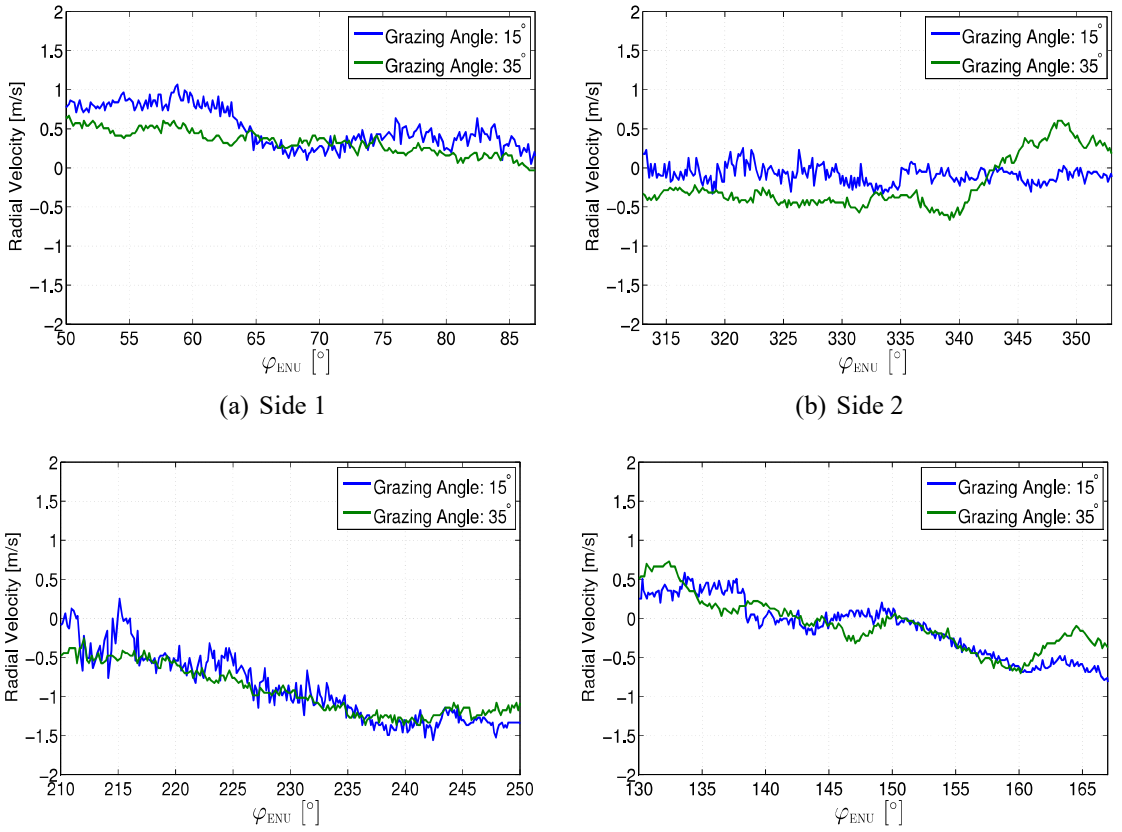

(a) Side 1 (b) Side 2

(c) Side 3 (d) Side 4

Figure 4.7: Estimated mean radial clutter velocity from Doppler centroid in dependence of azimuth angle

Chapter 5

Theoretical Multichannel Analysis of Sea Clutter

This chapter derives the multichannel properties of sea clutter. In sections 5.1 and 5.2 the multichannel statistical description of land clutter is revised to consider the different characteristics of sea clutter. Section 5.3 demonstrates how the properties of sea clutter affect the STAP performance. The multichannel model of sea clutter is used in section 5.4, to derive a theoretical description of the channel correlation. Section 5.5 considers the influence of fast scatterers, which result due to wave breaking, on the multichannel description of sea clutter and alters it.

5.1 Doppler Frequency

While the multichannel characteristics of land clutter are based on the assumption of stationary scatterers, for sea clutter also the contribution of the radial component of its own motion has to be considered. For microwave radars the varying scatterer velocities are determined by orbital motion ([72, 59]), as described in chapter 3.3. By defining the radial sea scatterer velocity for a certain position as $v_s = \mathbf{u}^H \mathbf{v}_{orb}$, the Doppler frequency of sea clutter can be stated as

$$\mathcal{F}(u, v_s) = \frac{2}{\lambda_r}(v_p u - v_s). \tag{5.1}$$

Here the platform is assumed to move along the x-axis, as in chapter 2.2. Due to the random nature of the sea surface, v_s is considered to be a realization of the random variable $V_s(u)$, which varies in dependence of the look direction and its variance is denoted by σ_s^2. This implies that the Doppler frequency $\mathcal{F}(u, V_s(u))$ is itself of random nature.
If a small interval of azimuth angles is assumed, as described in chapter 2.2, the relationship between the radial sea scatterer velocity variance and the orbital velocity variance can be stated as

$$\sigma_s^2 = \left(\cos^2(\varphi_0 - \varphi_s)\cos^2\theta + \sin^2\theta\right)\sigma_{orb}^2. \tag{5.2}$$

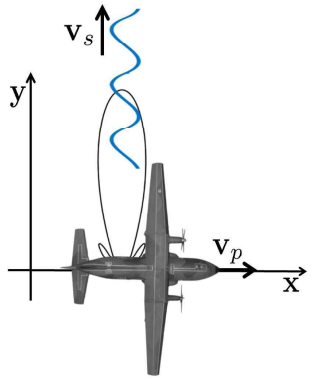

Figure 5.1: Geometry of described scenario to calculate Doppler frequency of sea clutter

The azimuth angle of the steering direction is denoted by φ_0. Here the random water waves are considered as in [73]. The described geometry to calculate the Doppler frequency is visualized in figure 5.1, and the orbital velocity variance properties are summarized in chapter 3.1.

5.2 Cross-Covariance Matrix and Spectral Density Matrix

To characterize the sea clutter signal, the Doppler frequency defined in equation (5.1) has to be considered. The sea clutter signal then equals with equation (5.3) to

$$\begin{aligned}\mathbf{c}(T) &= \int_{\Omega} A(u) \exp\left\{j2\pi\mathcal{F}(u, V_s(u))T\right\} \mathbf{d}(u)\, du \\ &= \int_{\Omega} A(u)\mathbf{s}(T, u, V_s(u))\, du. \end{aligned} \tag{5.3}$$

Here the normalized time-dependent radar clutter signal $\mathbf{s}(T, u, V_s(u))$ is dependent on the radial sea scatterer velocity. It is therefore also of random nature.
To calculate the clutter cross-covariance matrix, the complex echo amplitude is modeled as a spatially white and zero mean random variable with a random phase and the variance σ_c^2, as described in chapter 2.3. The correlation between $V_s(u)$ and $A(u)$ is zero due to the random phase. Since, no converse facts or suppositions are evident, we further assume that the echo amplitude and the radial sea scatterer velocity can considered to be independent, as it is done for example in [53] and [15]. If the clutter signal is a stationary process, the cross-covariance matrix equals

$$\begin{aligned}\mathbf{R}_c(\tau) &= E\left\{\mathbf{c}(T+\tau)\mathbf{c}^H(T)\right\} \\ &= \sigma_c^2 \int_{\Omega} E\left\{\mathbf{s}(T+\tau, u, V_s(u))\mathbf{s}^H(T, u, V_s(u))\right\}\, du. \end{aligned} \tag{5.4}$$

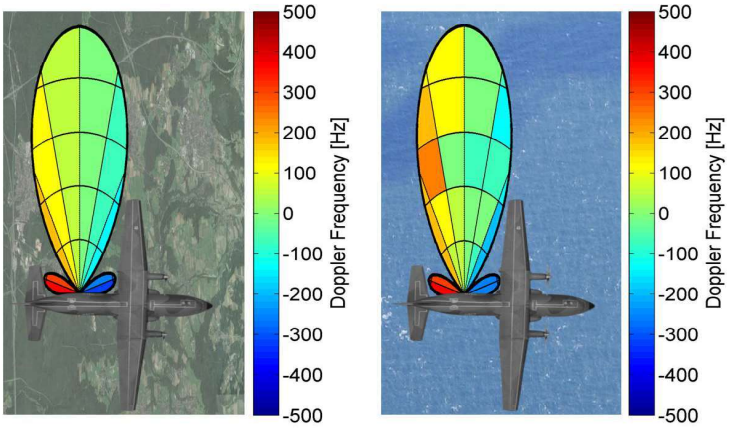

Figure 5.2: Relationship between Doppler frequency and look direction for land and sea clutter. For land clutter a certain Doppler frequency can be assigned to each look direction. For sea clutter the Doppler frequency varies for the same look direction in a random manner.

The sea clutter spectral density matrix $\mathbf{C}_c(F)$ can be calculated from the Fourier transform of the clutter cross-covariance matrix as

$$\mathbf{C}_c(F) = \sigma_c^2 \int_\Omega E\left\{\mathbf{d}(u)\mathbf{d}^H(u)\delta(F - \mathcal{F}(u, V_s(u)))\right\}\, du. \tag{5.5}$$

Due to the Dirac delta function, only those directions contribute to the integral for which the frequency equals the Doppler frequency. For sea clutter, equation (5.1) has to be inverted to calculate the directional cosine affecting the frequency F

$$u\left(F, V_s(u)\right) = \frac{F\lambda_r}{2v_p} + \frac{V_s(u)}{v_p}. \tag{5.6}$$

This equation shows the fundamental difference between land and sea clutter. Unlike for land clutter, for sea clutter there is no unique relationship between the look direction and the frequency. Due to the dependence of the look direction on the radial sea scatterer velocity, it is itself a random variable for each frequency. The different meanings of the look direction in reference to the frequency are visualized in figure 5.2. While for land clutter to each look direction a Doppler frequency can be assigned independently of the range bin, for sea clutter the Doppler frequency varies for the same look direction but different range bins in a random manner. To further calculate the spectral density matrix, a sea scatterer velocity distribution is assumed, which is independent of u. Using the integral form of the expected value and describing the sea scatterer velocity distribution with $p^{V_s}(v_s)$, the spectral density matrix can be written as

$$\mathbf{C}_c(F) = \sigma_c^2 \int_\Omega \int_{-\infty}^{\infty} \mathbf{d}(u)\mathbf{d}^H(u)\delta\left(F - \frac{2v_p}{\lambda_r}u + \frac{2}{\lambda_r}v_s\right) p^{V_s}(v_s)\, dv_s\, du. \tag{5.7}$$

For each frequency F and each scatterer velocity v_s, there is only one directional cosine, where the Dirac delta function is nonzero. The two-dimensional integral reduces therefore to a one-dimensional one

$$\begin{aligned}\mathbf{C}_c(F) &= \sigma_c^2 \int_{-\infty}^{\infty} \mathbf{d}\left(\frac{F\lambda_r}{2v_p} + \frac{v_s}{v_p}\right) \mathbf{d}^H\left(\frac{F\lambda_r}{2v_p} + \frac{v_s}{v_p}\right) p^{V_s}(v_s)\, dv_s \\ &= \sigma_c^2 E\left\{\mathbf{d}\left(\frac{F\lambda_r}{2v_p} + \frac{V_s(u)}{v_p}\right) \mathbf{d}^H\left(\frac{F\lambda_r}{2v_p} + \frac{V_s(u)}{v_p}\right)\right\}. \end{aligned} \tag{5.8}$$

It is assumed that all receive antennas have the same two-way antenna pattern $D(\cdot)$, which allows to define the DOA vector as

$$\mathbf{d}\left(u_0(F) + \frac{V_s(u)}{v_p}\right) = D\left(u_0(F) + \frac{V_s(u)}{v_p}\right) \mathbf{e}\left(u_0(F) + \frac{V_s(u)}{v_p}\right). \tag{5.9}$$

Here for convenience $u_0(F) = \frac{F\lambda_r}{2v_p}$ is specified, and the phase vector is denoted by

$$\mathbf{e}\left(u_0(F) + \frac{V_s(u)}{v_p}\right) = \left(\exp\left\{j\frac{2\pi}{\lambda_r} x_n \left(u_0(F) + \frac{V_s(u)}{v_p}\right)\right\}\right)_{n=1}^{N}. \tag{5.10}$$

The directional cosine $u_0(F)$ corresponds to the look direction of stationary scatterers. To further calculate the spectral density matrix analytically, $\mathbf{e}\left(u_0(F) + \frac{V_s(u)}{v_p}\right)$ is approximated by the Taylor series as

$$\mathbf{e}\left(u_0(F) + \frac{V_s(u)}{v_p}\right) \approx \mathbf{e}\left(u_0(F)\right) + \frac{V_s(u)}{v_p}\mathbf{e}'\left(u_0(F)\right), \tag{5.11}$$

where $\mathbf{e}'\left(u_0(F)\right)$ corresponds to

$$\mathbf{e}'(u_0(F)) = \left(jx_n\frac{2\pi}{\lambda_r}\exp\left\{j\frac{2\pi}{\lambda_r}u_0(F)x_n\right\}\right)_{n=1}^{N}, \tag{5.12}$$

and $\mathbf{d}'(u_0(F)) = D(u_0(F))\mathbf{e}'(u_0(F))$.
Here $V_s(u)$ is assumed to be zero mean. A non-zero mean has only a small impact on the following derivations and is discussed later.
With the phase vector in equation (5.11) the spectral density matrix becomes

$$\begin{aligned}\mathbf{C}_c(F) \approx \sigma_c^2 E\Bigg\{\left|D\left(u_0(F) + \frac{V_s(u)}{v_p}\right)\right|^2 \Bigg(\left(\mathbf{e}\left(u_0(F)\right) + \frac{V_s(u)}{v_p}\mathbf{e}'\left(u_0(F)\right)\right) \\ \left(\mathbf{e}\left(u_0(F)\right) + \frac{V_s(u)}{v_p}\mathbf{e}'\left(u_0(F)\right)\right)^H\Bigg)\Bigg\}. \end{aligned} \tag{5.13}$$

In the following an antenna coordinate system is chosen, where the center of gravity of phase center positions is at the origin. The vectors $\mathbf{e}(u_0(F))$ and $\mathbf{e}'(u_0(F))$ are then

orthogonal to each other. To further analyze the properties of the sea clutter spectral density matrix, its basis is changed, where the set of vectors which form the new basis are $\left\{\frac{\mathbf{e}(u_0(F))}{||\mathbf{e}(u_0(F))||}, \frac{\mathbf{e}'(u_0(F))}{||\mathbf{e}'(u_0(F))||}, \mathbf{b}_3(F), \ldots, \mathbf{b}_N(F)\right\}$, where $\mathbf{b}_3(F), \ldots, \mathbf{b}_N(F)$ are some vectors which are orthonormal to $\frac{\mathbf{e}(u_0(F))}{||\mathbf{e}(u_0(F))||}$ and $\frac{\mathbf{e}'(u_0(F))}{||\mathbf{e}'(u_0(F))||}$. This transformation is discussed in appendix C and it shows that the sea clutter spectral density matrix in equation (5.13) is a rank two matrix.
If a Gaussian distribution is assumed for the radial sea scatterer velocity and the absolute squared value of the two-way antenna pattern is described by a Gauss function, the eigenvalues of $\mathbf{C}_c(F)$ can be evaluated around the Doppler centroid as

$$\begin{aligned}\lambda_1(F) &\approx \sigma_c^2 \frac{\sigma_a}{\sqrt{\sigma_a^2 + \frac{\sigma_s^2}{v_p^2}}} ||\mathbf{d}(u_0(F))||^2, \\ \lambda_2(F) &\approx \frac{\sigma_c^2 \sigma_s^2}{v_p^2} \frac{\sigma_a^3}{\left(\sigma_a^2 + \frac{\sigma_s^2}{v_p^2}\right)^{(3/2)}} ||\mathbf{d}'(u_0(F))||^2,\end{aligned} \tag{5.14}$$

where σ_a^2 is the width of the Gauss function. The main steps to calculate these eigenvalues are summarized in appendix C.

If the influence of the radial sea scatterer velocity on the amplitude modulation caused by the two-way antenna pattern can be neglected, the distribution of the sea scatterer velocity does not require consideration and the sea clutter spectral density matrix reduces to

$$\begin{aligned}\mathbf{C}_c(F) \approx \sigma_c^2 &\mathbf{d}\left(u_0(F)\right) \mathbf{d}^H\left(u_0(F)\right) \\ &+ \frac{\sigma_c^2 \sigma_s^2}{v_p^2} \mathbf{d}'\left(u_0(F)\right) \mathbf{d}'^H\left(u_0(F)\right).\end{aligned} \tag{5.15}$$

This is a reasonable assumption, because the spectrum width is mainly determined by the platform velocity for airborne radar systems. The vectors $\mathbf{e}(u_0(F))$ and $\mathbf{e}'(u_0(F))$ correspond then to multiples of the eigenvectors of the clutter spectral density matrix. The eigenvalues of this matrix can be calculated as

$$\begin{aligned}\lambda_1(F) &= \sigma_c^2 ||\mathbf{d}(u_0(F))||^2, \\ \lambda_2(F) &= \frac{\sigma_c^2 \sigma_s^2}{v_p^2} ||\mathbf{d}'(u_0(F))||^2.\end{aligned} \tag{5.16}$$

Note that the sum of the eigenvalues in equation (5.16) does not coincide with the trace of the spectral density matrix in equation (5.15). This is due to a first order Taylor approximation. If the phase vector in (5.11) is approximated with three terms and the $\frac{V_s^4(u)}{v_p^4} x_n^4$-terms are neglected, then the eigenvalues can be calculated more appropriately, with their sum matching the trace of the matrix. This calculation can be found in appendix D. The

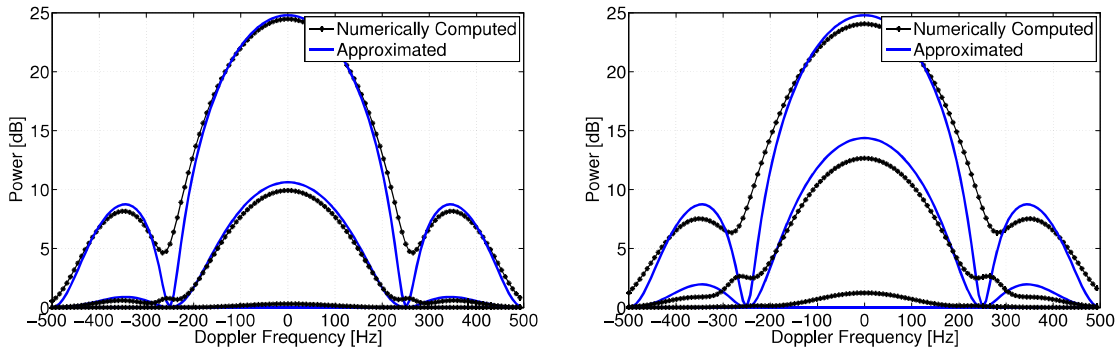

(a) $\sigma_s^2 = 0.2\ \mathrm{m}^2/\mathrm{s}^2$ (b) $\sigma_s^2 = 0.5\ \mathrm{m}^2/\mathrm{s}^2$

Figure 5.3: Approximated and numerically computed eigenvalue distributions in dependence of the Doppler frequency. The eigenvalues are estimated from the numerically computed spectral density matrix from equation (5.8) and analytically calculated from the approximations in equation (5.16).

result of this longer derivation is however only a small additional contribution to the first eigenvalue. The main multichannel properties are not changed by an additional term of the Taylor series. In the main analysis a second order Taylor approximation is therefore not considered.

To consider a non-zero mean μ_s, the Taylor approximation in equation (5.11) has to be performed around $u_0(F) + \frac{\mu_s}{v_p}$, which results in $\mathbf{e}(u_0(F) + \frac{V_s(u)}{v_p}) \approx \mathbf{e}(u_0(F) + \frac{\mu_s}{v_p}) + \left(\frac{V_s(u)}{v_p} - \frac{\mu_s}{v_p}\right) \mathbf{e}'(u_0(F) + \frac{\mu_s}{v_p})$. The eigenvectors of the clutter spectral density matrix in equation (5.15) are then multiples of $\mathbf{e}(u_0(F) + \frac{\mu_s}{v_p})$ and $\mathbf{e}'(u_0(F) + \frac{\mu_s}{v_p})$ and the centroids of the eigenvalue distributions are at $u_0(F) + \frac{\mu_s}{v_p}$.

To analyze if the spectral density matrix from equation (5.8) can be approximated by equation (5.13), the calculated eigenvalues are compared with numerically computed ones. For the numerical computation, the integral in equation (5.8) is evaluated numerically by assuming a Gaussian distribution for the radial sea scatterer velocity. In figure 5.3 the eigenvalues are calculated for different Doppler frequencies from equation (5.16), where the influence of the sea scatterer velocity on the clutter Doppler spectrum is neglected. In figure 5.3(a) the eigenvalues are computed with a sea scatterer velocity variance of $\sigma_s^2 = 0.2\ \mathrm{m}^2/\mathrm{s}^2$ and in figure 5.3(b) with $\sigma_s^2 = 0.5\ \mathrm{m}^2/\mathrm{s}^2$. Both figures validate the derived multichannel characteristics of sea clutter, because also for the numerically computed values, two eigenvalues have to be considered for sea clutter. The value of the second eigenvalue changes significantly around 0 Hz with a varying velocity variance, as is expected due to the dependence of the second eigenvalue on the sea scatterer velocity variance. While in figure 5.3(a) the approximated and the numerically computed eigenvalues match quite well, in figure 5.3(b) deviations are visible between the differently evaluated eigenvalues. This is due to a higher impact of the sea scatterer velocity on the clutter Doppler spectrum.

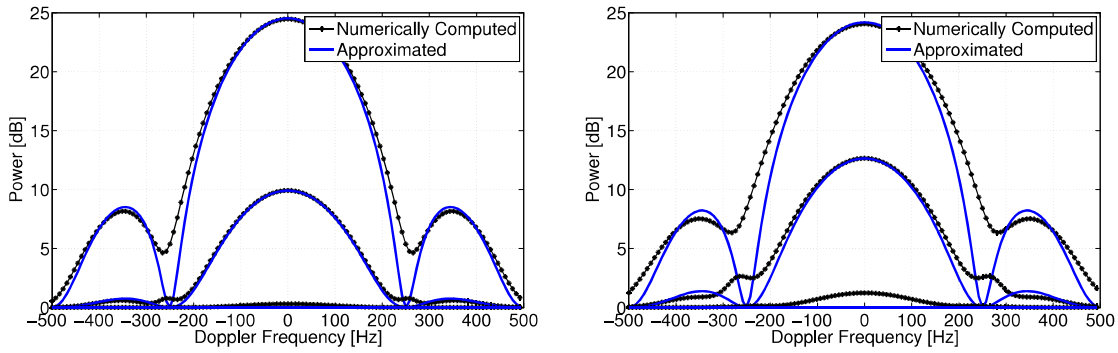

(a) $\sigma_s^2 = 0.2$ m^2/s^2 (b) $\sigma_s^2 = 0.5$ m^2/s^2

Figure 5.4: Approximated and numerically computed eigenvalue distributions in dependence of the Doppler frequency. The eigenvalues are estimated from the numerically computed spectral density matrix from equation (5.8) and analytically calculated from the approximations in equation (5.14).

Figure 5.4 demonstrates approximated and numerically computed eigenvalues for different Doppler frequencies, where the approximated eigenvalues result from equation (5.14). In this approximation the radial sea scatterer velocity variance influence on the clutter Doppler spectrum is considered. Also here the eigenvalues are computed with a velocity variance of $\sigma_s^2 = 0.2$ m^2/s^2, shown in figure 5.4(a), and with $\sigma_s^2 = 0.5$ m^2/s^2, which is visualized in figure 5.4(b). Figure 5.4(b) shows a better match of the numerically computed and calculated eigenvalues around the Doppler centroid as compared to the eigenvalues in figure 5.3(b). This analysis shows that a better eigenvalue evaluation is possible, if the distribution of the sea scatterer velocity is known. This is especially evident for high sea scatterer velocity variances.
In figures 5.3(b) and 5.4(b) also a small third eigenvalue of the numerical evaluation is visible. If $\frac{V_s^6(u)}{v_p^6} x_n^6$-terms are not neglected, also a third eigenvalue has to be accounted for. Generally, however, this resulting eigenvalue can be neglected in reference to noise.
The spectral density matrix of sea clutter has different properties than the one of land clutter. For land clutter, the spectral density matrix is ideally a rank one matrix, implying an one-dimensional clutter subspace. Therefore only one nonzero eigenvalue has to be considered. The spectral density matrix of sea clutter is, however, a rank two matrix. The clutter power is spanned over a two-dimensional subspace and there are two eigenvalues, which have to be accounted for. The differences between land and sea clutter spectral density matrices are described in [39].
The different properties of land and sea clutter are visualized in figures 5.5 and 5.6, where the power of CPIs of real land and sea data are projected on estimated eigenvectors of the clutter plus noise spectral density matrix for different range bins and Doppler frequencies. The projected power on the nth eigenvector is calculated from $||\mathbf{P}_n(F)\mathbf{Z}(r,F)||^2$, where $\mathbf{Z}(r,F)$ is the received multichannel vector from range bin r and frequency F and

$\mathbf{P}_n(F)$ is a projection matrix on the corresponding eigenvector, which is defined as

$$\mathbf{P}_n(F) = \frac{\mathbf{u}_n(F)\mathbf{u}_n^H(F)}{||\mathbf{u}_n(F)||^2}, \tag{5.17}$$

where $\mathbf{u}_n(F)$ is the eigenvector of dimension n.
For this demonstration sea data, which was acquired during experiment 3, is chosen. A downsampling to a PRF of 1000 Hz is performed, to allow a comparison between both experiments. This PRF is still sufficient to neglect aliasing. To carry out a Fourier transform, CPIs with 128 pulses are chosen and a Hamming window is applied to mitigate spectral leakage. By means of simulations, the chosen time length of a CPI in combination with windowing is found to be long enough to neglect spectral leakage. The Doppler shift due to the platform velocity is removed and for sea data additionally the Doppler shift caused by any present currents, modulations of the long waves or the phase velocity of capillary waves is eliminated. For each data set the figures are equally normalized and the same color scale is chosen, where the upper limit of this scale is the maximum power from the incoherent sum of all projections. For land data, figure 5.5(a) illustrates the power from the incoherent sum of all projections and figure 5.5(b) shows the power, which is projected on the first eigenvector. It is evident that the power distribution of both figures coincides, indicating that the entire clutter power is contained only along the first eigenvector. The power on the second and third eigenvector, visualized by figures 5.5(c) and 5.5(d), is equal and negligible. It is only due to noise and some non-ideal conditions. The projections of land data demonstrate that the clutter is only contained in a one-dimensional subspace, hence confirming a rank one land clutter spectral density matrix. The projections of sea data in figure 5.6 show, however, quite different characteristics. Figures 5.6(a) and 5.6(b), where the power from the incoherent sum of all projections and the power on the first eigenvector are illustrated, suggest that here most of the clutter power is contained along the first eigenvector, as well. But figure 5.6(c) visualizes that a considerable clutter power amount is also projected on the second eigenvector. Figure 5.6(d) shows that along the third eigenvector only noise is present. This observation validates the derivation of a rank two sea clutter spectral density matrix.

5.3 Space-Time Filter

One of the main reasons why the analysis of the clutter spectral density matrix is important is the insight into the properties of the space-time filter. As described in chapter 2.3, the space-time filter gain, defined in equation (2.18), informs about the detection performance for moving targets with the used multichannel system. In this chapter, the space-time filter gain of sea clutter is evaluated, and the alteration of this measure due to the different properties of the sea clutter spectral density matrix is described.
To evaluate the space-time filter gain, the inverse of the clutter plus noise spectral density matrix has to be calculated. To determine the inverse of this matrix, the singular value de-

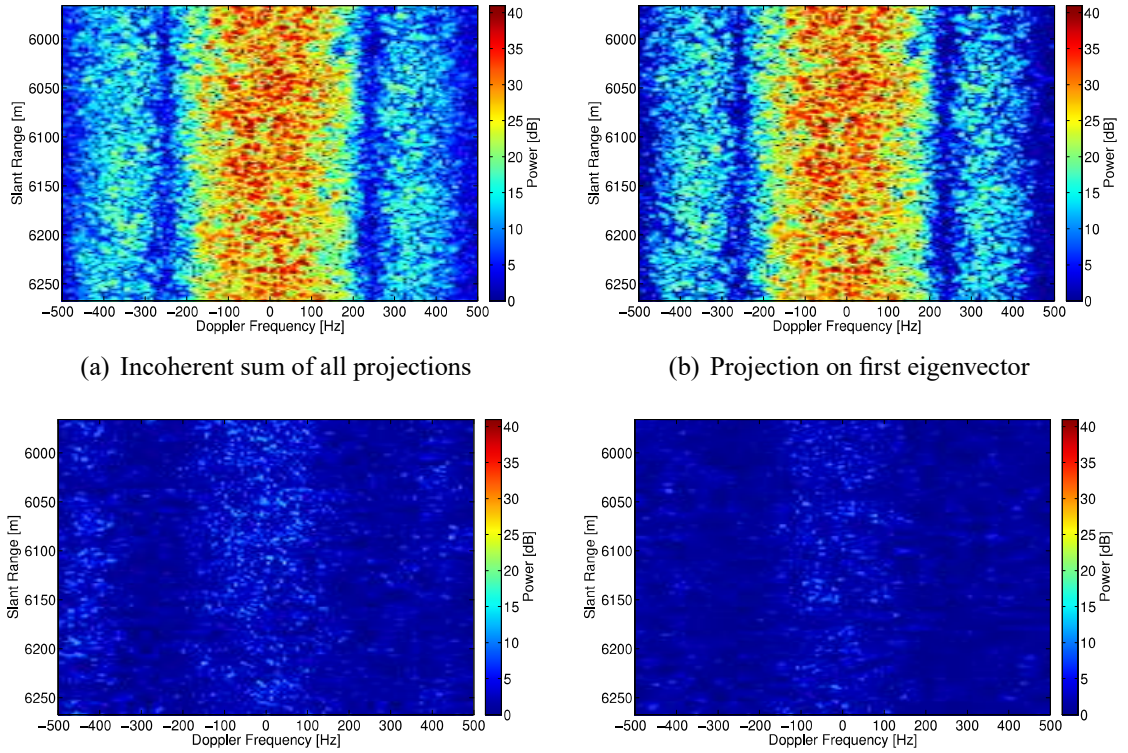

(a) Incoherent sum of all projections

(b) Projection on first eigenvector

(c) Projection on second eigenvector

(d) Projection on third eigenvector

Figure 5.5: Projections of received land data vector for different slant ranges and Doppler frequencies on estimated eigenvectors of the clutter plus noise spectral density matrix.

composition is applied. The clutter plus noise spectral density matrix can then be stated as

$$\mathbf{C}_z(F) = \mathbf{Q}(F)\mathbf{\Lambda}(F)\mathbf{Q}^H(F) + \sigma_n^2\mathbf{I}_{N\times N}, \tag{5.18}$$

where $\mathbf{Q}(F)$ is composed of all the orthonormal eigenvectors and

$$\Lambda(F) = \text{diag}\left(\lambda_1(F), \lambda_2(F), 0, \ldots, 0\right). \tag{5.19}$$

Here, as described in the previous section, it is assumed that due to the properties of sea clutter, two eigenvalues have to be considered. Further, the matrix inversion lemma (see [74]) is used, which is defined as

$$(\mathbf{A}+\mathbf{BCD})^{-1} = \mathbf{A}^{-1} - \mathbf{A}^{-1}\mathbf{B}\left(\mathbf{C}^{-1}+\mathbf{DA^{-1}B}\right)^{-1}\mathbf{DA^{-1}}, \tag{5.20}$$

where $\mathbf{A}$, $\mathbf{B}$, $\mathbf{C}$ and $\mathbf{D}$ all denote matrices of the correct size.
To calculate $\mathbf{C}_z^{-1}(F)$, these matrices are defined as follows:
$\mathbf{A} = \sigma_n^2\mathbf{I}_{N\times N}$, $\mathbf{B} = \mathbf{Q}(F)\mathbf{\Lambda}(F)$, $\mathbf{C} = \mathbf{I}_{N\times N}$ and $\mathbf{D} = \mathbf{Q}^H(F)$. With equation (5.20), the

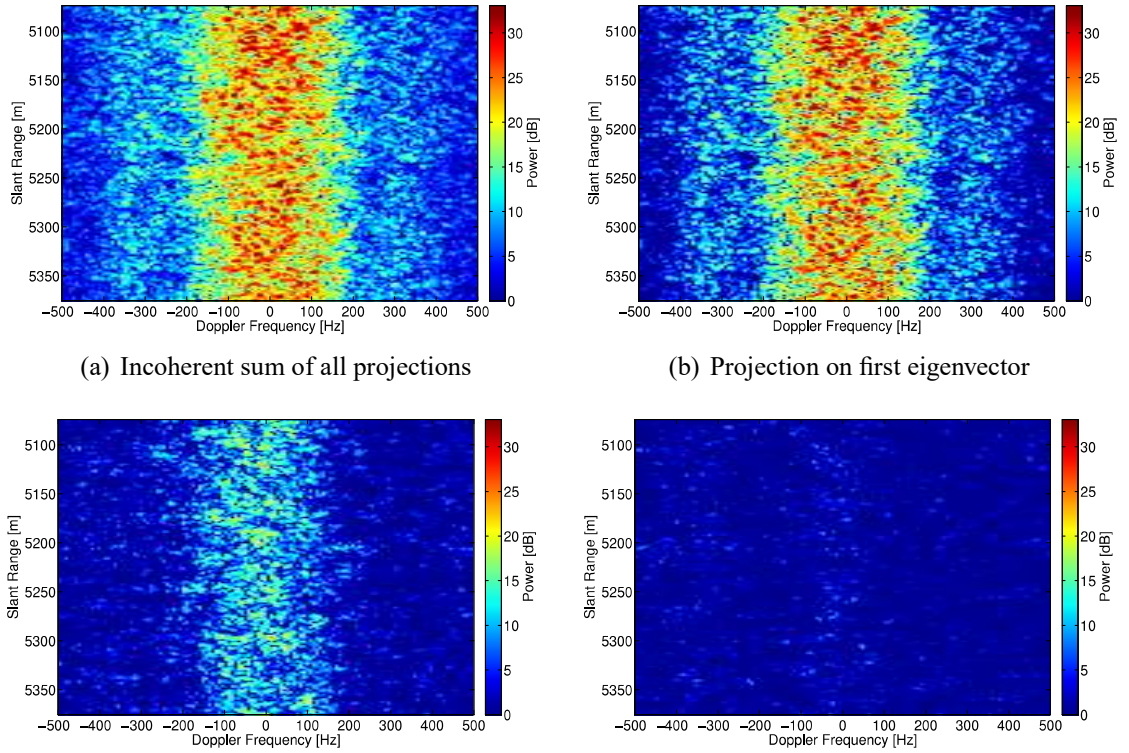

(a) Incoherent sum of all projections

(b) Projection on first eigenvector

(c) Projection on second eigenvector

(d) Projection on third eigenvector

Figure 5.6: Projections of received sea data vector for different slant ranges and Doppler frequencies on estimated eigenvectors of the clutter plus noise spectral density matrix.

inverse spectral density matrix is equal to

$$\mathbf{C}_z^{-1}(F) = \frac{1}{\sigma_n^2}\left(\mathbf{I}_{N\times N} - \frac{\lambda_1(F)}{\lambda_1(F)+\sigma_n^2}\frac{\mathbf{e}(u_0(F))\mathbf{e}^H(u_0(F))}{||\mathbf{e}(u_0(F))||^2} - \frac{\lambda_2(F)}{\lambda_2(F)+\sigma_n^2}\frac{\mathbf{e}'(u_0(F))\mathbf{e}'^H(u_0(F))}{||\mathbf{e}'(u_0(F))||^2}\right). \tag{5.21}$$

The eigenvalues $\lambda_1(F)$ and $\lambda_2(F)$ are as described in the previous section. If these eigenvalues are much bigger than the noise power, $\mathbf{C}_z^{-1}(F)$ reduces to a projection matrix, which projects the received signal to a subspace orthogonal to the clutter subspace, spanned by the two eigenvectors of the clutter spectral density matrix

$$\mathbf{C}_z^{-1}(F) = \frac{1}{\sigma_n^2}\left(\mathbf{I}_{N\times N} - \frac{\mathbf{e}(u_0(F))\mathbf{e}^H(u_0(F))}{||\mathbf{e}(u_0(F))||^2} - \frac{\mathbf{e}'(u_0(F))\mathbf{e}'^H(u_0(F))}{||\mathbf{e}'(u_0(F))||^2}\right). \tag{5.22}$$

For land clutter, only the first eigenvalue in equation (5.21) is nonzero, therefore this matrix projects to a subspace which is only orthogonal to the DOA vector, as described in

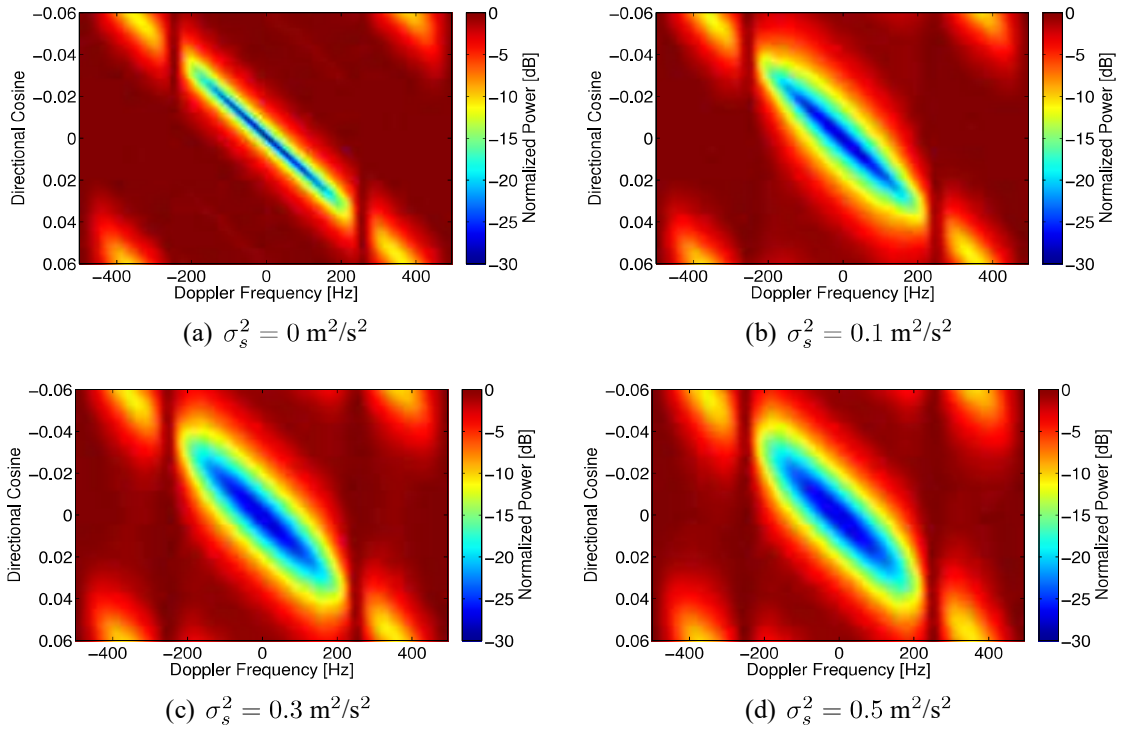

(a) $\sigma_s^2 = 0\ \mathrm{m}^2/\mathrm{s}^2$ (b) $\sigma_s^2 = 0.1\ \mathrm{m}^2/\mathrm{s}^2$

(c) $\sigma_s^2 = 0.3\ \mathrm{m}^2/\mathrm{s}^2$ (d) $\sigma_s^2 = 0.5\ \mathrm{m}^2/\mathrm{s}^2$

Figure 5.7: Calculated normalized space-time filter gain with different sea scatterer velocity variances

[32]. The evaluation of the inverse of the clutter plus noise spectral density matrix, shows the fundamental difference between land and sea clutter. For land clutter, only an one-dimensional clutter subspace has to be suppressed, therefore after space-time filtering an $N-1$-dimensional signal is left. For sea clutter, a two-dimensional clutter subspace has to be considered to remove the clutter from the received signal. Hence, after suppression of sea clutter with a space-time filter, only an $N-2$-dimensional signal is left for target detection and localization.

The second eigenvalue is much smaller than the first one, because it is proportional to the inverse of v_p^2. The assumption that $\lambda_2(F)$ is much bigger than σ_n^2 is therefore in general not valid. Then, the inverse spectral density matrix does not completely suppress the dimension spanned by the second eigenvector. The amount of suppression is dependent on the second eigenvalue, which depends on the sea scatterer velocity variance.

Figure 5.7 demonstrates space-time filter gains, calculated from equations (2.21) and (5.21) with the parameters of the PAMIR system. Here the eigenvalues of equation (5.16) are used. The different space-time filter gains are calculated with different sea scatterer velocity variances. The filter gain indicates the amount of power by which a received signal is attenuated for each frequency and each look direction, where 0 dB means no attenuation. In 5.7(a) an evaluation with $\sigma_s^2 = 0\ \mathrm{m}^2/\mathrm{s}^2$ is performed, which corresponds to land clutter. The displayed filter gain shows a notch along a diagonal line. The received

signal is only attenuated, where the look direction corresponds to the Doppler frequency by equation (2.9). The other filter gains are calculated with $\sigma_s^2 = 0.1$ m^2/s^2, $\sigma_s^2 = 0.3$ m^2/s^2 and $\sigma_s^2 = 0.5$ m^2/s^2, visualized by figures 5.7(b) - 5.7(d). On one hand, these figures show that the filter notch of land clutter is much narrower than the ones of sea clutter. This is expected due to the additional clutter subspace dimension, which has to be considered by the filter for sea clutter. On the other hand, figures 5.7(b) - 5.7(d) show a broader filter notch for higher velocity variances. This is due to the dependence of the second eigenvalue on the sea scatterer velocity variance. A broader filter notch means that for each look direction a target is attenuated at more radial velocities by the corresponding filter.

5.4 Channel Correlation

Another important multichannel measure is the channel correlation. The channels have to be highly correlated for a successful STAP performance. Channel correlation is however also important for other radar applications. For ocean monitoring with interferometric SAR, for example, this measure places limitations on the achievable sensitivity of current velocity measurements [75].
Channel correlation is a measure of the similarity between the received signals at channels n and n'. This measure is here defined as

$$\rho_{nn'} = \frac{E\left\{Z_n(F_c)Z_{n'}^H(F_c)\right\}}{\sqrt{E\left\{|Z_n(F_c)|^2\right\}E\left\{|Z_{n'}(F_c)|^2\right\}}}, \tag{5.23}$$

where F_c is the Doppler centroid. The denominator of this equation is calculated by assuming equal power at all channels. If the scatterers are stationary, as this is the case for land data, this value is equal to

$$\begin{aligned} E\left\{|Z_n(F_c)|^2\right\} &= E\left\{C_n^H(F_c)C_n(F_c)\right\} + \sigma_n^2 \\ &= \sigma_c^2|D(u(F_c))|^2 + \sigma_n^2. \end{aligned} \tag{5.24}$$

The numerator for land data can be calculated due to $u(F) = \frac{F\lambda_r}{2v_p}$ as

$$E\left\{Z_n(F_c)Z_{n'}^H(F_c)\right\} = \sigma_c^2|D(u(F_c))|^2 \exp\left\{j\frac{2\pi}{\lambda_r}u(F_c)(x_n - x_{n'})\right\}. \tag{5.25}$$

The constant exponential term in equation (5.25) is known and is usually compensated for, if the look direction is unequal to zero, to compare the channel correlation [76]. Considering further the clutter-to-noise ratio (CNR) of a single channel to be

$$CNR_n = \frac{\sigma_c^2 E\left\{|D(u(F_c))|^2\right\}}{\sigma_n^2} \tag{5.26}$$

reduces the channel correlation of land data to

$$\begin{aligned}\rho_l &= \frac{\sigma_c^2 |D(u(F_c))|^2}{\sigma_c^2 |D(u(F_c))|^2 + \sigma_n^2} \\ &= \frac{1}{1 + \frac{1}{CNR_n}},\end{aligned} \tag{5.27}$$

as can for example be found in [77]. This equation captures the land data channel correlation for ideal experiment conditions. There are several situations under which further channel decorrelation occurs for land experiments. One possible source is if the subapertures of the channels do not illuminate the same scene. Another possible decorrelation source is any kind of uncompensated system delays between different channels. For high bandwidth experiments, also carrier wave lengths of different clutter echoes will vary, causing additional decorrelation. Further, the assumption of an ideal antenna is not always valid. Mutual coupling between single elements of the antenna, for example, cause additional channel decorrelation. The presence of different bandpass filters for different channels also decorrelates the channels, as demonstrated in [78]. A detailed description of different channel errors can be found in [29] or [28].
If the definition in equation (5.23) is used to derive the channel correlation for sea data, the following numerator has to be considered

$$\begin{aligned}E\left\{Z_n(F_c) Z_{n'}^H(F_c)\right\} = \sigma_c^2 \exp\left\{j\frac{2\pi}{\lambda_r} u_0(F_c)(x_n - x_{n'})\right\} \\ E\left\{\left|D\left(u_0(F_c) + \frac{V_s(u)}{v_p}\right)\right|^2 \exp\left\{j\frac{2\pi}{\lambda_r}\frac{V_s(u)}{v_p}(x_n - x_{n'})\right\}\right\}.\end{aligned} \tag{5.28}$$

If the radial sea scatterer velocity influence on the antenna modulation due to the two-way antenna pattern can be neglected, then the denominator is equal to the one in equation (5.24), and the numerator is

$$E\left\{Z_n(F_c) Z_{n'}^H(F_c)\right\} = \sigma_c^2 \left|D\left(u_0(F_c)\right)\right|^2 E\left\{\exp\left\{j\frac{2\pi}{\lambda_r}\frac{V_s(u)}{v_p}(x_n - x_{n'})\right\}\right\}, \tag{5.29}$$

where the constant exponential term is compensated for. The difference between land and sea data correlation is the additional exponential term, which has to be considered for sea clutter. To calculate this term, the distribution of the sea scatterer velocity has to be known. Here a Gaussian distribution is assumed, as described in (C.5), which allows to state the numerator as

$$\begin{aligned}E\left\{Z_n(F_c) Z_{n'}^H(F_c)\right\} &= \frac{\sigma_c^2 \left|D\left(u_0(F_c)\right)\right|^2}{\sqrt{2\pi}\sigma_s} \int_{-\infty}^{\infty} \exp\left\{-\frac{v_s^2}{2\sigma_s^2} + j\frac{2\pi}{\lambda_r}\frac{v_s}{v_p}(x_n - x_{n'})\right\} dv_s \\ &= \sigma_c^2 |D(u_0(F_c))|^2 \exp\left\{-\frac{2\pi^2}{\lambda_r^2}\frac{\sigma_s^2}{v_p^2}(x_n - x_{n'})^2\right\}.\end{aligned} \tag{5.30}$$

Here the relationship

$$\int_{-\infty}^{\infty} \exp\left\{ax^2 + bx + c\right\}\, dx = \sqrt{\frac{\pi}{a}} \exp\left\{\frac{b^2 + 4ac}{4a}\right\} \tag{5.31}$$

is used, which can for example be found in [79], to evaluate the integral. With equation (5.30) the sea data channel correlation is derived as

$$\rho_s = \frac{\exp\left\{-\frac{2\pi^2}{\lambda_r^2}\frac{\sigma_s^2}{v_p^2}(x_n - x_{n'})^2\right\}}{1 + \frac{1}{CNR_n}}. \tag{5.32}$$

Equation (5.32) shows the fundamental difference between channel correlations of land and sea data. While under ideal experiment conditions, land data decorrelates only due to noise, for sea data there is an additional decorrelation source due to the movement of the sea scatterers. Hence, the channel correlation of sea data is expected to be always lower than the one of land data. Equation (5.32) also demonstrates that sea data channel correlation is dependent on the sea scatterer velocity variance and the separation between channels n and n'. Consequently, different channel correlations for different sea states and different channel displacements are expected. In [37] it is also analyzed how the channel correlation of sea clutter relates to the eigenvalues of the sea clutter spectral density matrix.

If the influence of the radial sea scatterer velocity on the amplitude modulation due to the two-way antenna pattern cannot be neglected, the antenna pattern function has to be known. Here a Gauss function is assumed for the absolute squared value of the two-way antenna pattern as described by equation (C.6). The denominator of equation (5.23) has then to be stated as

$$E\left\{|Z_n(F_c)|^2\right\} = \frac{\sigma_c^2}{\sqrt{2\pi}\sigma_s} \int_{-\infty}^{\infty} \exp\left\{-\frac{\left(u_0(F_c) + \frac{v_s}{v_p}\right)^2}{2\sigma_a^2}\right\} \exp\left\{-\frac{v_s^2}{2\sigma_s^2}\right\}\, dv_s + \sigma_n^2 \tag{5.33}$$

and the numerator equals to

$$E\left\{Z_n(F_c) Z_{n'}^H(F_c)\right\} = \frac{\sigma_c^2}{\sqrt{2\pi}\sigma_s} \int_{-\infty}^{\infty} \exp\left\{-\frac{\left(u_0(F_c) + \frac{v_s}{v_p}\right)^2}{2\sigma_a^2}\right\} \exp\left\{j\frac{2\pi}{\lambda_r}\frac{v_s}{v_p}(x_n - x_{n'})\right\} \exp\left\{-\frac{v_s^2}{2\sigma_s^2}\right\}\, dv_s. \tag{5.34}$$

To evaluate the integrals in equations (5.33) and (5.34), the relationship in equation (5.31) is applied and a centroid position at 0 Hz is assumed. This allows to calculate the denominator and the numerator of equation (5.23) as

$$E\left\{|Z_n(F_c)|^2\right\} = \sigma_c^2 \frac{\sigma_a}{\sqrt{\sigma_a^2 + \frac{\sigma_c^2}{v_p^2}}} |D(u_0(F_c))|^2 + \sigma_n^2 \tag{5.35}$$

and

$$E\left\{Z_n(F_c)Z_{n'}^H(F_c)\right\} = \sigma_c^2 \frac{\sigma_a}{\sqrt{\sigma_a^2 + \frac{\sigma_c^2}{v_p^2}}} |D(u_0(F_c))|^2 \exp\left\{-\frac{2\pi^2}{\lambda_r^2}\frac{\sigma_s^2}{v_p^2}\frac{\sigma_a^2(x_n - x_{n'})^2}{\left(\frac{\sigma_s^2}{v_p^2} + \sigma_a^2\right)}\right\}. \tag{5.36}$$

With these calculations, the channel correlation of sea clutter can be derived as

$$\rho_s = \frac{\exp\left\{-\frac{2\pi^2}{\lambda_r^2}\frac{\sigma_s^2}{v_p^2}k(x_n - x_{n'})^2\right\}}{1 + \frac{1}{CNR_n}}, \tag{5.37}$$

where $k = \frac{\sigma_a^2}{\left(\frac{\sigma_s^2}{v_p^2} + \sigma_a^2\right)}$. The difference between this channel correlation and the one in equation (5.32), where the influence on the amplitude modulation due to the two-way antenna pattern is neglected, is that here $k \neq 1$. If $\frac{\sigma_s^2}{v_p^2}$ is much smaller than σ_a^2, the quotient of k can be neglected and the channel correlation in equation (5.37) reduces to the one in equation (5.32). This coincides with the observation that only for high velocity variances the influence of the sea scatterer velocity on the amplitude modulation has to be considered, as shown in section 5.2.

5.5 Impact of Fast Scatterers

In the previous sections of this chapter, the multichannel analysis was only derived for slow scatterers. In chapter 3.4, however, also an additional scattering type, the so-called fast scatterers, has been specified. To consider the impact of fast scatterers on the multichannel properties, the clutter signal of equation (5.3) is altered to

$$\begin{aligned}\mathbf{c}(T) = &\int_\Omega A(u)\exp\{j2\pi\mathcal{F}(u, V_s(u))T\}\mathbf{d}(u)\,du \\ &+ B\int_\Omega A_f(u)\exp\{j2\pi\mathcal{F}(u, V_f(u))T\}\mathbf{d}(u)\,du.\end{aligned} \tag{5.38}$$

Here the first term is the contribution of slow scatterers and the second one is due to fast scatterers. The complex echo amplitude of fast scatterers is denoted by $A_f(u)$, which is assumed to be spatially white, zero mean and independent of the reflectivity of slow scatterers $A(u)$ and the velocity of fast scatterers. The radial velocity of fast scatterers $V_f(u)$ is modeled as a random variable, which has the expected value μ_f and the variance σ_f^2. Note that unlike for slow scatterers, the fast scatterer velocity is not considered to be zero mean. As described in chapter 3.4, the velocity of fast scatterers is much faster than the one of slow scatterers. The Doppler frequency of fast scatterers is of random nature and corresponds to

$$\mathcal{F}(u, V_f(u)) = \frac{2v_p}{\lambda_r}u - \frac{2}{\lambda_r}V_f(u). \tag{5.39}$$

The variable B denotes a Bernoulli random variable (see for example [80]) with the expected value μ_B. The realization of this random variable can either have the value 0 or 1 and models if fast scatterers are present at the observed range bin or not. The expected value μ_B corresponds to how many wave breakings occurred in the observed scene.
The overall clutter spectral density matrix can be calculated from the sum of the spectral density matrices of both scatterer types, due to the independence of their amplitudes

$$\mathbf{C}_c(F) = \mathbf{C}_s(F) + \mathbf{C}_f(F). \tag{5.40}$$

Here the spectral density matrix of slow scatterers is defined in equation (5.15). The spectral density matrix of fast scatterers can be derived in a similar way as the one of slow scatterers

$$\begin{aligned}
\mathbf{C}_f(F) &= \int_{-\infty}^{\infty} E\Bigg\{ B^2 \int_{\Omega} A_f(u) A_f^H(u) \mathbf{d}(u)\mathbf{d}^H(u) \\
&\qquad\qquad \exp\left\{ j2\pi(\mathcal{F}(u, V_f(u)) - F)\tau \right\} \, du \Bigg\} \, d\tau \\
&= \mu_B \sigma_{cf}^2 E\left\{ \int_{\Omega} \mathbf{d}(u)\mathbf{d}^H(u)\delta(F - \mathcal{F}(u, V_f(u))) \, du \right\} \\
&= \mu_B \sigma_{cf}^2 E\left\{ \mathbf{d}\left(u_0(F) + \frac{V_f(u)}{v_p} \right) \mathbf{d}^H\left(u_0(F) + \frac{V_f(u)}{v_p} \right) \right\}.
\end{aligned} \tag{5.41}$$

The variance of $A_f(u)$ is denoted by σ_{cf}^2 and the property $E\left\{B^2\right\} = \mu_B$ of a Bernoulli random variable is used. The number of occurring wave breaking events is independent of the reflectivity or velocity of fast scatterers. The fast scatterer velocity distribution is expected to be independent of the look direction. Due to the non-negligible mean of the radial fast scatterer velocity, the Taylor approximation of the DOA vector is performed at $u_f(F) = u_0(F) + \frac{\mu_f}{v_p}$ resulting in

$$\mathbf{e}\left(u_f(F) + \frac{V_f(u)}{v_p} - \frac{\mu_f}{v_p} \right) \approx \mathbf{e}(u_f(F)) + \left(\frac{V_f(u)}{v_p} - \frac{\mu_f}{v_p} \right) \mathbf{e}'(u_f(F)). \tag{5.42}$$

Further, only the deterministic part of the fast scatterer velocity is considered for the influence of the amplitude modulation by the two-way antenna pattern. The described simplifications and the approximation with the Taylor series reduce the spectral density matrix of fast scatterers to

$$\begin{aligned}
\mathbf{C}_f(F) &\approx \sigma_{cf}^2 \mu_B \left| D\left(u_f(F)\right) \right|^2 \left(\mathbf{e}(u_f(F))\mathbf{e}^H(u_f(F)) + \frac{\sigma_f^2}{v_p^2} \mathbf{e}'(u_f(F))\mathbf{e}'^H(u_f(F)) \right) \\
&= \sigma_{cf}^2 \mu_B \left(\mathbf{d}\left(u_f(F)\right) \mathbf{d}^H\left(u_f(F)\right) + \frac{\sigma_f^2}{v_p^2} \mathbf{d}'\left(u_f(F)\right) \mathbf{d}'^H\left(u_f(F)\right) \right).
\end{aligned} \tag{5.43}$$

The eigenvectors of this matrix are multiples of $\mathbf{e}\left(u_f(F)\right)$ and $\mathbf{e}'\left(u_f(F)\right)$, which differ from the ones of the spectral density matrix of slow scatterers $\mathbf{C}_s(F)$. The overall eigenvalues of the clutter spectral density matrix $\mathbf{C}_c(F)$ can therefore not easily be calculated analytically. For this analysis, it is assumed that the contribution of fast scatterers is much smaller than the one of slow scatterers. This assumption is justified due to the fact that wave breaking, which produces fast scatterers, only occurs at single positions, while slow scatterers are always present. Then the properties of $\mathbf{C}_c(F)$ can be calculated by using the perturbation method, where $\mathbf{C}_s(F)$ is the original matrix and $\mathbf{C}_f(F)$ is the perturbation matrix. A detailed description of the perturbation theory for eigenvalue problems can for example be found in [81] or [82]. For the sake of completeness, the related aspects of this method are summarized in appendix E. With this method the first order perturbation of the second eigenvalue due to fast scatterers, as described by equation (E.5), can be calculated as

$$\lambda_{2,f}(F) = \frac{\mathbf{e}'^H(u_0(F))\mathbf{C}_f(F)\mathbf{e}'(u_0(F))}{||\mathbf{e}'(u_0(F))||^2}. \tag{5.44}$$

For simplicity, the second term of equation (5.43) is neglected, because this term is much smaller than the first one and the overall contribution of $\mathbf{C}_f(F)$ is considered to be small. Then the second eigenvalue of $\mathbf{C}_c(F)$ can be calculated as

$$\begin{aligned}\lambda_2(F) &= \frac{\sigma_c^2\sigma_s^2}{v_p^2}||\mathbf{d}'(u_0(F))||^2 + \lambda_{2,f}(F) \\ &= \frac{\sigma_c^2\sigma_s^2}{v_p^2}||\mathbf{d}'(u_0(F))||^2 + \mu_B\sigma_{cf}^2\kappa(F)\left|D\left(u_f(F)\right)\right|^2,\end{aligned} \tag{5.45}$$

where $\kappa(F) = \frac{\left|\mathbf{e}'^H(u_0(F))\mathbf{e}\left(u_f(F)\right)\right|^2}{||\mathbf{e}'(u_0(F))||^2}$. Here the first term is due to slow scatterers and the second one due to fast scatterers. On one hand, this equation shows that there is an extra contribution to the second eigenvalue due to fast scatterers. This implies an additional broadening of the space-time filter notch due to this scattering type. On the other hand, this equation suggests that the contribution of fast scatterers is centered around the frequency $F = \frac{2v_p}{\lambda_r}u - \frac{2}{\lambda_r}\mu_f$, due to the shifted centroid of the clutter Doppler spectrum. Therefore an asymmetrical second eigenvalue distribution in dependence of the frequency is expected, if fast scatterers are present, which also results in an asymmetrical broadness of the space-time filter notch. Figure 5.8 shows the implication of this calculation. Here the space-time filter gain is calculated with the second eigenvalue from equation (5.45). This figure shows that due to an asymmetrical distribution of the second eigenvalue, the broadness of the space-time filter notch is also asymmetrical.

Another important implication of the presence of fast scatterers is the fact that the received power of this clutter type is distributed over other subspace dimensions of the spectral density matrix. At dimension n there is a contribution of $\frac{\mathbf{u}_n^H(F)\mathbf{C}_f(F)\mathbf{u}_n(F)}{||\mathbf{u}_n(F)||^2}$ from fast scatterers, where $\mathbf{u}_n(F)$ is the n-th eigenvector of the slow scatterer spectral density matrix.

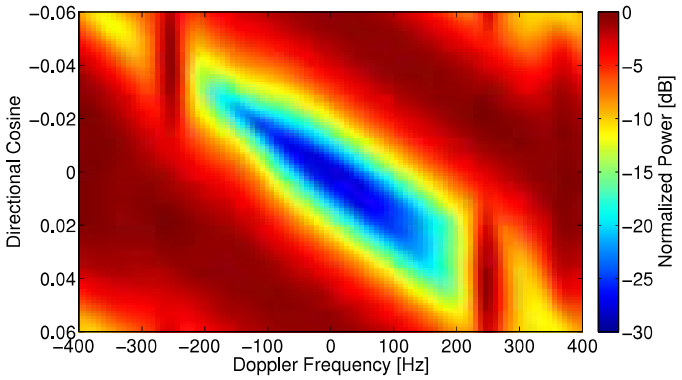

Figure 5.8: Calculated normalized space-time filter gain with calculated second eigenvalue from equation (5.45)

It is demonstrated in figure 5.9 how the multichannel properties change due to fast scatterers. Here the power of a CPI, where the sea scatterers are moving in the up swell direction, is projected on estimated eigenvectors of the clutter spectral density matrix. This CPI contains also 128 pulses, but a PRF of 2000 Hz is used to avoid any changes of the characteristics of fast scatterers in time. Figure 5.9(a) shows the incoherent sum of all subspace dimensions. In this data set fast scatterers are visible due to their high Doppler shift, which is centered around positive Doppler frequencies. Figures 5.9(a) and 5.9(b) visualize a significant difference between the sum of the power and the power projected on the first eigenvector. The reason for this observation is that many clutter returns are positioned on other eigenvectors than the first one. Figure 5.9(c) demonstrates the projected power on the second eigenvector, where quite high clutter contributions are evident. This is due to the high sea scatterer velocity variance of slow scatterers, as well as due to an additional contribution of fast scatterers. These contributions are evident because of higher returns at positive Doppler frequencies. Figure 5.9(d) shows the projected power on the third eigenvector, where echos of fast scatterers are present. The amount of clutter power along the third eigenvector changes in dependence of the availability of fast scatterers. This is demonstrated by comparing figures 5.6 and 5.9, where in the latter CPI fast scatterers are present while in the first one they are not. As demonstrated in appendix E, due to the contribution of fast scatterers, not only the eigenvalues, but also the eigenvectors change. A multiple of the first eigenvector can be calculated from equations (E.5), (E.8) and (5.16) as

$$\mathbf{u}_1(F) = \mathbf{e}(u_0(F)) + \frac{\mu_B \sigma_{cf}^2 \left|D\left(u_f(F)\right)\right|^2}{\sigma_c^2 \left|D\left(u_0(F)\right)\right|^2} \beta(F) \mathbf{e}'(u_0(F)), \tag{5.46}$$

where $\beta(F) = \frac{\mathbf{e}'^H(u_0(F))\mathbf{e}(u_f(F))\mathbf{e}^H(u_f(F))\mathbf{e}(u_0(F))}{||\mathbf{e}'(u_0(F))||^2(||\mathbf{e}(u_0(F))||^2 - \sigma_s^2/v_p^2||\mathbf{e}'(u_0(F))||^2)}$.

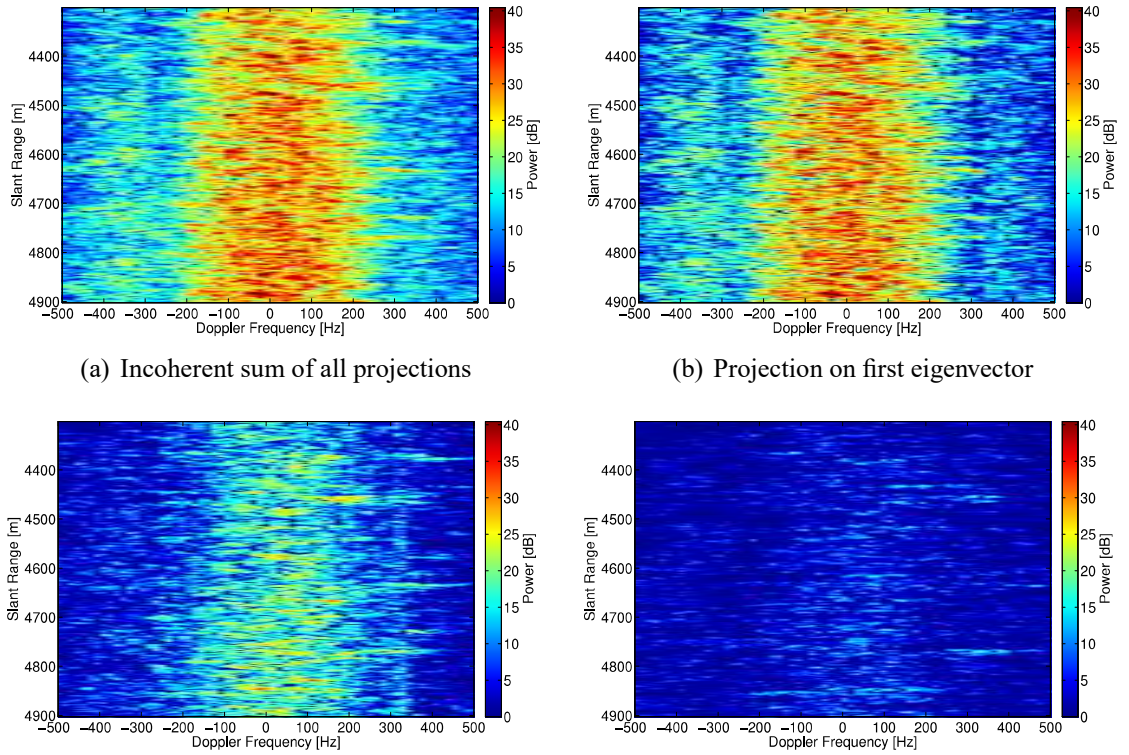

(a) Incoherent sum of all projections

(b) Projection on first eigenvector

(c) Projection on second eigenvector

(d) Projection on third eigenvector

Figure 5.9: Projections of received sea data vector with fast scatterers for different slant ranges and Doppler frequencies on estimated eigenvectors of the clutter plus noise spectral density matrix

Chapter 6

Multichannel Properties of Real and Simulated Data

To validate the multichannel characteristics of sea clutter, this chapter analyzes these properties of real and simulated data. The simulation model is described in section 6.1. To perform simulations of multichannel sea clutter, the radial sea scatterer velocity variance has to be known. Section 6.2 derives therefore an estimator for this measure and in section 6.4 this estimator is applied to all available data sets of the three sea experiments. The multichannel properties of real and simulated sea data are analyzed in section 6.3. The channel correlation of real data is evaluated in section 6.5, where different data sets are compared and the agreement between estimated and calculated correlation coefficients is illustrated. Section 6.6 analyses the multichannel properties of real and simulated data with fast scatterers.

6.1 Simulation Model

Simulations are performed to validate the theoretical multichannel model for sea clutter, which is described in chapter 5. To simulate the received signal, a space-time signal for one iso-range ring and a short coherent processing interval (CPI) is defined as

$$\tilde{\mathbf{z}} = \tilde{\mathbf{c}} + \tilde{\mathbf{n}}. \tag{6.1}$$

The space-time white Gaussian noise vector is denoted by $\tilde{\mathbf{n}}$ and $\tilde{\mathbf{c}}$ is the space-time clutter signal

$$\tilde{\mathbf{c}} = \int_{\Omega} A(u)\tilde{\mathbf{s}}(u, V_s(u))\, du, \tag{6.2}$$

where $\tilde{\mathbf{s}}(u, V_s(u)) = \mathbf{g}(\mathcal{F}(u, V_s(u))) \otimes \mathbf{d}(u)$ is the normalized space-time radar clutter signal. The Kronecker product is denoted by $\otimes$ and $\mathbf{g}(\mathcal{F}(u, V_s(u)))$ is the Doppler vector for sea clutter. This Doppler vector can be defined as

$$\mathbf{g}(\mathcal{F}(u, V_s(u))) = \left(\exp\left\{j2\pi m\mathcal{F}(u, V_s(u))\Delta T\right\}\right)_{m=1}^{M}, \tag{6.3}$$

where ΔT is the pulse repetition interval, $\mathcal{F}(u, V_s(u))$ is the Doppler frequency calculated from equation (5.1), and M is the number of pulses of the CPI. This model can also be used to simulate land clutter if the Doppler frequency is calculated with equation (2.9).
The radar parameters of the simulations are chosen to correspond to those of the experiments. The reflectivity is modeled as a Gaussian distributed complex random variable. The variances of reflectivity and noise are assumed to be $\sigma_c^2 = \sigma_n^2 = 1$. The normalized antenna pattern of one channel is described by si $\left(\pi \frac{L_{tx}}{\lambda_r} u\right)$ si $\left(\pi \frac{L_{rx}}{\lambda_r} u\right)$, where si is the unnormalized sinc function, L_{tx} the transmitting and L_{rx} the receiving antenna length. The antenna gain is chosen to match the CNR of real data and the Doppler centroid is at 0 Hz. The simulated pulses are multiplied with a Hamming window.
To simulate sea data, a Gaussian distribution of the sea scatterer velocity is assumed, as in equation (C.5). To model this distribution, the velocity variance σ_s^2 has to be known. One possibility is to calculate σ_s^2 from the Pierson-Moskowitz spectrum, as shown in equation (3.16). Another possibility is to estimate the velocity variance from real data. This method is described in the next section.

6.2 Estimation of Radial Sea Scatterer Velocity Variance

Several approaches to estimate the radial velocity variance of sea scatterers are treated in the literature. One possible method is described in [59] or [83], where σ_s^2 is estimated from the bandwidth of the clutter spectrum, which is broadened due to this measure. This method is however not very precise, because of the difficulty to discriminate between the broadening due to the movement of the platform and the movement of sea scatterers. An improved method is to estimate the velocity variance from the channel correlation, if several channels are available. This approach is evaluated in [84] and [14]. Different approaches to estimate the velocity variance from real data are also discussed in [85].
In this chapter a new method is proposed, where the velocity variance is estimated from the eigenvalues of the spectral density matrix.
The estimator of the velocity variance is derived using the assumption that the eigenvalues of the clutter spectral density matrix can be described by equation (5.14). Note that this is only valid for sea scatterer velocities, having a Gaussian distribution. With white Gaussian noise and equation (5.14), the estimated eigenvalues of real data are assumed to be

$$\hat{\lambda}_1(F) \stackrel{!}{=} \sigma_c^2 \frac{\sigma_a}{\sqrt{\sigma_a^2 + \frac{\sigma_s^2}{v_p^2}}} ||\mathbf{d}(u_0(F))||^2 + \sigma_n^2 \tag{6.4}$$

$$\hat{\lambda}_2(F) \stackrel{!}{=} \frac{\sigma_c^2 \sigma_s^2}{v_p^2} \frac{\sigma_a^3}{\left(\sigma_a^2 + \frac{\sigma_s^2}{v_p^2}\right)^{(3/2)}} ||\mathbf{d}'(u_0(F))||^2 + \sigma_n^2 \tag{6.5}$$

$$\hat{\lambda}_3(F) = \cdots = \hat{\lambda}_N(F) \stackrel{!}{=} \sigma_n^2. \tag{6.6}$$

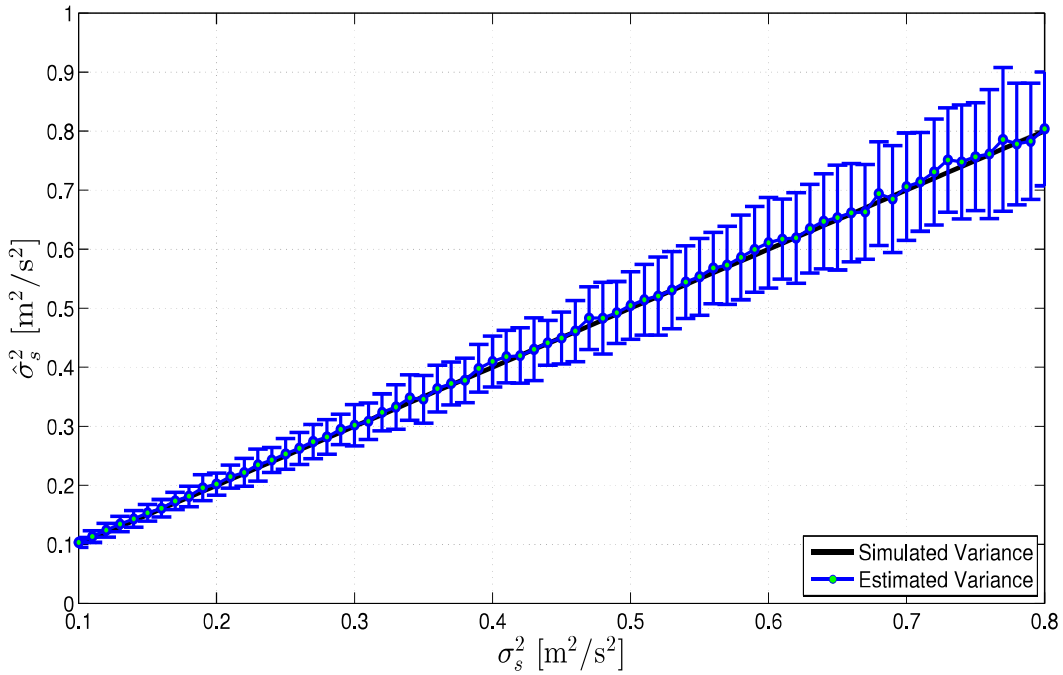

Figure 6.1: Estimated radial sea scatterer velocity variance from simulated data sets. Simulations are performed with the variance σ_s^2, and the estimator from equation (6.8) is applied to estimate $\hat{\sigma}_s^2$. The blue dot indicates the estimated mean radial sea scatterer velocity variance from 100 trials, and the bars display the standard deviation.

The second eigenvalue can be used to estimate σ_s^2. However, also σ_c^2 is not known. This measure can be estimated from the first eigenvalue, which results in

$$\hat{\sigma}_c^2 = \frac{\hat{\lambda}_1(F_c) - \sigma_n^2}{\sigma_a ||\mathbf{d}(u_0(F_c))||^2} \sqrt{\sigma_a^2 + \frac{\sigma_s^2}{v_p^2}}, \tag{6.7}$$

where σ_n^2 is here estimated from the third eigenvalue. The estimation is performed around the Doppler centroid F_c. With equations (6.5), (6.6) and (6.7), the radial sea scatterer velocity variance can be derived as

$$\hat{\sigma_s}^2 = \frac{v_p^2(\hat{\lambda}_2(F_c) - \sigma_n^2)}{\alpha(F_c)(\hat{\lambda}_1(F_c) - \sigma_n^2) - \frac{1}{\sigma_a^2}(\hat{\lambda}_2(F_c) - \sigma_n^2)}, \tag{6.8}$$

where $\alpha(F_c) = \frac{||\mathbf{d}'(u_0(F_c))||^2}{||\mathbf{d}(u_0(F_c))||^2}$.

Figure 6.1 shows the evaluation of the described estimator. Here simulations, as described in section 6.1, are performed with a certain sea scatterer velocity variance. Then the estimator is applied to the simulated data to evaluate how well the variance can be estimated. The black line and the x-axis show the simulated velocity variances and the blue

line indicates the estimated one. The error bars demonstrate the standard deviation for each regarded velocity variance, and the blue dots indicate the estimated mean velocity variance. For each considered velocity variance, 100 simulations are performed. Figure 6.1 shows that the proposed estimator in equation (6.8) on average estimates the velocity variance quite well. The mean error between the simulated and estimated velocity variance is 0.004 m^2/s^2. The standard deviation of this estimator is higher for higher velocity variances, because then the second eigenvalue changes less due to this measure.

6.3 Comparison of Real and Simulated Data

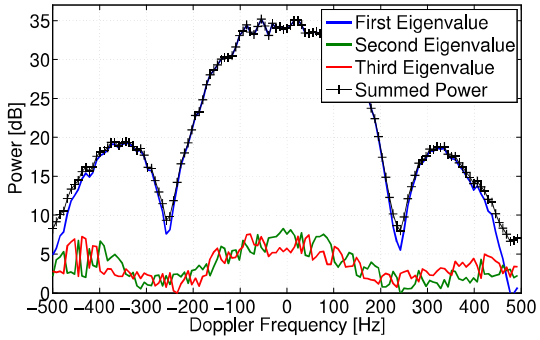

Figure 6.2: Eigenvalue distributions. Real land data, grazing angle 20°.

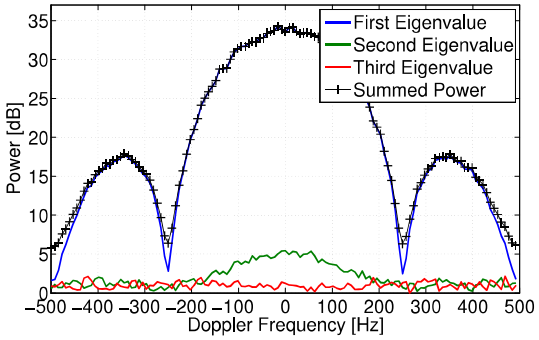

Figure 6.3: Eigenvalue distributions. Simulated land data, matching parameters.

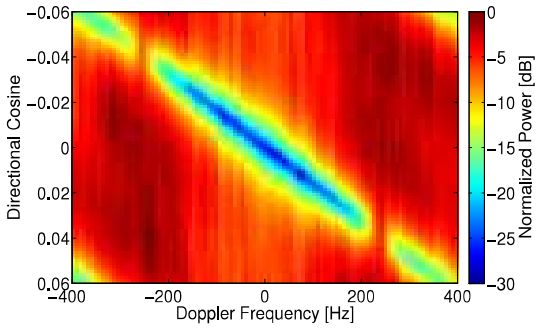

Figure 6.4: Space-time filter gain. Real land data, grazing angle 20°.

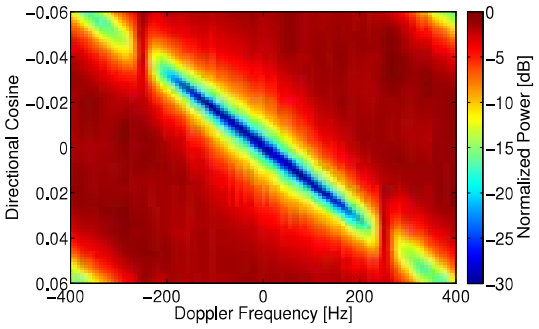

Figure 6.5: Space-time filter gain. Simulated land data, matching parameters.

In this section the multichannel properties of real and simulated data are analyzed. To compare the different data sets, a downsampling to a PRF of 1000 Hz is performed and the Doppler shift due to the platform velocity is removed.
For real sea data additionally the Doppler shift caused by any present currents, modulations of the long waves or the phase velocity of capillary waves, which are described

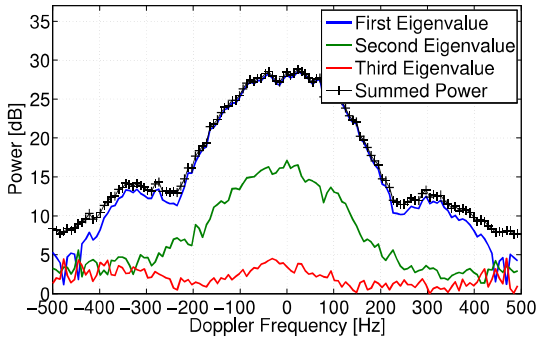

Figure 6.6: Eigenvalue distributions. Real sea data, experiment 3, grazing angle 15°.

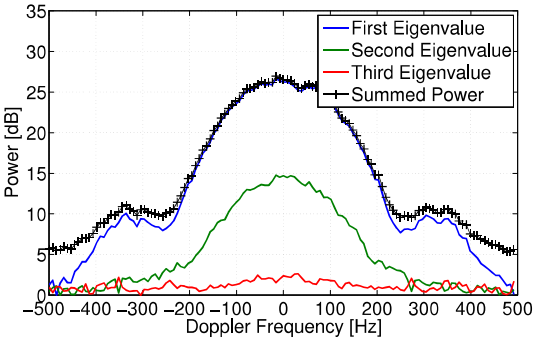

Figure 6.7: Eigenvalue distributions. Simulated sea data, matching parameters.

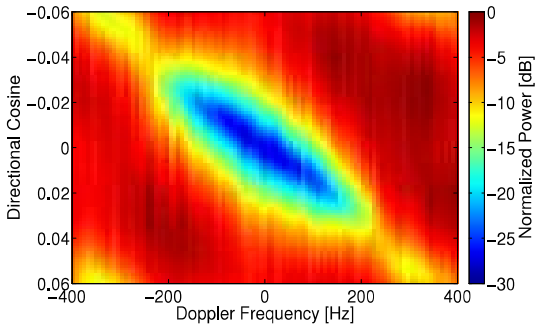

Figure 6.8: Space-time filter gain. Real sea data, exp. 3, grazing angle 15°.

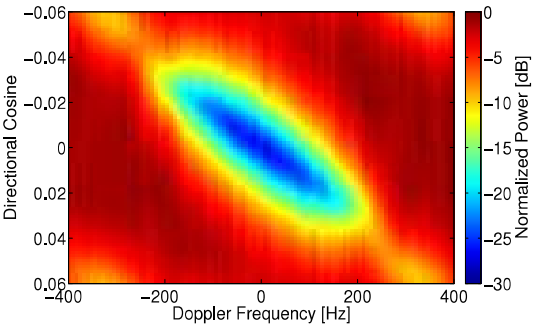

Figure 6.9: Space-time filter gain. Simulated sea data, matching parameters.

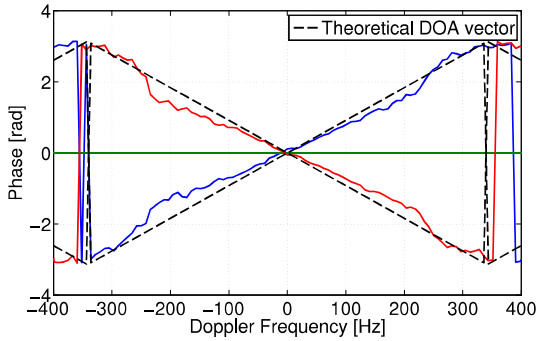

Figure 6.10: Phase of first eigenvector. Real sea data, exp. 3, grazing angle 15°.

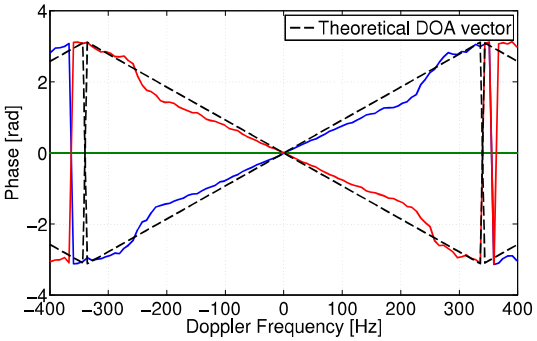

Figure 6.11: Phase of first eigenvector. Simulated sea data, matching parameters.

in chapter 4.3, is eliminated. In figure 6.2 the eigenvalues of land clutter are plotted for different Doppler frequencies of the same CPI as in figure 5.5. Figure 6.3 demonstrates eigenvalue distributions of a simulated data set with matching radar parameters. The black line indicates additionally the summed power of all three channels for each Doppler frequency. For both data sets a very strong first eigenvalue around the Doppler

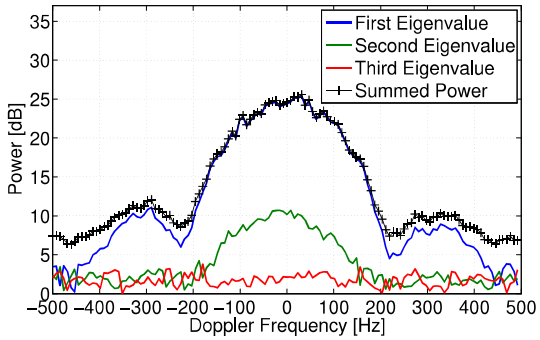

Figure 6.12: Eigenvalue distributions. Real sea data, exp. 2, grazing angle 15°.

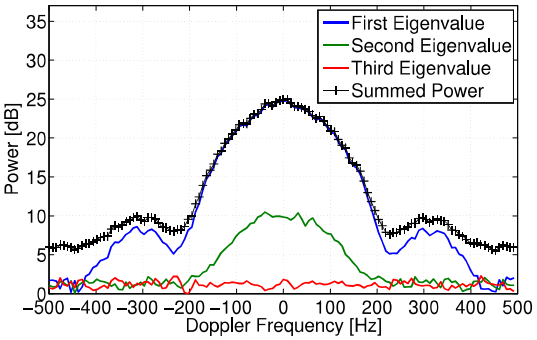

Figure 6.13: Eigenvalue distributions. Simulated sea data, matching parameters.

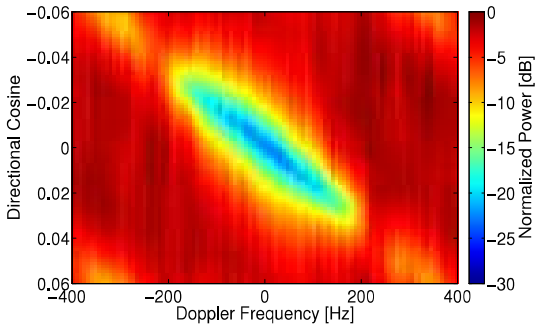

Figure 6.14: Space-time filter gain. Real sea data, exp. 2, grazing angle 15°.

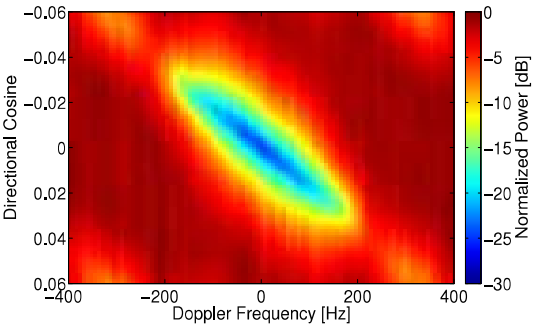

Figure 6.15: Space-time filter gain. Simulated sea data, matching parameters.

centroid is present, while the other two eigenvalues are negligible. The second and third eigenvalue of real land data are higher due to additional channel mismatches, which are not considered by the simulation, but the difference between the first and the other eigenvalues at the Doppler centroid is still 26.5 dB. The eigenvalue distribution of real and simulated land clutter justify that spectral leakage is neglected for the chosen CPI length. Figure 6.4 displays the normalized filter gain of the real land data set and figure 6.5 of the simulated one. The filter notch of both data sets is a diagonal line, as expected due to the demonstrated calculations of a theoretical land filter in figure 5.7.
Figure 6.6 shows eigenvalue distributions of the same sea data as in figure 5.6, and the eigenvalue distributions of a simulated data set with corresponding parameters are visualized in figure 6.7. For both CPIs a pronounced rise of the second eigenvalue can be observed around the Doppler centroid. The difference between the first and second eigenvalue is only 11.3 dB for real data and 11.6 dB for simulated. To simulate this sea data, the radial sea scatterer velocity variance is estimated from the real CPI with equation (6.8) to be $\hat{\sigma}_s^2 = 0.37\ \mathrm{m}^2/\mathrm{s}^2$, which corresponds to a standard deviation of $\hat{\sigma}_s = 0.61$ m/s.

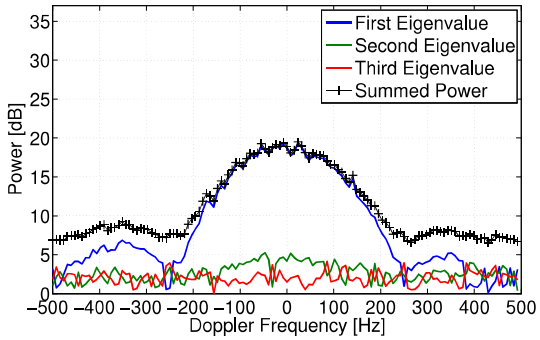

Figure 6.16: Eigenvalue distributions. Real sea data, exp. 1, grazing angle 15°.

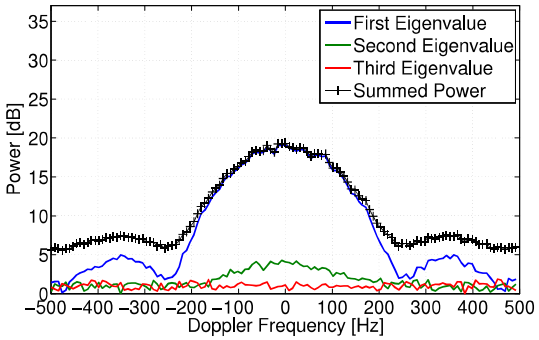

Figure 6.17: Eigenvalue distributions. Simulated sea data, matching parameters.

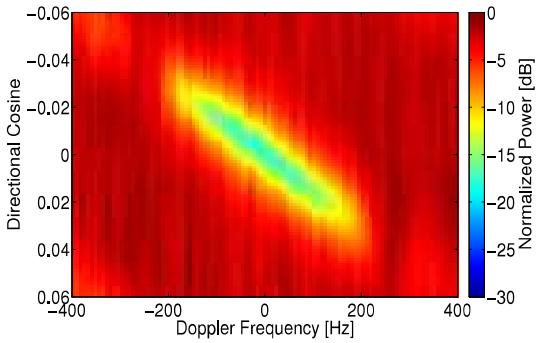

Figure 6.18: Space-time filter gain. Real sea data, exp. 1, grazing angle 15°.

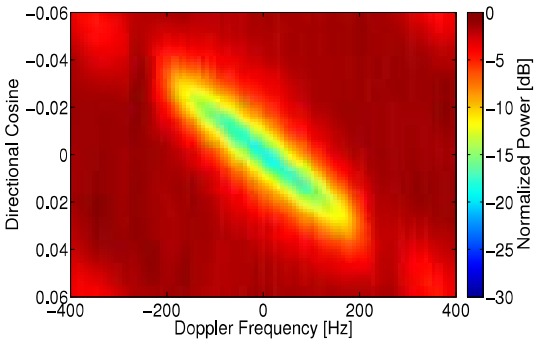

Figure 6.19: Space-time filter gain. Simulated sea data, matching parameters.

Figures 6.8 and 6.9 demonstrate the normalized space-time filter gain of the described real and simulated data. A significant broadening of the filter notch is evident. For each look direction, there is a significantly higher amount of Doppler frequencies where a target would be attenuated or even suppressed by the space-time sea clutter filter. The broadening of the filter notch confirms the calculations performed in chapter 5.3, which predict a broader space-time filter notch for sea clutter than for land clutter.
The phase of the first eigenvector is visualized for real and simulated data in figures 6.10 and 6.11. The dotted black line indicates the phase of the theoretical DOA vector in both figures. The comparison of both phases shows an agreement between the phase of the first eigenvector and the one of the theoretical DOA vector. This coincides with the analysis in chapter 5.2, where the first eigenvector is assumed to equal the DOA vector. The small bends of the estimated first eigenvector phase are analyzed in appendix C.
In figure 6.12 eigenvalue distributions of a real sea data set of experiment 2 are demonstrated. This CPI is processed in the same manner as the CPI of experiment 3. Figure 6.13 shows eigenvalues in dependence of the Doppler frequency of a simulated data set with corresponding radar and sea parameters. Both figures display a significantly lower second eigenvalue around the Doppler centroid. The difference between the first and sec-

ond eigenvalue is 14.4 dB for the real data set and 15.1 dB for the simulated one at 0 Hz. The first eigenvalue is also lower at the Doppler centroid, because the CNR is lower for this experiment, as described in chapter 4.3. From the eigenvalues of this real sea data also a smaller radial sea scatterer velocity variance is estimated, which is equal to $\hat{\sigma}_s^2 = 0.158\ \mathrm{m}^2/\mathrm{s}^2$.
Figures 6.14 and 6.15 show the normalized space-time filter gains of the described sea data sets. The filter notches of real and simulated data are significantly narrower than the filter notches of experiment 3. The consequence of this observation is that for this experiment slower low SCNR targets can be detected than for experiment 3. A change of the broadness of the space-time filter notch in dependence of the radial sea scatterer velocity variance is in accordance with the calculations, which are performed in chapter 5.3 and visualized in figure 5.7.
Figure 6.16 demonstrates eigenvalue distributions of a real CPI of experiment 1. This CPI is also processed in the same manner as the data sets of experiments 2 and 3. The eigenvalue distributions of figure 6.17 are evaluated of a simulated CPI with matching radar and sea parameters. Both figures show a small difference between the second and third eigenvalue around 0 Hz. This indicates a small influence of the sea scatterer velocity on the multichannel properties. The sea scatterer velocity variance is estimated from the real data set as $\hat{\sigma}_s^2 = 0.088\ \mathrm{m}^2/\mathrm{s}^2$, which equals to a standard deviation of $\hat{\sigma}_s = 0.30$ m/s.
Figures 6.6 - 6.17 show significant variations of the second eigenvalue around the Doppler centroid for different experiments. The real and simulated CPIs of experiment 3 display a pronounced second eigenvalue. The CPIs of experiment 2 visualize a less distinct second eigenvalue and the demonstrated second eigenvalue of experiment 1 is almost only due to noise. The second eigenvalue of the different experiments changes due to its dependence on the radial sea scatterer velocity variance. Different sea scatterer velocity variances of the three performed sea experiments are expected, due to different sea states, which were present during the data acquisitions. The influence of the sea state on the radial sea scatterer velocity variance confirms the proportional relationship between this measure and the orbital velocity variance, presented in equation (5.2). The orbital velocity variance is clearly dependent on the sea state. If, for example, the Pierson-Moskowitz spectrum is considered, equation (3.17) shows that the orbital velocity variance increases quadratically with the wind velocity.
Figures 6.19 and 6.18 demonstrate the normalized space-time filter gains of the described CPIs of experiment 1. These figures show a narrower filter notch, but a comparison of the space-time filter gains of the different experiments is difficult due to a changing CNR.
To have a meaningful comparison of the space-time filter gain for different sea scatterer velocity variances, simulations are performed with the same CNR but varying σ_s^2. In figure 6.20 this evaluation is visualized, where the space-time filter gain is plotted for $u = 0$. The blue line shows the filter of simulated land clutter ($\sigma_s^2 = 0$) and the brightly colored lines indicate filters of sea clutter. To simulate the different sea data sets, the same radial sea scatterer velocity variances as the ones estimated from the presented CPIs of the dif-

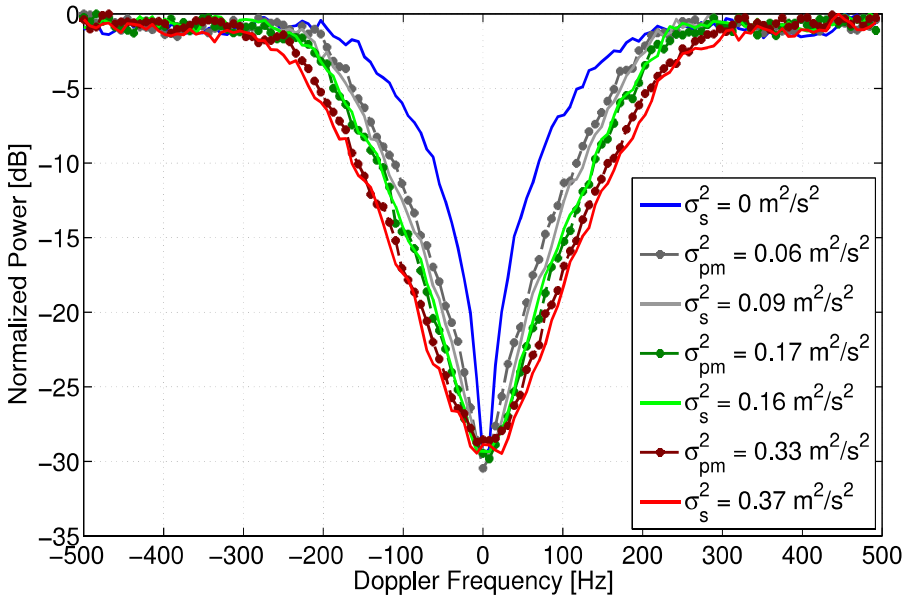

Figure 6.20: Space-time filter gain at $u = 0$ for simulated data sets with same CNR but varying velocity variance.

ferent experiments are used. This figure demonstrates significantly broader filter notches of sea data as compared to land data. Additionally, a broadening with a rising velocity variance is evident.

The dotted lines in figure 6.20 indicate filter gains of sea data sets, which are simulated with theoretically calculated radial sea scatterer velocity variances from equations (3.17) and (5.2), with radar and sea parameters which correspond to the performed sea experiments. This evaluation is performed to show that the multichannel properties of sea clutter can also be simulated if the velocity variance cannot be estimated from real data in advance. To calculate the orbital velocity variance with the Pierson-Moskowitz spectrum from equation (3.17) and to determine the radial sea scatterer velocity variance from the orbital velocity variance with equation (5.2), the maximum recorded swell directions and wind velocities, which are summarized in chapter 4.2, are used. Deviations between calculated and estimated radial sea scatterer velocity variances are present due to unprecise weather data and due to the application of the Pierson-Moskowitz spectrum, which is only an approximation of the real sea surface spectral density. Other approximations of the sea spectral density are more precise, like the JONSWAP spectrum, which is introduced in [86]. Nevertheless, the simulated multichannel characteristics with calculated sea scatterer velocity variances show that a reproduction of the multichannel properties of real sea data is also possible to some extent if an estimation of the sea scatterer velocity variance cannot be performed.

Figure 6.21 demonstrates eigenvalue distributions of a CPI which was acquired during experiment 3 with a grazing angle of 35°. This CPI is processed exactly like the other

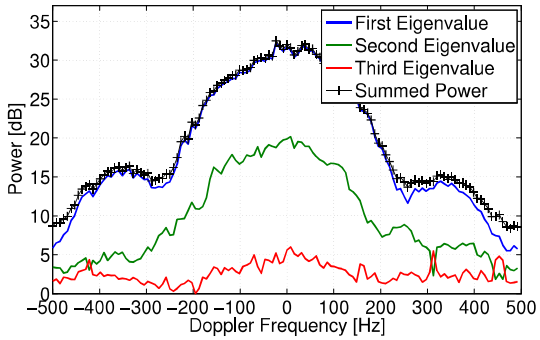

Figure 6.21: Eigenvalue distributions. Real sea data, exp. 3, grazing angle $35°$.

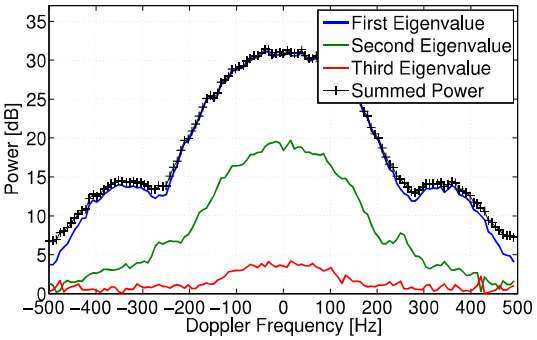

Figure 6.22: Eigenvalue distributions. Simulated sea data, matching parameters.

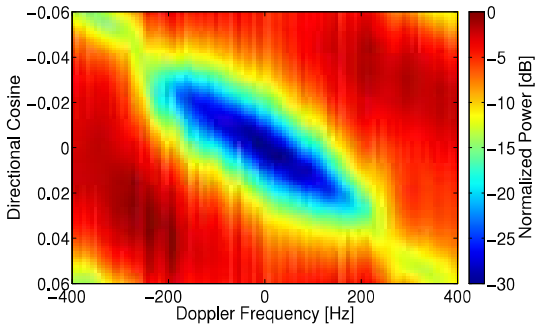

Figure 6.23: Space-time filter gain. Real sea data, exp. 3, grazing angle $35°$.

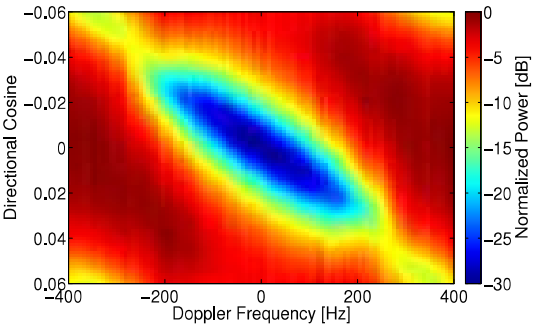

Figure 6.24: Space-time filter gain. Simulated sea data, matching parameters.

data sets in this section. Figure 6.22 visualizes eigenvalue distributions of a simulated CPI with corresponding radar and sea parameters. Both figures show a higher first eigenvalue at the Doppler centroid as compared to data sets collected with the $15°$ grazing angle. This is due to a higher CNR as discussed in chapter 4.3. Also for these CPIs a pronounced second eigenvalue is visible around the Doppler centroid. The difference between the first and second eigenvalue is only 12.1 dB for the real data set and 12.4 dB for the simulated one. The estimated velocity variance corresponds to $\hat{\sigma}_s^2 = 0.423\ \mathrm{m}^2/\mathrm{s}^2$, which is equal to a standard deviation of $\hat{\sigma}_s = 0.65$ m/s.
In figures 6.23 and 6.24 the space-time filter gain of the presented real and simulated data is visualized. A significantly broader filter notch is evident for these data sets than for land clutter. At the look direction $u = 0$, for example, a target with a radial velocity of 1.1 m/s would be attenuated by 11 dB more by the presented filter in figure 6.23 as compared to the land space-time filter shown in figure 6.4.

The comparison of multichannel properties of simulated and real sea data, which are demonstrated in figures 6.6-6.24, illustrates a good agreement. This shows that the multichannel properties of sea clutter can be reproduces with the described simulation model

for different sea states. Furthermore, this evaluation confirms the multichannel sea clutter properties, which are theoretically derived in chapter 5.2.

6.4 Radial Sea Scatterer Velocity Variance of Real Data

The radial sea scatterer velocity variance has a crucial influence on the multichannel characteristics of sea clutter. This measure decides how much the multichannel properties of sea clutter deviate from the ideal properties of land clutter. If fast scatterers are not considered, the velocity variance specifies the magnitude of the second eigenvalue and the decorrelation of the channels in addition to noise. The velocity variance is a measure of the broadness of the space-time filter notch, which determines at which velocities a target can still be detected after sea clutter suppression.
This section presents estimations of velocity variances with the presented estimator in equation (6.8). Here all collected data sets of the three sea experiments are evaluated. The performed estimations are summarized in tables 6.1 - 6.3, where the mean of all estimated velocity variances $E\{\hat{\sigma}_s^2\}$ of one data set, the standard deviation $\sqrt{Var\{\hat{\sigma}_s^2\}}$ of the corresponding data set and the azimuth angle range in ENU coordinates, at which the velocity variance is estimated, are documented.
To estimate the velocity variance, CPIs with 256 pulses are considered at steering angles, which range from 70° - 110° in the platform coordinate system. The eigenvalues are calculated from a spectral density matrix, which is estimated from 200 range bins. The range interval with the highest clutter power is chosen for this estimation. For experiment 3, several range intervals are selected for each CPI. The velocity variance is estimated from each range interval and an average is calculated. This is performed to mitigate the influence of fast scatterers.
The mean velocity variance is calculated from 150 - 250 trials, depending on the available number of CPIs for the desired steering angle range. The velocity variance is assumed not to change due to the azimuth angle within the observed interval. Unfortunately, the data acquisition during experiment 1 at side 2 with the grazing angle of 15° was not successful.
Tables 6.1 - 6.3 show that the mean velocity variance changes significantly for different experiments. The estimated velocity variance interval ranges from 0.075 m^2/s^2 to 0.125 m^2/s^2 for the first experiment, from 0.141 m^2/s^2 to 0.231 m^2/s^2 for the second one and is equal to 0.360 m^2/s^2 - 0.514 m^2/s^2 for the third experiment. Different velocity variances are evaluated for different experiments due to unequal sea state, during these experiments. The orbital velocity variance depends on the weather and sea conditions, and the radial sea scatterer velocity variance is proportional to the orbital velocity variance.
A higher velocity variance is expected for in swell directions due to equation (5.2). Additionally, for the cross swell direction a higher velocity variance should be present for the grazing angle of 35° as opposed to 15°. While such a tendency can be observed regarding the estimations of experiment 3, for the other experiments this dependence is not

	φ_{ENU} [°]	$E\{\hat{\sigma}_s^2\}$ [m²/s²]	$\sqrt{Var\{\hat{\sigma}_s^2\}}$ [m²/s²]
$\theta = 35°$, side 1	50 - 95	0.102	0.025
$\theta = 35°$, side 2	340 - 25	0.100	0.023
$\theta = 35°$, side 3	255 - 300	0.105	0.029
$\theta = 35°$, side 4	310 - 355	0.102	0.021
$\theta = 15°$, side 1	70 - 105	0.075	0.015
$\theta = 15°$, side 3	260 - 295	0.110	0.019
$\theta = 15°$, side 4	165 - 200	0.125	0.017

Table 6.1: Estimated radial sea scatterer velocity variance of experiment 1

	φ_{ENU} [°]	$E\{\hat{\sigma}_s^2\}$ [m²/s²]	$\sqrt{Var\{\hat{\sigma}_s^2\}}$ [m²/s²]
$\theta = 35°$, side 1	65 - 105	0.185	0.027
$\theta = 35°$, side 2	350 - 25	0.141	0.022
$\theta = 35°$, side 3	265 - 305	0.197	0.034
$\theta = 35°$, side 4	170 - 205	0.197	0.032
$\theta = 15°$, side 1	70 - 105	0.231	0.035
$\theta = 15°$, side 2	350 - 25	0.144	0.014
$\theta = 15°$, side 3	260 - 295	0.198	0.024
$\theta = 15°$, side 4	175 - 200	0.214	0.029

Table 6.2: Estimated radial sea scatterer velocity variance of experiment 2

	φ_{ENU} [°]	$E\{\hat{\sigma}_s^2\}$ [m²/s²]	$\sqrt{Var\{\hat{\sigma}_s^2\}}$ [m²/s²]
$\theta = 35°$, side 1	50 - 95	0.473	0.085
$\theta = 35°$, side 2	310 - 355	0.432	0.065
$\theta = 35°$, side 3	210 - 255	0.504	0.067
$\theta = 35°$, side 4	130 - 175	0.401	0.046
$\theta = 15°$, side 1	50 - 85	0.450	0.084
$\theta = 15°$, side 2	315 - 350	0.434	0.055
$\theta = 15°$, side 3	210 - 250	0.514	0.068
$\theta = 15°$, side 4	130 - 165	0.360	0.034

Table 6.3: Estimated radial sea scatterer velocity variance of experiment 3

distinct. The reason for the observed discrepancies are considered to be the unprecise weather condition measurements, which were collected once an hour and not exactly at the observed scene. The collected weather information is considered to be sufficient to compare the different experiments with each other, but not precise enough to allow any conclusions concerning the data sets of the different sides of one experiment. For such

an analysis more precise in-situ measurements would be needed.
The radial sea scatterer velocity variance is also a crucial measure for SAR imaging. This measure determines the azimuth resolution of a sea surface SAR image (see for example [15] or [12]). In literature this measure is often referred to as the coherence time. The relationship between the coherence time and the sea scatterer velocity variance is given as ([12], [87])

$$\tau_s = \frac{\lambda_r}{2\pi\sqrt{2\sigma_s^2}}, \tag{6.9}$$

which is valid if the time auto-correlation function of sea scatterers can be assumed to be Gaussian.
In literature several attempts to estimate the coherence time can be found ([13, 84, 14]). In [84] the coherence time is estimated from two along-track channels, and in [14] two channels with a switching technique are used to achieve a dual baseline. The estimations of both publications are performed in L-band with obtained velocity variances of 0.052 m^2/s^2 - 0.126 m^2/s^2 in [84] and 0.026 m^2/s^2 - 0.317 m^2/s^2 in [14].

6.5 Channel Correlation of Real Data

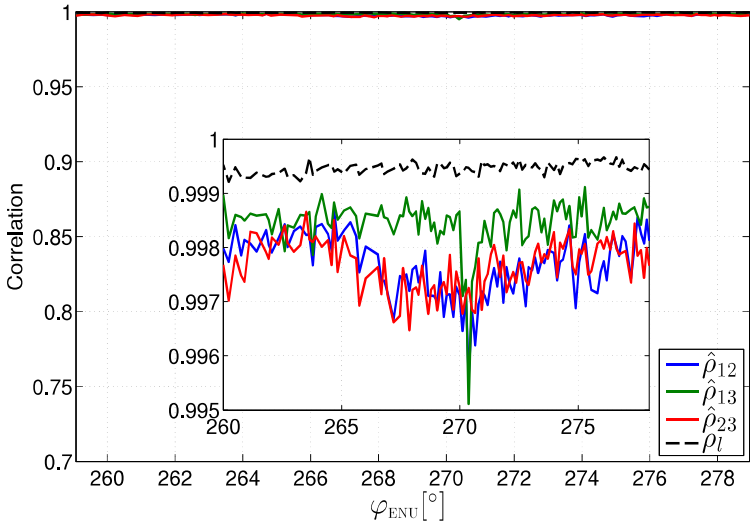

Figure 6.25: Channel correlation of land data for different azimuth angles. Estimated correlation (colored lines) and theoretical correlation for land data (black line).

To evaluate the channel correlation from real range compressed data, coherent processing intervals with 256 pulses are chosen to apply a Fourier transform. The channel correlation is estimated from 200 range bins. The pulses are multiplied with a Hamming window to mitigate spectral leakage. The cable length and system delays are compensated for each channel. The Doppler shift due to the platform velocity is removed, and for sea data

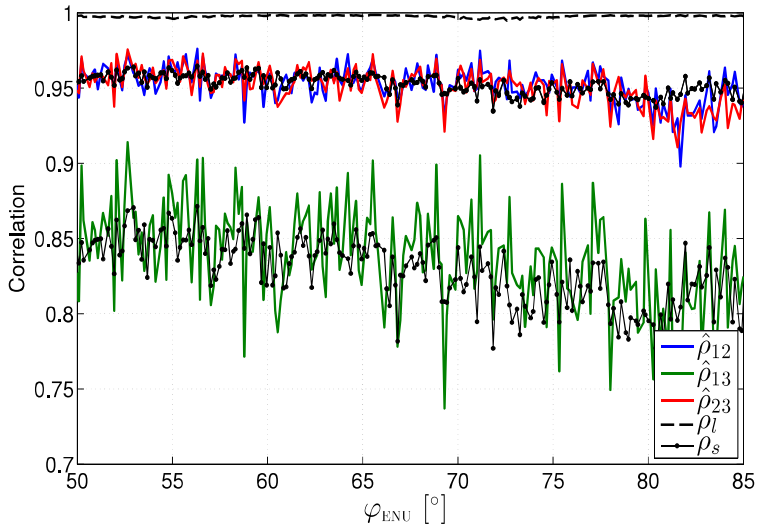

Figure 6.26: Channel correlation of sea data for different azimuth angles. Experiment 3, side 1, grazing angle $15°$. Estimated correlation (colored lines) and theoretical correlation for land data (dashed black line) and sea data (dotted black line).

additionally the Doppler shift caused by any sea scatterer velocities is eliminated. The channel correlation is evaluated in dependency of the azimuth angle φ_{ENU}, which is the angle between the x-axis and the line-of-sight vector to the center position in the ENU coordinate system.
In figure 6.25 the channel correlation of real land data is plotted for different azimuth angles. Here a scale is chosen to match the channel correlation of sea data. Additionally, a second figure is inserted with a more appropriate scale to view the land data channel correlation. The colored lines show the estimated correlation coefficients using equation (5.23) and the dashed black line indicates the calculated channel correlation from equation (5.27), which calculates the decorrelation due to noise. Figure 6.25 shows highly correlated channels, where the mean correlation coefficients are equal to $E\{\hat{\rho}_{12}\} = 0.997$, $E\{\hat{\rho}_{13}\} = 0.998$ and $E\{\hat{\rho}_{23}\} = 0.997$. These mean values suggest equal correlation between all channels. Additionally, in figure 6.25 a match between the calculated and estimated channel correlations is visible, where the mean of the calculated channel correlation is equal to $E\{\rho_l\} = 0.999$. The described evaluation validates equation (5.27) and suggests that noise is the only decorrelation source for the described land data set.
Figure 6.26 shows the channel correlation of a real sea data set, which was collected during experiment 3 with the grazing angle of $15°$. Here again the colored lines indicate the estimated channel correlation from equation (5.23) and the dashed black line shows the calculated channel correlation from equation (5.27). Additionally, the dotted black line visualizes the calculated channel correlation from equation (5.37), which is derived for sea data. In figure 6.26 a significantly lower channel correlation for sea data is visible as compared to land data. The estimated channel correlation is also much lower than the

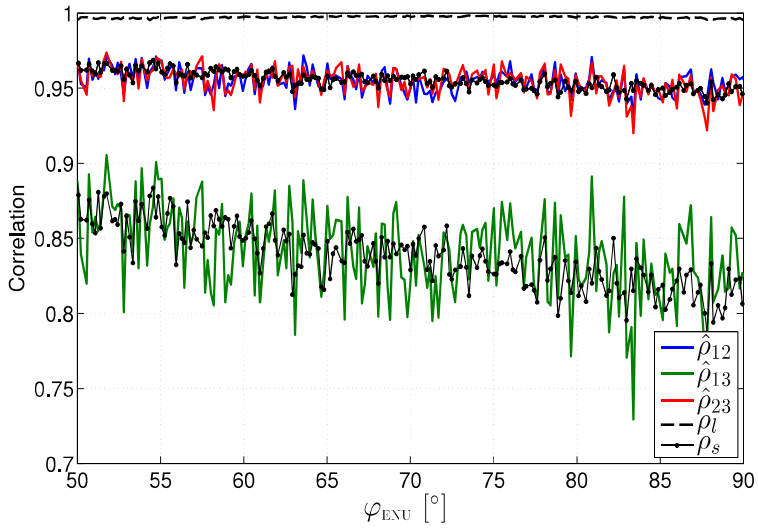

Figure 6.27: Channel correlation of sea data for different azimuth angles. Experiment 3, side 1, grazing angle $35°$. Estimated correlation (colored lines) and theoretical correlation for land data (dashed black line) and sea data (dotted black line).

calculated one from equation (5.27), indicating a further source of decorrelation for sea data than just noise. Another striking property of the estimated sea data channel correlation are the significantly different correlation coefficients between channels 1 and 3, as compared to the other channels, which is due to different phase center separations. Channels 1 and 2 and channels 2 and 3 are equidistant. The phase center separation between channels 1 and 3 is however twice as big. As derived in equation (5.37), higher phase center separations result in lower channel correlations. This is crucially different from land data, where this measure is expected to be independent of the channel separation. A match of the calculated correlation coefficients from equation (5.37) and the estimated ones is evident, where also different values are calculated for different phase center separations.

To determine the channel correlation of sea data, the radial sea scatterer velocity variance has to be known. For this calculation the sea scatterer velocity variance is estimated from equation (6.8). Note that it would also be possible to estimate the velocity variance from the estimated channel correlations. This estimator is however not applied here, because it has a higher variance than the proposed estimator.

The mean correlation coefficients, which are presented in figure 6.26, are $E\{\hat{\rho}_{12}\} = 0.952$, $E\{\hat{\rho}_{23}\} = 0.951$ and $E\{\hat{\rho}_{13}\} = 0.836$. The mean calculated sea data correlation coefficients are 0.953 and 0.832 for the two phase center separations. If the sea data channel correlation for this data set is calculated without considering the influence of the radial sea scatterer velocity on the antenna pattern, the mean values for both channel separations would be 0.940 and 0.786. These values indicate that the antenna pattern cannot be neglected when considering the channel correlation.

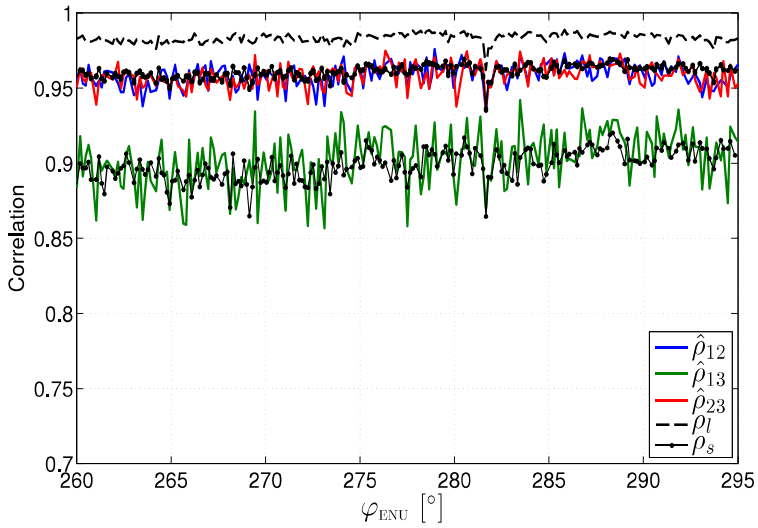

Figure 6.28: Channel correlation of sea data for different azimuth angles. Experiment 2, side 3, grazing angle $15°$. Estimated correlation (colored lines) and theoretical correlation for land data (dashed black line) and sea data (dotted black line).

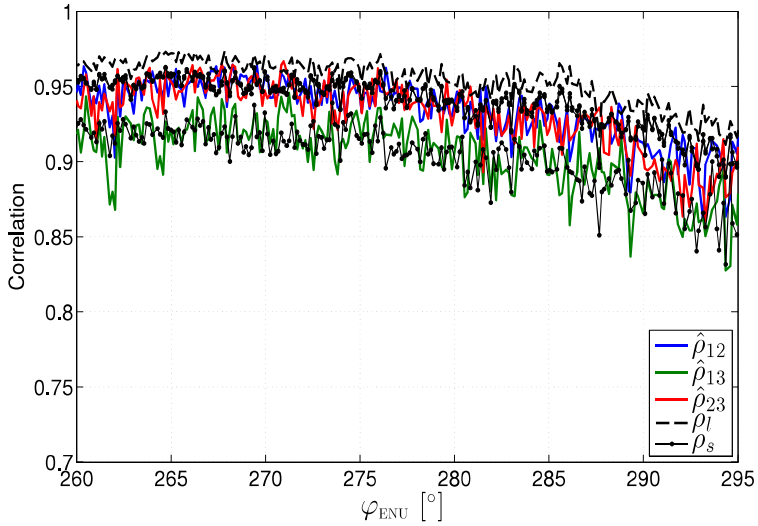

Figure 6.29: Channel correlation of sea data for different azimuth angles. Experiment 1, side 3, grazing angle $15°$. Estimated correlation (colored lines) and theoretical correlation for land data (dashed black line) and sea data (dotted black line).

Figure 6.27 shows channel correlation coefficients for different azimuth angles of a sea data set collected during experiment 3 with the grazing angle of $35°$. This figure demonstrates same properties for this grazing angle as compared to the grazing angle of $15°$. The correlation of the channels is lower compared to land data, resulting in a discrepancy between estimated channel correlations and the theoretical channel correlation of land

	$E\{\hat{\rho}_{12}\}$	$E\{\hat{\rho}_{23}\}$	$E\{\hat{\rho}_{13}\}$	$E\{\rho_l\}$	$E\{\rho_s\}$
$\theta = 35°$, side 1	0.966	0.965	0.936	0.981	0.968/ 0.933
$\theta = 35°$, side 2	0.957	0.956	0.929	0.971	0.958/ 0.925
$\theta = 35°$, side 3	0.970	0.969	0.938	0.984	0.971/ 0.935
$\theta = 35°$, side 4	0.968	0.966	0.938	0.981	0.969/ 0.936
$\theta = 15°$, side 1	0.953	0.952	0.932	0.967	0.957/ 0.931
$\theta = 15°$, side 3	0.942	0.941	0.913	0.960	0.947/ 0.911
$\theta = 15°$, side 4	0.955	0.954	0.918	0.974	0.959/ 0.917

Table 6.4: Estimated and calculated channel correlation coefficients of experiment 1

	$E\{\hat{\rho}_{12}\}$	$E\{\hat{\rho}_{23}\}$	$E\{\hat{\rho}_{13}\}$	$E\{\rho_l\}$	$E\{\rho_s\}$
$\theta = 35°$, side 1	0.962	0.961	0.884	0.993	0.969/ 0.900
$\theta = 35°$, side 2	0.961	0.960	0.904	0.985	0.967/ 0.917
$\theta = 35°$, side 3	0.966	0.965	0.899	0.992	0.969/ 0.905
$\theta = 35°$, side 4	0.969	0.968	0.895	0.997	0.975/ 0.912
$\theta = 15°$, side 1	0.945	0.944	0.856	0.984	0.952/ 0.866
$\theta = 15°$, side 2	0.971	0.971	0.919	0.9993	0.971/ 0.911
$\theta = 15°$, side 3	0.959	0.958	0.902	0.984	0.961/ 0.899
$\theta = 15°$, side 4	0.970	0.970	0.905	0.997	0.974/ 0.910

Table 6.5: Estimated and calculated channel correlation coefficients of experiment 2

	$E\{\hat{\rho}_{12}\}$	$E\{\hat{\rho}_{23}\}$	$E\{\hat{\rho}_{13}\}$	$E\{\rho_l\}$	$E\{\rho_s\}$
$\theta = 35°$, side 1	0.951	0.950	0.828	0.998	0.952/ 0.826
$\theta = 35°$, side 2	0.950	0.949	0.822	0.999	0.956/ 0.837
$\theta = 35°$, side 3	0.943	0.941	0.798	0.999	0.950/ 0.818
$\theta = 35°$, side 4	0.953	0.952	0.836	0.998	0.954/ 0.834
$\theta = 15°$, side 1	0.952	0.951	0.836	0.998	0.953/ 0.832
$\theta = 15°$, side 2	0.943	0.941	0.813	0.996	0.950/ 0.827
$\theta = 15°$, side 3	0.936	0.934	0.785	0.998	0.948/ 0.815
$\theta = 15°$, side 4	0.951	0.949	0.834	0.997	0.953/ 0.832

Table 6.6: Estimated and calculated channel correlation coefficients of experiment 3

data from equation (5.27). A match between the actual channel correlations and the theoretical channel correlation of sea data can however be observed, where also here channels 1 and 3 are significantly less correlated than the other ones.
In figures 6.28 and 6.29 channel correlation coefficients are visualized of data sets, which were collected during experiments 2 and 1, to show how sea data channel correlation changes for different sea conditions. In figure 6.28 the data set of experiment 2 is pre-

sented, which shows a smaller difference between the estimated correlation $\hat{\rho}_{13}$ and the other correlations in reference to the data sets of experiment 3. This is due to a smaller sea scatterer velocity variance, which was present during experiment 2 as compared to experiment 3. Figure 6.29 shows an even smaller discrepancy between the different channel correlations. In this figure the correlation is evaluated from a data set of experiment 1, where the radial sea scatterer velocity variance is the smallest one of all three sea experiments. Also the deviation between estimated coefficients and the calculated one for land data is not significant, indicating a small influence of the movement of sea scatterers on the channel decorrelation. A smaller sea scatterer velocity variance is observed for experiments 2 and 1 due to a smaller sea state, which was present during these experiments. The radial sea scatterer velocity variance is proportional to the orbital velocity variance of the sea surface and this variance decreases for smaller sea states, as described in chapter 3.1.
Figures 6.28 and 6.29 show that for smaller sea states the channel decorrelation due to noise rises. This is due to the decrease of the radar cross section of sea echoes for smaller sea states, as observed in chapter 4.3.
Tables 6.4 - 6.6 summarize the correlation coefficients between the three channels of all available data sets. These coefficients are estimated within the azimuth angle intervals described in section 6.4 and calculated with equations (5.27) and (5.37). These tables show three properties. First, they illustrate that channel correlation of sea data is highly dependent on the sea state. The difference between the correlation of channels 1 and 3 and the other channel correlations changes significantly for different experiments. Also the discrepancy between the actual channel decorrelation and the calculated channel decorrelation due to noise varies for different experiments. Both variations are due to different sea scatterer velocity variances during different experiments, hence the impact of the movement of the scatterers is different for all three experiments. Secondly, tables 6.4 - 6.6 demonstrate same properties for both grazing angles. Thirdly, these tables validate the derived model to calculate the channel correlation of sea data in equation (5.37), indicating that channel decorrelation due to the movement of the sea surface can be reproduced by the proposed model. Some deviations are evident for experiment 3 at sides, where significant amounts of fast scatterers are present. This is because fast scatterers are not considered in the derived model. Another possible deviation source is if the sea scatterer velocity has a different distribution than the Gaussian one. Further, the channels can decorrelate due to any other non-ideal conditions, which are not considered by the presented model.

6.6 Real and Simulated Data with Fast Scatterers

To validate the impact of fast scatterers on multichannel properties of sea data, simulated and real data sets with slow and fast scatterers are evaluated. Such simulations are performed as described in section 6.1. Here, however, a space-time clutter signal, which

consists of slow and fast scatterers, is used

$$\tilde{\mathbf{c}} = \int_{\Omega} A(u)\tilde{\mathbf{s}}(u, V_s(u))\, du + B \int_{\Omega} A_f(u)\tilde{\mathbf{s}}(u, V_f(u))\, du. \tag{6.10}$$

For the described simulations, the mean of the fast scatterer velocity μ_f, the mean of the Bernoulli variable μ_B, the fast scatterer velocity variance σ_f^2 and the reflectivity variance σ_{cf}^2 are chosen to match real data.
In figure 6.30 beamformed clutter power of the same CPI as in figure 5.9 is presented, and the power of a simulated data set with corresponding radar and sea parameters is shown in figure 6.31. Both figures show several scatterers with a high negative radial velocity.
In figures 6.32 and 6.33 the eigenvalue distributions of these CPIs are visualized. The second eigenvalue around the Doppler centroid is also significantly higher than for land data, due to the motion of the sea scatterers. Additionally, however, the centroid of the second eigenvalue distribution is different from the one of the first eigenvalue. For simulated and real data, the second eigenvalue distribution centroid is at 46 Hz. This is expected due to the derivations which are performed in chapter 5.5, where an asymmetric contribution to the second eigenvalue distribution in dependence of the frequency is calculated, if fast scatterers are present. The dotted black line in figure 6.33 indicates the calculated distribution of the second eigenvalue from equation (5.45). For this calculation, the clutter power of slow and fast scatterers of the performed simulation are used. The calculated eigenvalue distribution is also centered around 46 Hz and agrees quite well with the simulated one. Small deviations are present due to several approximations, which are applied to calculate the second eigenvalue of the slow plus fast scatterer spectral density matrix. Figures 6.32 and 6.33 show a higher third eigenvalue distribution, which is because of the presence of fast scatterer clutter power in the third subspace dimension. The power of the third eigenvalue distribution in figure 6.32 is lower than the one in figure 5.9, due to a discrepancy between estimated and calculated eigenvectors.
Figure 6.34 and 6.35 show the phase of the first eigenvector of real and simulated data. In figure 6.34 the black line indicates the phase of the theoretical DOA vector. It is obvious that the phase of the DOA vector does not correspond to the one of the first eigenvector at positive frequencies. As predicted in chapter 5.5, the first eigenvector changes asymmetrically due to the contribution of fast scatterers and is therefore not equal to the DOA vector any more. In figure 6.35 the black line indicates the phase of the first eigenvector, calculated from equation (5.46). This figure shows a good agreement between the calculated and simulated phase of the first eigenvector. This validates the derivations performed in chapter 5.5. Small deviations exist due to the used approximations.
The space-time filter gain of real and simulated sea data sets with fast scatterers are illustrated in figures 6.36 and 6.37. Both figures show a broader filter notch at positive Doppler frequencies than at negative ones. Therefore, at positive Doppler frequencies more look directions are attenuated by the space-time filter. Due to a changing centroid of the second eigenvalue distribution, an asymmetric space-time filter is predicted is chapter 5.5.

In figure 6.38 beamformed clutter power of a CPI of experiment 3 is presented, where the sea surface was moving in the down swell direction. This CPI is processed in the same manner as the CPI in figure 6.30. Figure 6.39 displays beamformed clutter power of a simulated CPI with matching radar and sea parameters. In figures 6.38 and 6.39 several scatterers at positive radial velocities are visible.
Figure 6.40 shows eigenvalue distributions of the described real data set and figure 6.41 of the simulated one. In both figures the centroid of the second eigenvalue distribution is shifted to -31 Hz. Figure 6.41 also visualizes the calculated distribution of the second eigenvalue for different frequencies with equation (5.45) for the corresponding radar and sea parameters. Also for the down swell condition this calculation matches the simulation.
In figure 6.42 the phase of the estimated first eigenvector of the real data is plotted. Additionally, the dotted black line indicates the phase of the theoretical DOA vector. Figure 6.42 shows that at negative Doppler frequencies the theoretical DOA vector does not match the actual one. In figure 6.43 the phase of the first eigenvector of the simulated data set is visualized. Here the dotted black line indicates the phase of the theoretically calculated first eigenvector from equation (5.46). This figure shows that this measure can be calculated from this equation for different frequencies, also for the up swell condition. Figures 6.44 and 6.45 illustrate the space-time filter gain of simulated and real sea data with many fast scatterers at negative Doppler frequencies. Here asymmetrical broadness of filter notches is evident, as well, where for these data sets a detection is more difficult at negative Doppler frequencies.

The comparison of simulated and real multichannel properties, which are presented in figures 6.32-6.45, illustrates a good agreement between both data sets for the up and down swell direction. All multichannel characteristics of real data are reproduced by the performed simulations. This shows that the impact of fast scatterers on multichannel characteristics can be simulated with the proposed model.

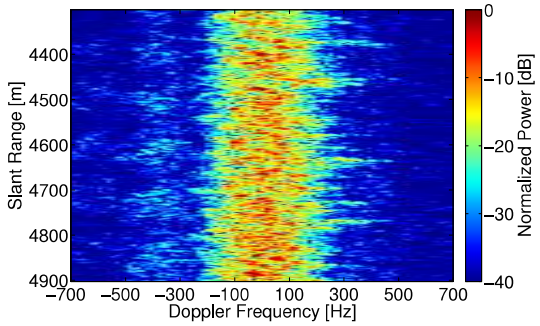

Figure 6.30: Beamformed power. Real data, exp. 3, up swell condition.

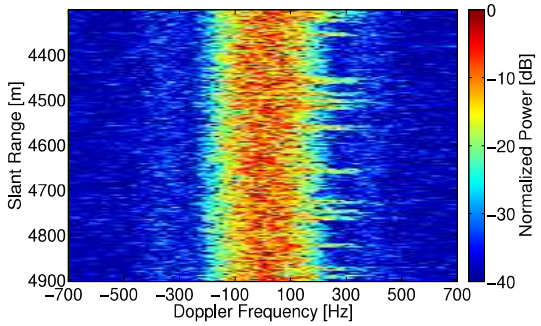

Figure 6.31: Beamformed power. Simulated data, matching parameters.

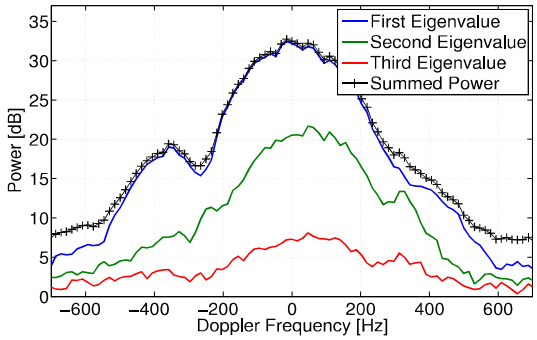

Figure 6.32: Eigenvalue distributions. Real data, exp. 3, up swell condition.

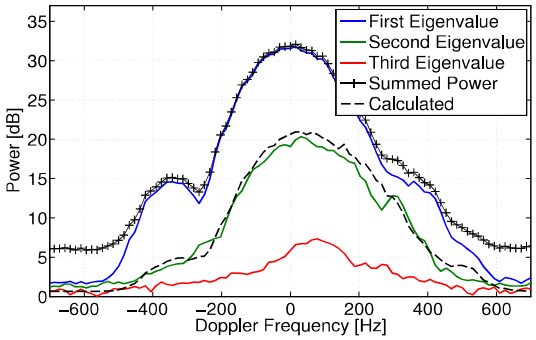

Figure 6.33: Eigenvalue distributions. Simulated data, matching parameters.

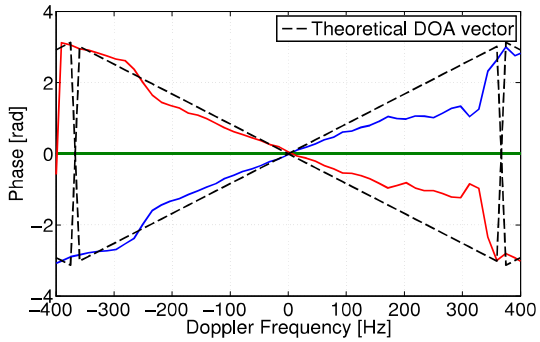

Figure 6.34: Phase of first eigenvector. Real data, exp. 3, up swell condition.

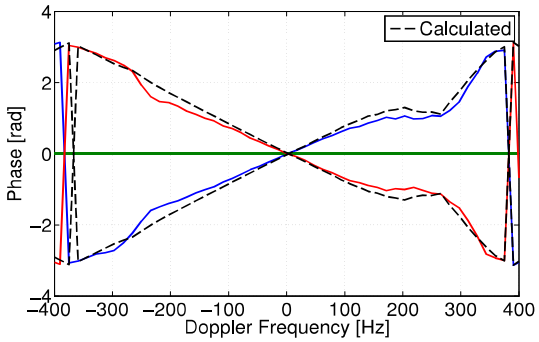

Figure 6.35: Phase of first eigenvector. Simulated data, matching parameters.

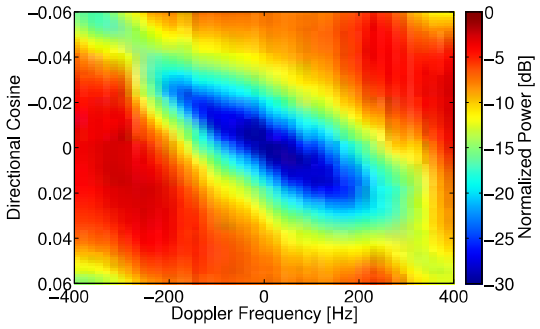

Figure 6.36: Space-time filter gain. Real data, exp. 3, up swell condition.

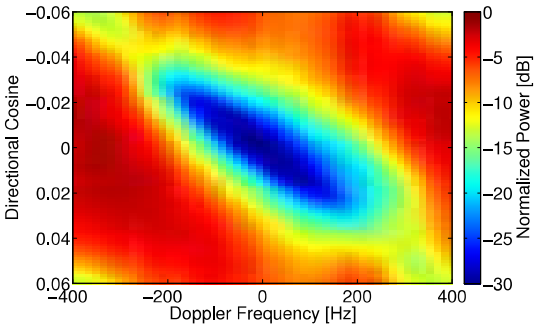

Figure 6.37: Space-time filter gain. Simulated data, matching parameters.

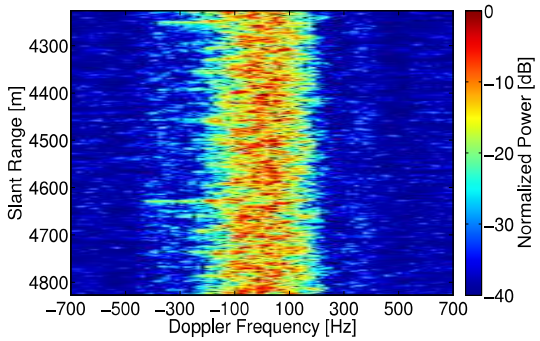

Figure 6.38: Beamformed power. Real data, exp. 3, down swell condition.

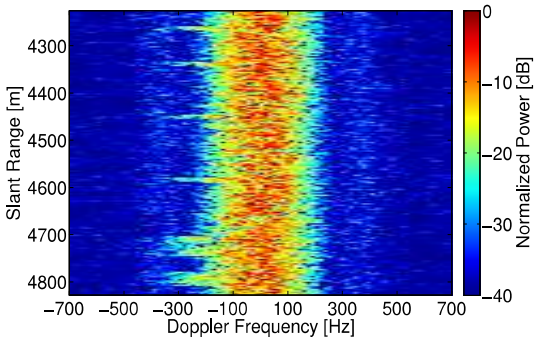

Figure 6.39: Beamformed power. Simulated data, matching parameters.

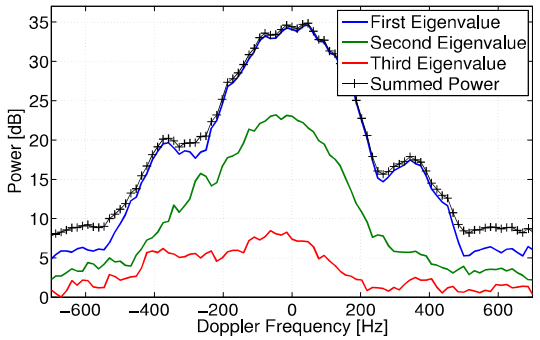

Figure 6.40: Eigenvalue distributions. Real data, exp. 3, down swell condition.

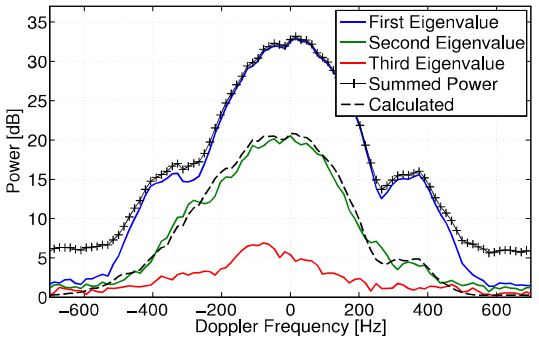

Figure 6.41: Eigenvalue distributions. Simulated data, matching parameters.

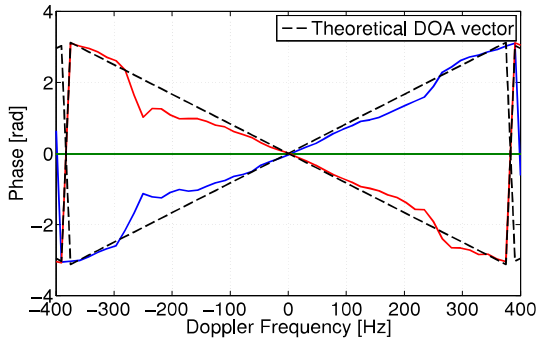

Figure 6.42: Phase of first eigenvector. Real data, exp. 3, down swell condition.

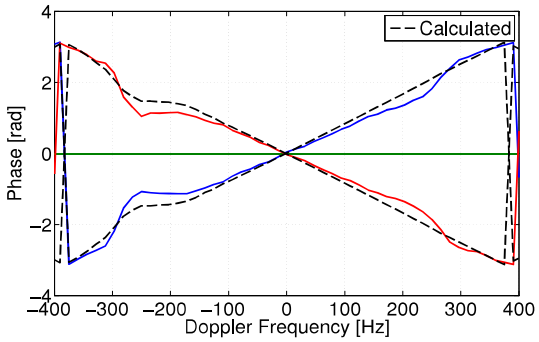

Figure 6.43: Phase of first eigenvector. Simulated data, matching parameters.

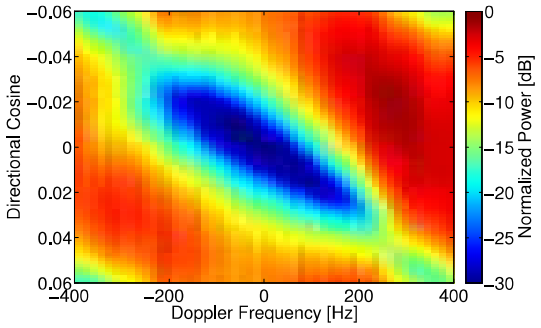

Figure 6.44: Space-time filter gain. Real data, exp. 3, down swell condition.

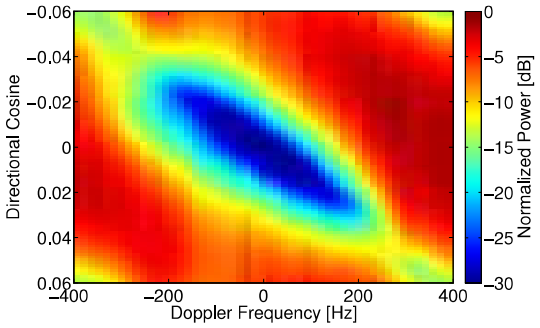

Figure 6.45: Space-time filter gain. Simulated data, matching parameters.

Chapter 7

Experiments with a Small Cooperative Boat

In the context of this thesis, experiments with the PAMIR system and a small cooperative boat were performed. The goal of these experiments, which are described in section 7.1, is to evaluate if STAP is needed for maritime radar systems. For this analysis, the target position is calculated inside the acquired data in section 7.2 and the SCNR is determined in section 7.3. Section 7.4 demonstrates the detection performance of the cooperative target for different processing methods.

7.1 Experiments

Figure 7.1: Cooperative boat, 7.5 m length $\times$ 2.5 m width

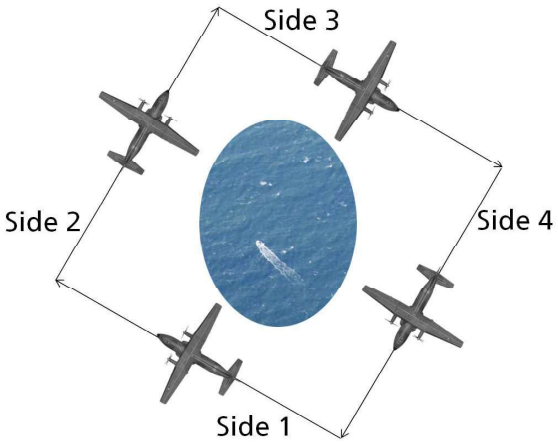

Figure 7.2: Flight path with a picture of cooperative target

PRF	2000 Hz
Range resolution	3.75 m
Nearest center slant range	5600 m
Platform velocity	100 m/s
Depression angle	35°
Slant swath	4500 m

Table 7.1: Radar parameters

Significant wave height	1.9 m - 2 m
Wind velocity	9 m/s - 11 m/s
Wind direction (ENU)	170° - 200°
Swell direction (ENU)	160° - 180°
Sea state	4

Table 7.2: Weather data

The experiments, which are evaluated in this chapter, were performed in the same manner as the sea experiments described in chapter 4.2. Here, however, also a cooperative target was located inside the scene. This target is a small boat with dimensions 7.5 m length $\times$ 2.5 m width, as shown in figure 7.1. During these experiments, a GPS system was used to record the position, track and velocity of the boat, where the boat was moving with its maximum possible velocity of 5 m/s - 6 m/s. In figure 7.2 the flight path is illustrated with a picture of the cooperative target. This picture was taken with a camera, which is integrated inside the PAMIR system, during the performed experiments. The track of the plane was rotated by 30° from the north, east, south and west direction. The radar parameters are summarized in table 7.1.

Several weather stations located near Helgoland were used to collect weather data. These recordings are summarized in table 7.2 and show quite rough sea conditions. The swell and wind direction angles are transformed into an ENU coordinate system and the sea state is identified on the Douglas scale.

7.2 Target Position in acquired Data

To evaluate how well the cooperative boat can be detected with different processing techniques, the position of this boat inside the acquired data has to be known. The longitude, latitude and velocity of the boat were recorded with a GPS receiver. These measures are also known from the platform due to the IMU and DGPS systems which are integrated inside the PAMIR system. The longitude and latitude of the center position were defined a priori. The roll, pitch and yaw angles of the platform were taken into account by the steering of the phased array antenna, hence the center position is always the specified longitude and latitude.
To calculate the position of the target, its longitude and latitude have to be evaluated in terms of an earth-based local coordinate system. The longitude and latitude, which are given in the World Geodetic System 1984 (WGS84), are first transformed to an earth-centered earth-fixed (ECEF) coordinate system. These coordinates are then converted to a local east-north-up (ENU) Cartesian coordinate system. To transform from the ECEF coordinate system to an ENU coordinate system, a reference position has to be defined. Here the platform position is chosen as the reference position, because all location information collected by the PAMIR system is in reference to the platform, hence the platform coordinates are always $\mathbf{x}_p = (0,0,0)^T$. The described geometry is visualized in figure 7.3. Here the position of the boat is described by the position vector $\mathbf{x}_t$ and the center position coordinates are denoted by $\mathbf{x}_c$. The LOS vector to the center position is equal to $\mathbf{u}_c = \frac{\mathbf{x}_c}{||\mathbf{x}_c||}$, and the one to the target position is described by $\mathbf{u}_t = \frac{\mathbf{x}_t}{||\mathbf{x}_t||}$. Note that for this geometry the platform is not assumed to move along the x-axis. The platform velocity vector can be calculated from $\mathbf{v}_p = (v_{ph}\cos(\varphi_p), v_{ph}\sin(\varphi_p), v_{pv})^T$, where the horizontal and vertical platform velocities v_{ph} and v_{pv} and the track of the platform φ_p were recorded by the PAMIR system. The velocity vector $\mathbf{v}_s$ is due to the mean sea scatterer velocity at the center position.
With the target position vector, the target slant range can be calculated as

$$r_t = \sqrt{(x_t - x_p)^2 + (y_t - y_p)^2 + (z_t - z_p)^2} \tag{7.1}$$

and the Doppler shift of the target is equal to

$$\mathcal{F}(\mathbf{u}_t, \mathbf{v}_t) = -\frac{2}{\lambda_r}\mathbf{u}_t^H(\mathbf{v}_t - \mathbf{v}_p). \tag{7.2}$$

Here $\mathbf{v}_t$ is the target velocity vector, which can be calculated as

$$\mathbf{v}_t = v_t\left(\cos(\varphi_t), \sin(\varphi_t), 0\right)^T, \tag{7.3}$$

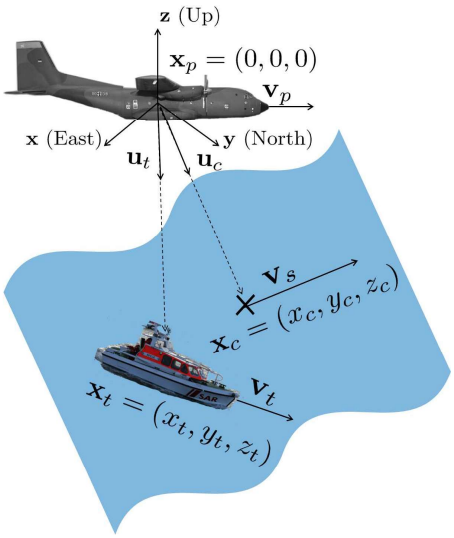

Figure 7.3: Geometry of observed scene

where φ_t is the track of the target and v_t the magnitude of the target velocity. Both values were collected with the GPS system. With the target Doppler shift, the radial velocity of the target relative to the center position can be calculated as

$$v_r = -\frac{\lambda_r}{2} \left(\mathcal{F}(\mathbf{u}_t, \mathbf{v}_t) - \mathcal{F}(\mathbf{u}_c, \mathbf{v}_s) \right), \tag{7.4}$$

where $\mathcal{F}(\mathbf{u}_c, \mathbf{v}_s)$ is the Doppler shift at the center position, whose estimation is described in chapter 4.3. The described calculation is demonstrated for all four sides in figure 7.4 in dependence of the azimuth angle in ENU coordinates, which is defined in equation (4.1). Figure 7.4 shows that the radial target velocity varies quite strongly for sides 1 and 3. For some angles the target is very fast and for some azimuth angles the radial velocity is almost zero. For sides 2 and 4 the variation of the target radial velocity is significantly smaller. During the data acquisition at side 2, the target velocity varied around 1.5 m/s - 4 m/s and while the plane was flying on side 4, the target moved with a radial velocity between 1 m/s - 1.5 m/s. As was described in chapter 2.2, it is important to know if the target is positioned inside or outside of the clutter band to analyze the different clutter suppression filters. For the PAMIR system, the theoretical clutter band is distributed between the velocity interval of $\pm$ 2 m/s for the platform velocity of 100 m/s. Due to the movement of the sea scatterers, the actual clutter band is however broader. To be positioned outside of the sea clutter band, the relative radial velocity of the target therefore has to be faster than for a land clutter band.
Figure 7.5 shows beamformed data in the range Doppler domain for one CPI, which was acquired during side 4. The CPI consists of 128 pulses with a PRF of 2000 Hz. The white circle in this figure indicates the expected position of the boat, calculated from equations (7.1) and (7.2). The target is however masked by the strong clutter. The

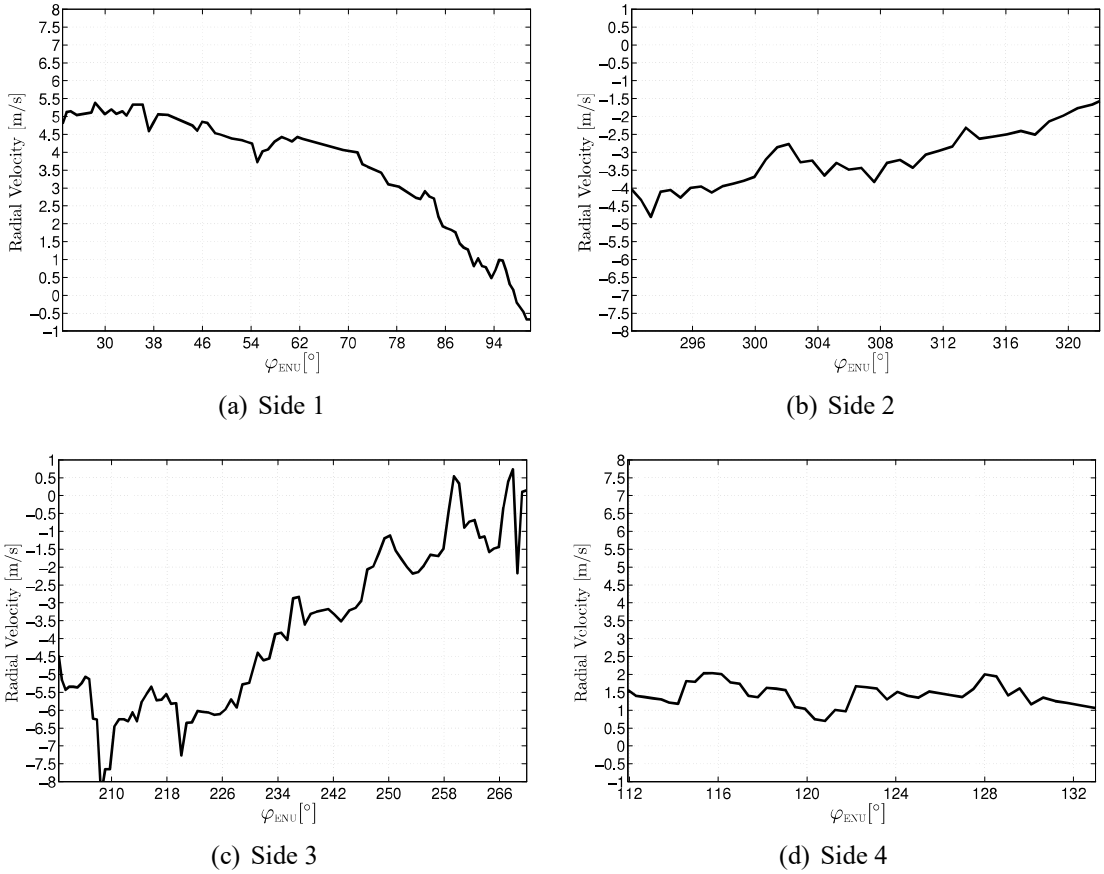

(a) Side 1 (b) Side 2

(c) Side 3 (d) Side 4

Figure 7.4: Relative radial velocity of cooperative target calculated from GPS data and clutter Doppler centroid

remaining uncertainty in range is due to the uncertainty of the GPS localization, which was 10 m during the data collection. This affects also the accuracy of the Doppler shift, but its uncertainty is additionally determined by the acceleration and the vertical velocity of the target, which were not known exactly during these experiments. To visualize the Doppler shift due to the movement of the scatterers, only the Doppler shift due to the platform velocity is compensated in figure 7.5. The remaining Doppler shift after this compensation is at 31 Hz, which corresponds to a mean radial velocity of the sea scatterers of -0.5 m/s.

7.3 SCNR before and after Clutter Suppression

A crucial parameter for target detection is the SCNR. On one hand, this measure is presented in this section without any processing, and on the other hand the SCNR is evaluated after clutter suppression with different filters. In figure 7.6 the SCNR before clutter suppression is plotted for data sets collected from the four different sides in dependency

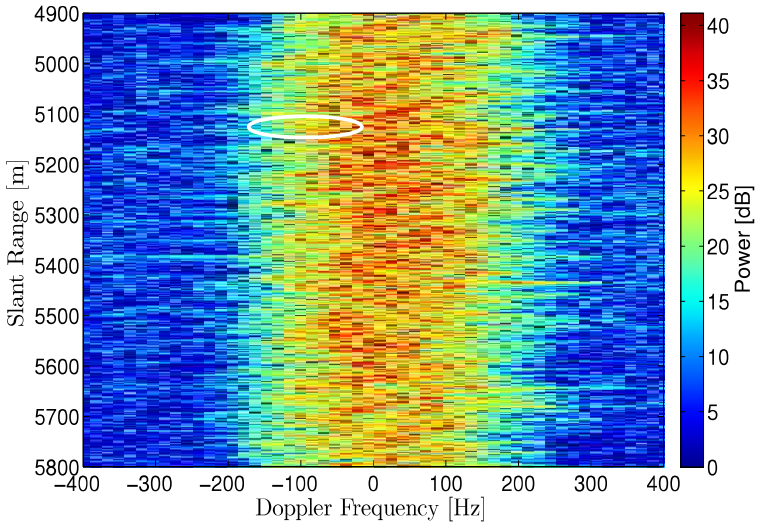

Figure 7.5: Beamformed data of one CPI. The circle indicates the position of the target, calculated from GPS data.

of the azimuth angle. The signal of the target is estimated from the maximum power inside the circle. The clutter and noise power is estimated by calculating the mean power inside the main beam (3 dB), but outside of the circle. For low signal powers, rather strong clutter returns inside the circle are mistaken to be the target, hence this estimation has to be considered as being the upper bound of the real SCNR. Figure 7.6 reveals quite strong variations of the SCNR before clutter suppression, which is due to different positions of the target inside the antenna beam and due to different target echoes from different aspect angles. To consider the variation of the SCNR due to the antenna beam, a normalized two-way antenna pattern is added to the real SCNR. The corrected SCNR is denoted by the blue dashed line in figure 7.6. Here only the azimuth antenna pattern is considered due to the narrower beamwidth. The position of the target inside the antenna beam is derived by calculating the difference between the cone angle of the center position and the cone angle of the target in the platform coordinate system.
The boat was not always inside the antenna beam, due to the stormy weather conditions and the small azimuth swath. Here data is considered, where the boat was inside the one-fourth power beamwidth (6 dB). During the data acquisition of side 2, the boat was not positioned in the center of the elevation pattern, therefore its SCNR is significantly lower than the ones of the other sides.
To compare the performance between multichannel processing and single channel processing with adaptive matched filters, a TAP filter and two different STAP filters are applied to the data to suppress the clutter. For multichannel processing the two most common STAP methods are chosen: pre-Doppler and post-Doppler STAP. For pre-Doppler STAP the sub-CPI method is applied and for post-Doppler STAP the multi-bin method is used. The sub-CPI method is described in detail in [28] and [30] and the multi-bin

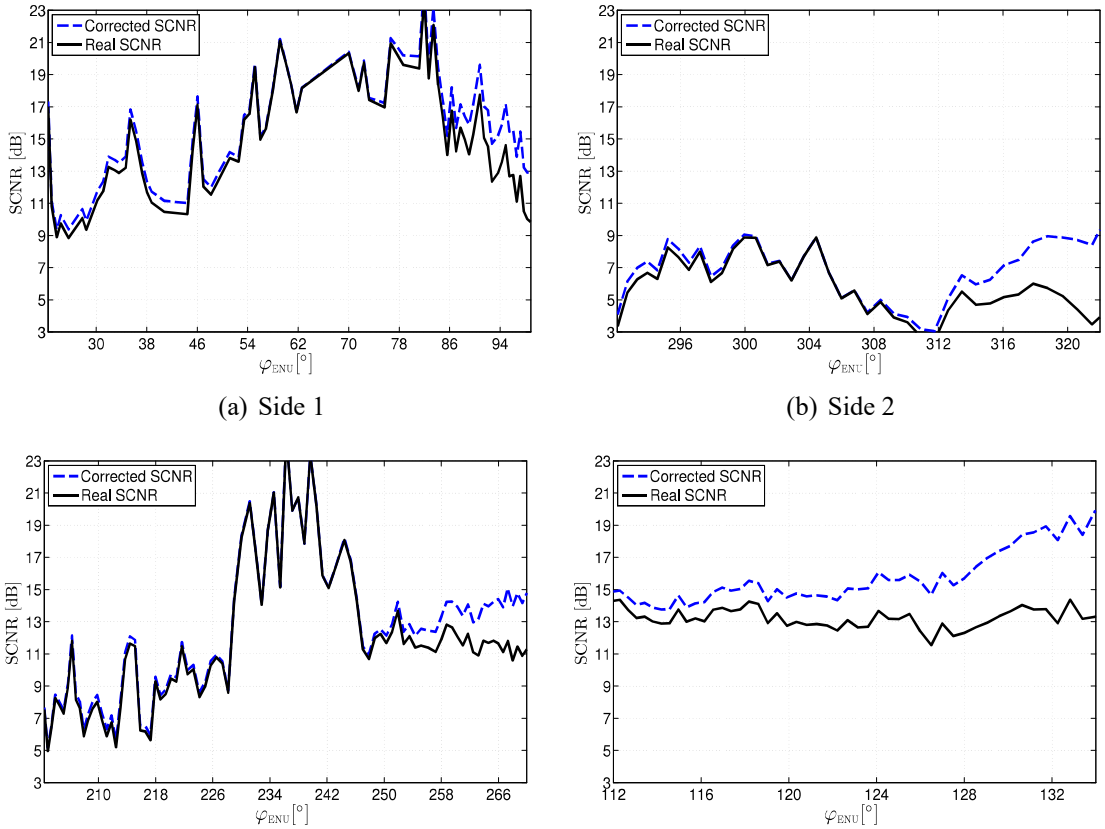

(a) Side 1 (b) Side 2

(c) Side 3 (d) Side 4

Figure 7.6: SCNR before clutter suppression. Estimated SCNR (black line) and SCNR with corrected antenna pattern (dashed blue line).

method in [30] and [88]. The main steps are visualized in figure 7.7, where the multi-bin method is shown on the left side of this figure. Here first a Fourier transform is performed in the slow time domain of one CPI. Then the available channels and a certain amount of Doppler bins, which are adjacent to the cell under test (CUT), are used to form a STAP filter. To estimate the spectral density matrix for this filter, the available range bins are utilized. A STAP filter is estimated and applied to each CUT. The sub-CPI method is visualized on the right side of figure 7.7. Here a certain amount of pulses and the available channels are used to form a STAP filter, where the covariance matrix is estimated from the available range samples. The Fourier transform is only performed after applying the STAP filter to each CUT. For the presented evaluation, two adjacent Doppler bins on each side are applied for the multi-bin method and four pulses are used for the sub-CPI method. For TAP also the sub-CPI technique is applied, first, however, the multichannel data is coherently combined to one single channel. For all filters, the spectral density or covariance matrix is estimated for each CUT using 256 range samples for training, with 128 bins being on each side. Four guard cells are used on each side of the CUT

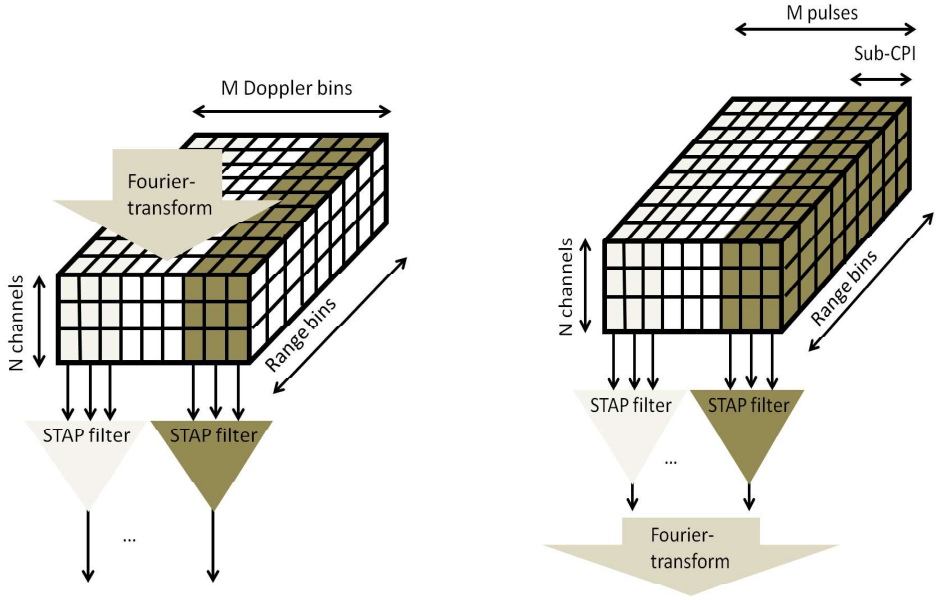

Figure 7.7: Main processing steps of multi-bin post-Doppler STAP (left) and sub-CPI pre-Doppler STAP (right)

to ensure that the target will not eliminate itself. A Hamming window is utilized for the post-Doppler technique, but not for the other ones. The SCNR after clutter suppression is calculated by considering the maximum power inside the circle and dividing it by the clutter plus noise power, which is estimated from all samples outside of the circle. Ideally, the clutter should be completely suppressed by the filter, so that the SCNR is equal to the signal-to-noise-ratio (SNR).
Figure 7.8 shows the SCNR after clutter suppression for the four different sides. The data of side 1 reveals quite high variations of the SCNR before clutter suppression. In figure 7.8(a), however, a high SCNR after all processing methods for angles until $\varphi_{\text{ENU}} = 86°$, with values of 20 dB - 30 dB, is visualized. For these angles, the target echo is outside of the clutter band, hence it is not suppressed by any filter. From $\varphi_{\text{ENU}} = 86°$ till the end of the data set, the relative target velocity is not higher than the maximum velocities of the clutter band, the target echo is therefore positioned inside the clutter band. For these angles the TAP-SCNR is clearly lower than the SCNRs of the STAP filters. For $\varphi_{\text{ENU}} = 98°$ - $101°$, the target velocity varies from -0.5 m/s to 0.5 m/s and the target signal is suppressed by all filters.
The SCNR of side 2 is low for all angles prior to clutter suppression. After applying all processing methods, however, values of 20 dB - 28 dB are observed, where the target power is well outside of the clutter band. This is the case for angles up to $\varphi_{\text{ENU}} = 314°$. At this angle the radial target velocity is at -2.5 m/s, which is theoretically outside of the clutter band, but due to the movement of the sea scatterers and due to fast scatterers, a broader clutter filter is estimated. From this angle the SCNR of all processings drops,

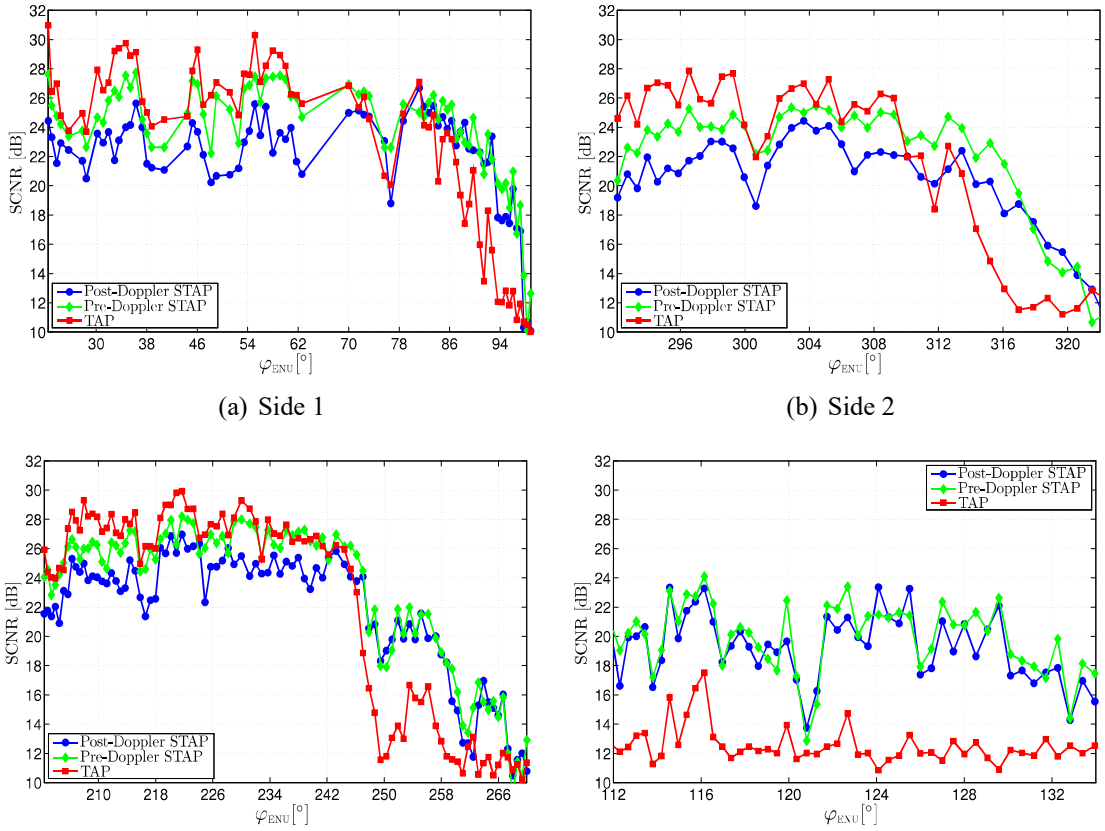

(a) Side 1 (b) Side 2

(c) Side 3 (d) Side 4

Figure 7.8: Estimated SCNR after clutter suppression with two different STAP filters and a TAP filter

where the one after applying TAP is significantly lower than the ones after multichannel processing. At $\varphi_{ENU} = 318°$ the target velocity is -2.1 m/s. From this angle till the end of the data set, the SCNR after clutter suppression is very low for all processing methods, which is also due to a lower SCNR prior to any processing.
During side 3 the target returns vary strongly. A high SCNR after clutter filtering can be observed for all angles, where the target signal does not have to compete with clutter returns. At $\varphi_{ENU} = 247°$ the target echo is positioned inside the clutter band. For this and all following angles, the target signal is suppressed by the TAP filter. From $\varphi_{ENU} = 259°$ the target radial velocity varies around -0.5 m/s to 0.25 m/s. For these velocities the target is also suppressed by the STAP filters.
The target signal, which was received during the experiment at side 4, is quite low, with values around 12 dB - 14 dB. Additionally, the target echo is always positioned inside or at the edge of the clutter band. Hence, the estimated SCNR after single channel processing mostly varies between 12 dB - 14 dB, which indicates a suppression of the target signal with the TAP filter. After multichannel processing, however, the SCNR is 18 dB -

24 dB for most angles, which results in a mean SCNR improvement of 8 dB with STAP compared to TAP for this side.
After suppressing the clutter, the relative radial target velocity is estimated from the acquired data sets. Such an estimation is needed, if targets of opportunity are detected, where no GPS data is available. This velocity is estimated from considering the Doppler frequency with the maximum power inside the circle after clutter suppression. The standard deviations of the difference between the calculated radial target velocity and the estimated one are summarized in table 7.3 for the different filters. The deviations are due to the uncertainties described in section 7.2. Furthermore, for some CPIs the target power is spread over several strong Doppler cells after clutter suppression. For the TAP filter the deviation is higher, due to suppressed target echoes for some angles. Here the radial velocity resolution is 0.25 m/s.

	Post-Doppler STAP	Pre-Doppler STAP	TAP
Side 1	0.50 m/s	0.47 m/s	0.50 m/s
Side 2	0.45 m/s	0.54 m/s	0.61 m/s
Side 3	0.49 m/s	0.48 m/s	0.77 m/s
Side 4	0.53 m/s	0.59 m/s	0.69 m/s

Table 7.3: Standard deviation between estimated and calculated relative radial target velocities after clutter suppression with different filters

7.4 Detection Performance

To evaluate the detection performance of the cooperative target after applying different filters, a suitable threshold has to be estimated. In this analysis, a threshold is set to achieve a probability of false alarm (P_{fa}) of 10^{-4}. This probability is estimated from all available range samples and Doppler bins which are outside of the target circle. Additionally, an area is excluded where a target of opportunity was present during the experiments. This condition will be described later in more detail. Another possibility would be to estimate the threshold in dependency of the Doppler frequency, because the clutter characteristics vary strongly for different Doppler bins, especially if fast scatterers are present. This is not pursued here, because then for some frequencies the threshold would be very high, preventing a detection of the cooperative target.
In figure 7.9 the estimated threshold is visualized for the four different sides in dependency of the azimuth angle. The mean threshold ranges between 14.9 dB - 15.4 dB for side 1, between 15.8 dB - 16.9 dB for side 2, between 14.7 dB - 15.5 dB for side 3 and is equal to 15.7 dB - 16.7 dB for side 4. The thresholds are on average slightly higher for side 2 and 4, because probably the observed azimuth angles are closer to the down or up swell direction. However, also for side 1 a high threshold is estimated between the azimuth angles 86° - 101° and also for side 3 the threshold is high between 202° -

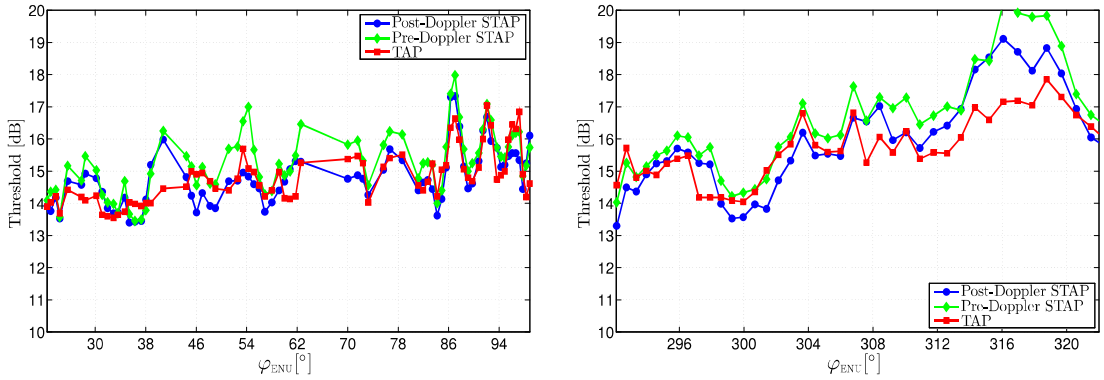

(a) Side 1 (b) Side 2

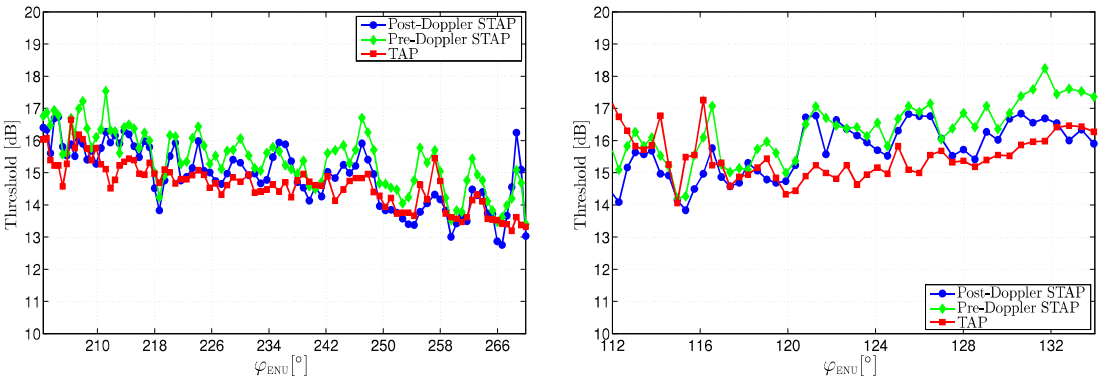

(c) Side 3 (d) Side 4

Figure 7.9: Estimated threshold for $P_{fa} = 10^{-4}$ after clutter suppression with different filters

218°. This is due to some fast scatterers, which are present in these data sets. To analyze why the fast scatterers occur in these angle intervals, more precise weather data would be needed. Figure 7.9 shows that a similar threshold is estimated for the three different processing methods. The threshold after applying the TAP filter is however slightly lower, because fast scatterers are often better suppressed with this filter. Fast scatterers are distributed over all subspace dimensions of the clutter plus noise spectral density matrix, as described in chapter 5.5. This makes it difficult for STAP filters to completely suppress this clutter type. The TAP filter, however, only estimates the present power for each Doppler frequency. If fast scatterers are present at many range bins but one Doppler frequency, they are eliminated with TAP.
The detection performance is evaluated by comparing the remaining power after clutter suppression to the estimated threshold for each CPI. If the power of more than one cell inside the target circle exceeds the threshold, then the target is considered to be detected for the according CPI. The detection performance is visualized for the four different sides for different azimuth angles in figures 7.10 - 7.12. In figure 7.10 the detection perfor-

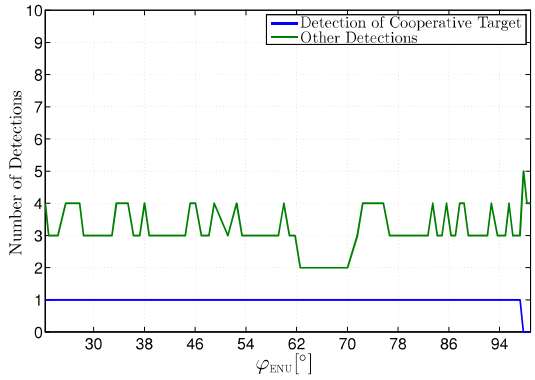

(a) Side 1

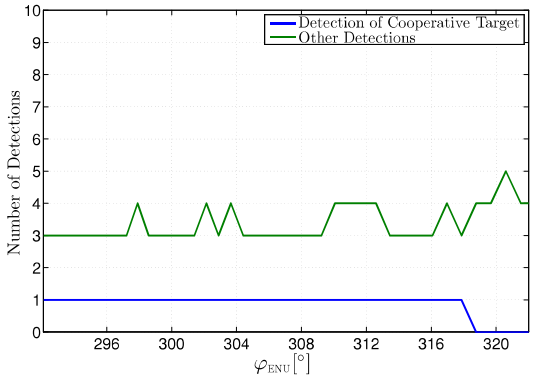

(b) Side 2

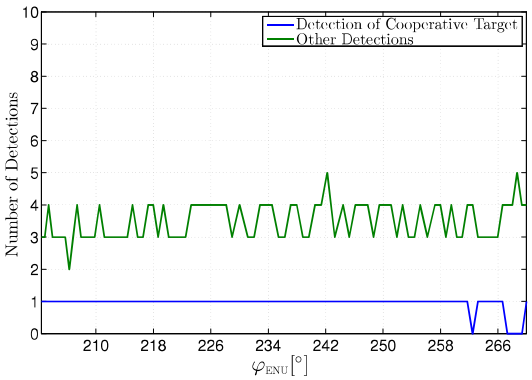

(c) Side 3

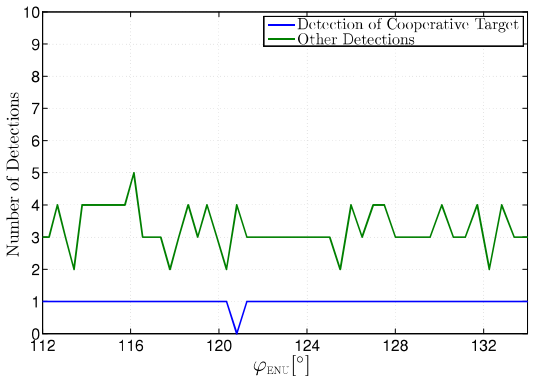

(d) Side 4

Figure 7.10: Number of detections with $P_{fa} = 10^{-4}$ and post-Doppler STAP

mance after applying the post-Doppler STAP filter is demonstrated, figure 7.11 shows the performance after pre-Doppler STAP and figure 7.12 illustrates how well the target is detected with the TAP filter. The blue line in these figures possesses the value 1 if the target is detected at the observed azimuth angle and 0 if it is not. For a better overview, the median between a certain azimuth interval is visualized.
At side 1 the target is reliably detected with TAP until the angle of 92°, which is visualized in figure 7.12(a). At this side the SCNR before clutter suppression is quite high. Even though the target is already inside the clutter band at 86°, it is not suppressed with TAP due to its high signal. With multichannel processing the target is reliably detected until the angle of 98°, as shown in figures 7.10(a) and 7.11(a). During side 2 the SCNR before clutter suppression is very low, because the target is at the edge of the elevation beamwidth. The target is therefore already suppressed by the TAP filter at 314°, where its radial velocity is -2.6 m/s, which is outside of the clutter band. With STAP the target power is suppressed from 316° with pre-Doppler processing and from 318° with post-Doppler STAP, which both correspond to a radial target velocity of -2.5 m/s. These detection performances are shown in figures 7.10(b), 7.11(b) and 7.12(b). Figure 7.12(c)

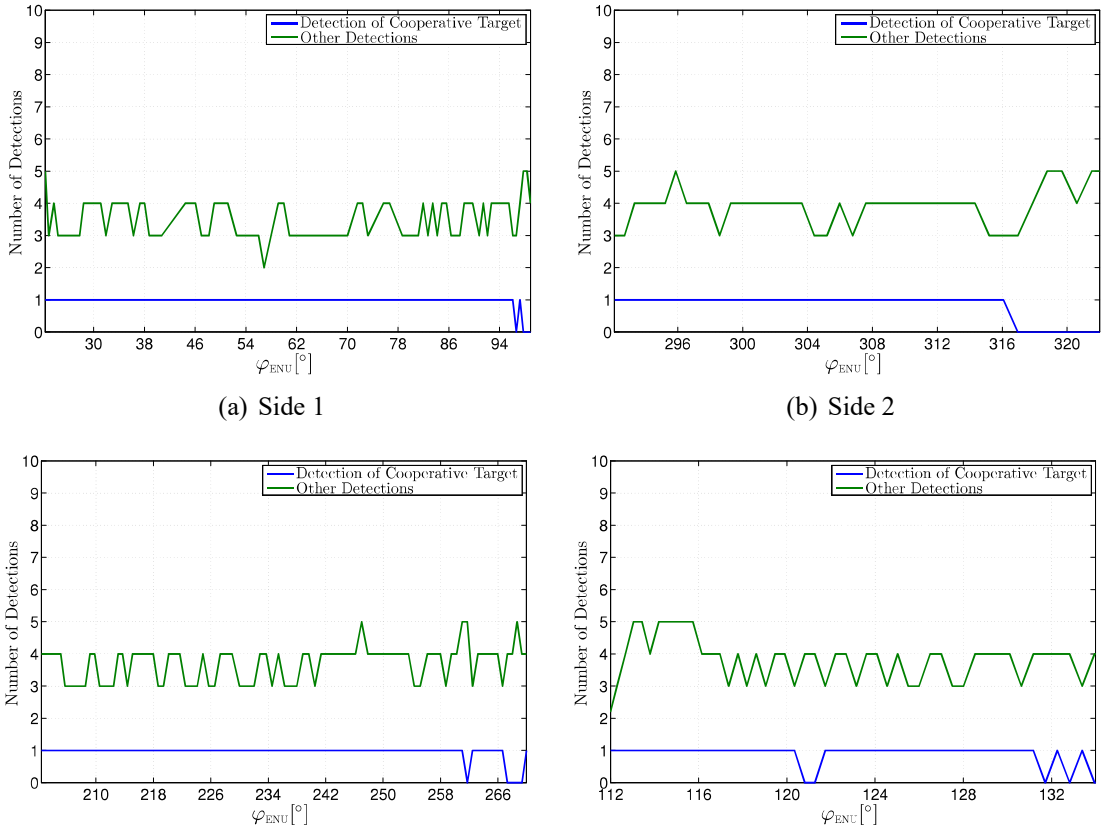

(a) Side 1 (b) Side 2

(c) Side 3 (d) Side 4

Figure 7.11: Number of detections with $P_{fa} = 10^{-4}$ and pre-Doppler STAP

shows detections during side 3 with single channel processing, where the target is identified between 202° - 247°. The target radial velocity range in this angle interval is -8 m/s to -2 m/s. With multichannel processing the target is detected up to a radial velocity of -0.3 m/s. During side 4 the target radial velocity varies between 1 m/s - 1.5 m/s, which is inside the clutter band. At this side the cooperative boat is almost never detected with single channel processing.
The described condition is demonstrated in figure 7.13, where the same CPI as in figure 7.5, is shown. Here the target and clutter power are visualized before and after clutter suppression, where only the slant ranges and Doppler frequencies around the expected target position are presented. In figure 7.13(a) the clutter and target power before clutter suppression are visualized. The target is masked by the clutter and can therefore not be detected. Figure 7.13(b) presents the CPI after applying a TAP filter. This figure shows that the clutter is suppressed quite well with this filter, but also the target is suppressed, preventing a detection. In figures 7.13(c) and 7.13(d) the clutter and target power are demonstrated after applying the two different STAP filters. With multichannel processing the clutter is suppressed, but the target is still well visible. With these processing

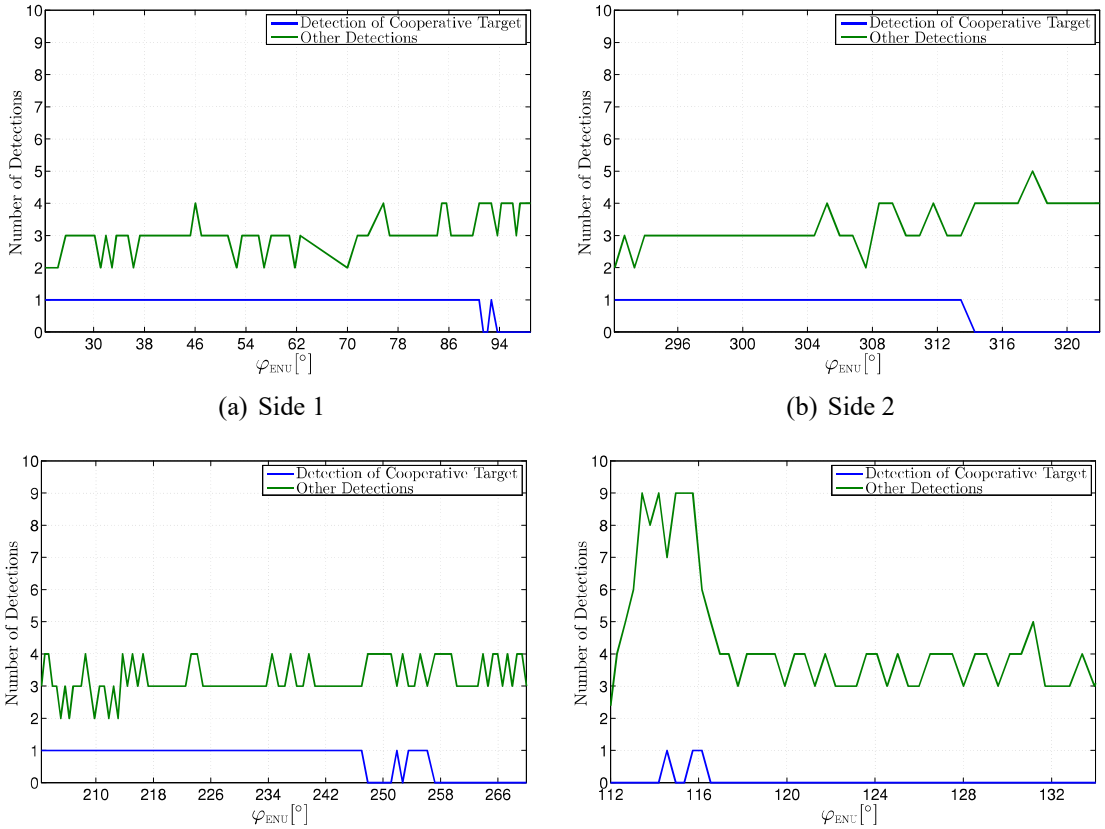

(a) Side 1 (b) Side 2

(c) Side 3 (d) Side 4

Figure 7.12: Number of detections with $P_{fa} = 10^{-4}$ and TAP

methods a detection is possible.
Table 7.4 demonstrates the probability of detection of the four sides and the three filters of all available CPIs. This table shows a worse detection performance with single channel processing. Especially during side 4 the probability of detection with TAP is only 9%, while with post-Doppler STAP the probability of detection is 92% and with pre-Doppler STAP 89%. With STAP filters the target is detected for most azimuth angles, which were observed during the data acquisition at side 4.
The green line in figures 7.10 - 7.12 indicates the number of detections outside of the target circle. In these figures an average is presented for each azimuth angle interval. A detection is considered to be valid if the power of at least two adjacent cells exceeds the threshold. All cells which are next to each other are counted as one target. In most cases the detections outside of the target circle correspond to false alarms. To further reduce their number, the range history of the detections should be analyzed. While the target position is assumed to change linearly in dependence of the slant range for different CPIs, scatterers should show a random behavior. An additional approach could also be to compare the power of a detection before and after clutter suppression. These improvement

steps will be considered in the future.
During side 4, between the angles of 112° - 117°, a target of opportunity was present inside the observed scene. This target was at the edge of the elevation and azimuth antenna beamwidth. Nevertheless, a strong signal power is received from this target. In figure 7.14 a picture of this target is shown. This picture was taken with the camera, which is integrated inside the PAMIR system, during the performed experiment. Figure 7.14 shows a big ship, hence the RCS of this target is quite high. Its power is distributed over several cells, therefore a considerable number of detections is present in figures 7.10(d) - 7.12(d) due to this ship.
In figure 7.15 one CPI which includes this target of opportunity is presented. This target is highlighted with a pink circle, whereas the cooperative boat is bordered by a white circle. Note that while for the cooperative target the position is known due to the GPS data, for the target of opportunity such information is not available. Figure 7.15(a) shows power of the clutter and of both targets without any processing. Here again the cooperative boat is masked by the strong clutter power. The target of opportunity is well visible, because it is well outside of the clutter band and due to its strong signal. In figure 7.15(b) the CPI is presented after clutter suppression with TAP. While the target of opportunity is well visible after single channel processing, the cooperative boat is suppressed and cannot be detected. The power of the big ship is visible over several Doppler frequencies, due to high spectral leakage. In figures 7.15(c) and 7.15(d) the clutter and target power after multichannel processing are demonstrated. These figures show that with STAP both targets can be detected. The power of the big ship after STAP filtering is not as high as without any processing, due to a small number of guard cells.

Side	Post-Doppler STAP	Pre-Doppler STAP	TAP
1	94 %	95 %	82 %
2	89 %	86 %	77 %
3	94 %	93 %	74 %
4	92 %	89 %	9 %

Table 7.4: Probability of detection of different sides after clutter suppression with different filters

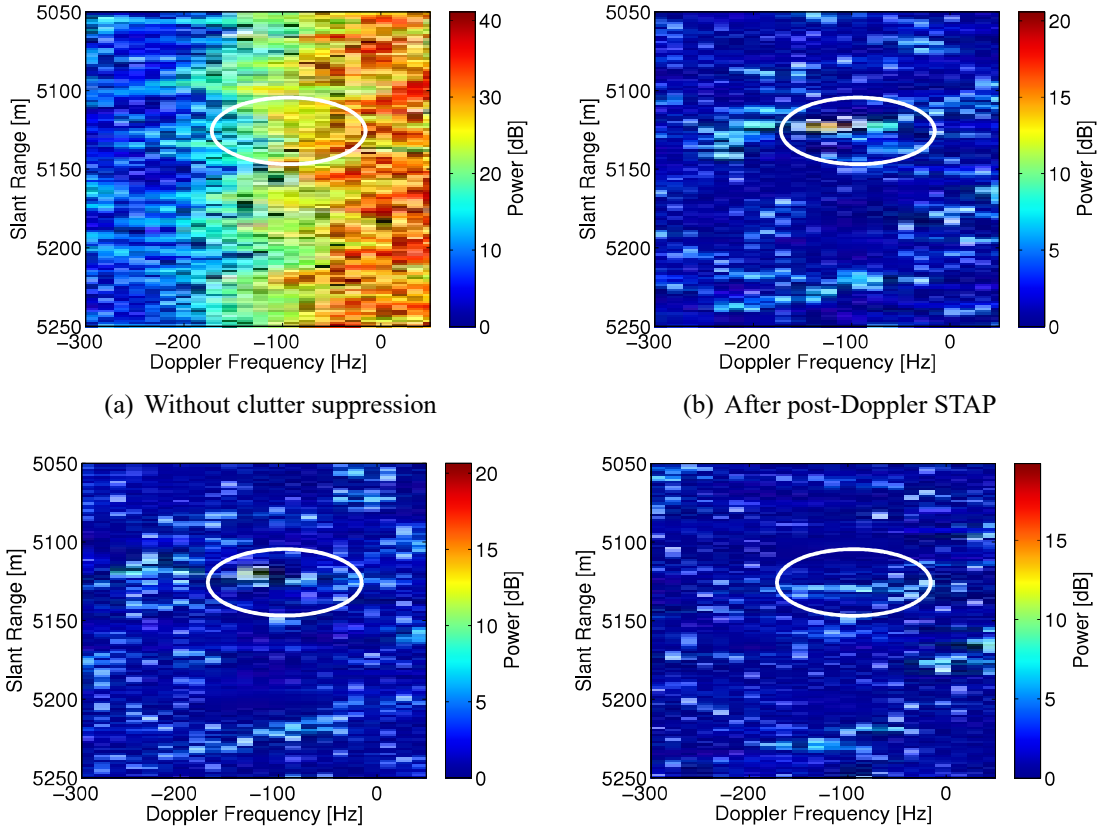

(a) Without clutter suppression

(b) After post-Doppler STAP

(c) After pre-Doppler STAP

(d) After TAP

Figure 7.13: Clutter power and signal of cooperative target with and without clutter suppression

Figure 7.14: Picture of target of opportunity inside the observed scene

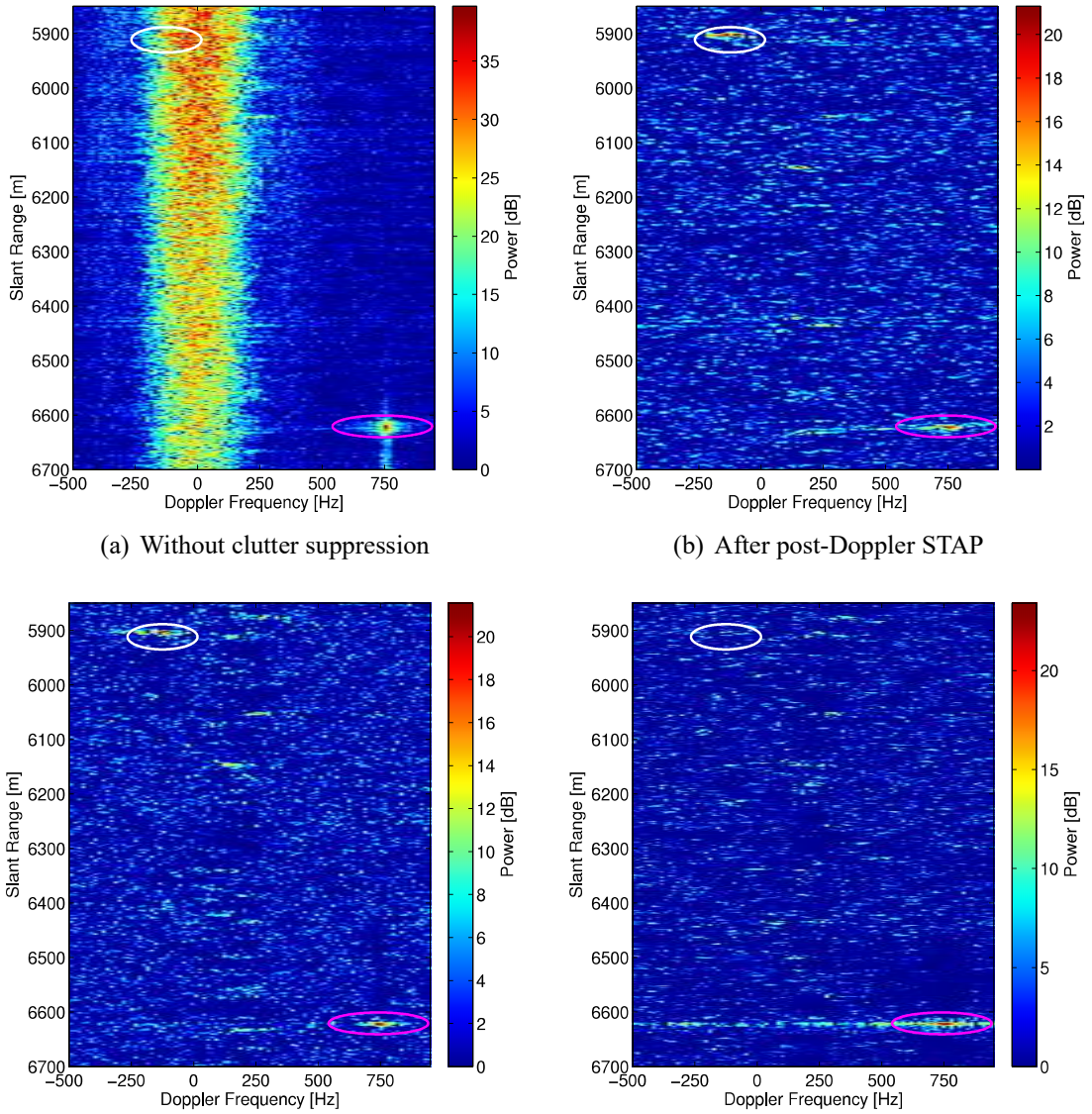

(a) Without clutter suppression

(b) After post-Doppler STAP

(c) After pre-Doppler STAP

(d) After TAP

Figure 7.15: Clutter power, signal of cooperative target and signal of target of opportunity with and without clutter suppression

Chapter 8

Conclusion and Outlook

The main focus of this thesis is to understand the multichannel properties of sea clutter for microwave radars. To achieve this goal, statistical multichannel properties of sea clutter are derived. Then these characteristics are validated with real multichannel sea data and reproduced with a simulation model.
In order to analyze the multichannel properties of sea clutter, first the well-known multichannel characteristics of land clutter are summarized. To point out the differences between land and sea clutter and to gain a deeper understanding of the latter clutter type, the physical origin of sea echoes is described and a brief introduction to oceanography is provided.
To achieve a comprehensive theoretical analysis of multichannel sea clutter, this thesis characterizes the sea clutter spectral density matrix, channel correlation, and space-time filter. It is derived that due to varying velocities of sea scatterers, for sea clutter at least a rank two clutter spectral density matrix has to be considered, whereas for land clutter only a rank one clutter spectral density matrix has to be accounted for.
The calculation of the sea clutter space-time filter demonstrates a broader filter notch than for land clutter, due to different sea clutter multichannel properties. It is shown that the radial sea scatterer velocity variance is crucial in determining the broadness of the space-time filter notch. The physical origin of this measure is investigated and the calculation possibilities are summarized. A further option is to estimate the radial sea scatterer velocity variance from available data. A suitable estimator is proposed in this thesis and its performance is evaluated.
This thesis also demonstrates that fast scatterers, which are echoes due to wave breaking, lead to additional broadening of the filter notch. The properties of this scattering type are summarized and the multichannel sea clutter model is extended to consider fast scatterers.
A model to calculate the channel correlation is derived, which shows that channels of sea clutter are more decorrelated than channels of land clutter due to the movement of sea scatterers. It is illustrated that sea clutter channel correlation is highly dependent on the phase center separation and the radial sea scatterer velocity variance.

To validate the introduced multichannel properties of sea clutter, in the context of this thesis three measurement campaigns were performed with the radar system PAMIR, where multichannel sea data was acquired at different sea states, different swell directions and two different grazing angles. To emphasize the difference between land and sea clutter, also data of a homogeneous land scene was collected. The evaluation of real sea data confirms the theoretical multichannel properties. Furthermore from real data a rank two spectral density matrix is estimated, which is dependent on the sea state. The actual channel correlation changes for different sea states and different phase center separations and matches the calculated one. This thesis demonstrates that for high sea states and in swell direction, fast scatterers are present in real sea data. A modification of the multichannel properties due to these scatterers is evident and agrees with the predicted behavior. Similar characteristics are observed for both grazing angles.
To further confirm the derived multichannel characteristics of sea clutter, simulations are performed with radar and sea parameters matching those of the acquired real sea data sets. The introduced simulation model reproduces the multichannel properties of real data for different sea states, different grazing angles and with existing fast scatterers.
Several applications can benefit from the introduced analysis. To monitor the ocean surface more precisely, the insight into the multichannel properties of sea clutter can be exploited to estimate parameters describing the sea surface. Further, the application of space-time adaptive processing (STAP) to maritime radar systems benefits from this analysis, because this thesis provides simulation and calculation models to evaluate the STAP performance in dependence on radar and sea parameters.
The necessity to use STAP in order to reliably detect small maritime targets from airborne radar systems is demonstrated in this thesis by performing further experiments with the radar system PAMIR and a small cooperative boat. The acquired data is used to analyze the detectability of this target without any processing, with time adaptive processing (TAP), and with STAP. The evaluation of these experiments shows that without any processing the signal-to-clutter plus noise ratio (SCNR) of this boat is too low to be detected. If TAP is applied, the target signal is often suppressed by this filter, preventing its detection. With STAP, however, the cooperative boat is almost always identified within the data sets of the presented experiments.
Multichannel processing for maritime radar systems is a new field of research, where several questions are still unanswered. One important issue are the dependencies of sea clutter multichannel properties on various sea and weather parameters. To evaluate these dependencies, further experiments need to be performed with precise in-situ measurements. It would also be useful to mount the PAMIR system on a stationary platform, in order to exclude influences of the moving platform. Furthermore, the demonstrated multichannel analysis refers to sea surfaces in deep waters. For several applications, like for harbour survaillance, an evaluation of multichannel sea clutter properties for shallow waters is of interest as well. To exploit further the processing possibilities of a coherent airborne radar system, the sea clutter multichannel analysis has to be extended to

synthetic aperture radar (SAR). It is expected that more features of the sea surface are recognized with this processing technique.
With multichannel processing an improved detection performance for airborne radar systems can be achieved. However, further improvement is possible if better detection techniques are developed. One possible source of improvement is the reduction of false alarms due to fast scatterers after STAP. To obtain a more general statement of possible detection performances with different processings, also experiments during different sea states with targets of different sizes and moving with different radial velocities have to be carried out and analyzed.

List of Abbrevations

CNR	Clutter-to-Noise Ratio
CPI	Coherent Processing Interval
CUT	Cell under Test
DGPS	Differential Global Positioning System
DOA	Direction of Arrival
ECEF	Earth-Centered Earth-Fixed
ENU	East-North-Up
GMTI	Ground Moving Target Indication
IMU	Inertial Measuring Unit
LOS	Line of sight
MTI	Moving Target Indication
PAMIR	Phased Array Multifunctional Imaging Radar
PRF	Pulse Repetition Frequency
RCS	Radar Cross Section
SAR	Synthetic Aperture Radar
SNR	Signal-to-Noise Ratio
STAP	Space-Time Adaptive Processing
TAP	Time Adaptive Processing

List of Symbols

Latin Symbols

$A(u)$	Reflectivity as random variable
$A_f(u)$	Reflectivity of fast scatterers as random variable
B	Bernoulli random variable
c	Speed of light
$\mathbf{c}_p$	Phase velocity vector of water wave
$c(T)$	Clutter signal in time domain
$\tilde{\mathbf{c}}$	Space-time clutter signal vector
$C(F)$	Clutter signal in frequency domain
$\mathbf{C}_c(F)$	Clutter spectral density matrix
$\mathbf{C}_f(F)$	Spectral density matrix of fast scatterers
$\mathbf{C}_n(F)$	Noise spectral density matrix
$\mathbf{C}_s(F)$	Spectral density matrix of slow scatterers
$C_w(F)$	Spectral density of water waves
$\mathbf{C}_z(F)$	Spectral density matrix of received signal
$\mathbf{d}(u)$	DOA-vector
$\mathbf{d}_0(u)$	DOA-vector without considering the antenna pattern
$D(u)$	Two-way antenna pattern
$\mathbf{e}_n(F)$	Eigenvector of spectral density matrix

$E\{\cdot\}$	Expectation value
f_r	Carrier radar frequency
f_s	Water wave frequency
F	Frequency
$F(\cdot)$	Doppler frequency
F_c	Doppler centroid
g	Gravity constant
$\mathbf{g}(F(\cdot))$	Doppler vector
$H(F)$	Fourier transform of elevation function
H_s	Water wave height
$\mathbf{k}_r$	Radar wave vector
$\mathbf{k}_s$	Water wave vector
M	Number of pulses of one CPI
N	Number of available channels
$p^{V_s}(v_s)$	Distribution of radial sea scatterer velocity
$\mathbf{r}$	Distance vector
r_t	Target slant range
$R_c(\tau)$	Clutter covariance matrix
$s(\cdot)$	Normalized time-dependent radar clutter signal
$\tilde{\mathbf{s}}(\cdot)$	Normalized space-time clutter signal vector
T	Slow time
u	Directional cosine, look direction
$u_0(F)$	Look direction of stationary scatterers
$\mathbf{u}_c$	LOS vector to center position
$\mathbf{u}_t$	LOS vector to target position

$\mathbf{u}$	LOS vector
U_w	Wind velocity
$\mathbf{v}_c$	Clutter velocity vector
$\mathbf{v}_{orb}$	Orbital water wave velocity vector
$\mathbf{v}_p$	Platform velocity vector
v_r	Radial target velocity
v_{rel}	Relative radial velocity
v_s	Radial sea scatterer velocity as realization
$\mathbf{v}_t$	Target velocity vector
$V_f(u)$	Radial velocity of fast scatterers as random variable
$V_s(u)$	Radial sea scatterer velocity as random variable
$\mathbf{w}(u, F)$	Space-time filter
$\mathbf{x}_c = (x_c, y_c, z_c)^T$	Clutter position vector
x_n	Position of nth channel
$\mathbf{x}_p = (x_p, y_p, z_p)^T$	Platform position vector
$\mathbf{x}_t = (x_t, y_t, z_t)^T$	Target position vector
$z(T)$	Received signal in time domain
$Z(F)$	Received signal in frequency domain

Greek Symbols

α	Cone angle
$\gamma(u, F)$	Space-time filter gain
$\delta(\cdot)$	Dirac delta distribution
$\eta(\cdot)$	Elevation function of sea surface

θ	Grazing angle
$\lambda_n(F)$	Eigenvalue of spectral density matrix
λ_r	Carrier radar wave length
λ_s	Wave length of water wave
μ_B	Expectation value of Bernoulli random variable
μ_f	Expectation value of radial sea scatterer velocity of fast scatterers
ρ_l	Channel correlation of land clutter
$\rho_{nn'}$	Channel correlation between channels n and n'
ρ_s	Channel correlation of sea clutter
σ_a^2	Broadness of absolute squared value of two-way antenna pattern
σ_c^2	Reflectivity variance
σ_{cf}^2	Reflectivity variance of fast scatterers
σ_f^2	Radial sea scatterer velocity variance of fast scatterers
σ_n^2	Noise variance
σ_{orb}^2	Orbital velocity variance
σ_{pm}^2	Orbital velocity variance calculated with Pierson-Moskowitz spectrum
σ_s^2	Radial sea scatterer velocity variance
$\hat{\sigma_s}^2$	Estimated radial sea scatterer velocity variance
φ	Azimuth angle
φ_{ENU}	Azimuth angle between x-axis in ENU-coordinates and center position
φ_s	Azimuth angle between x-axis and direction of water wave

Appendix A

Boundary Conditions to Calculate Flow Velocity of Water Waves

The flow is assumed to be incompressible

$$\nabla \mathbf{v}_{orb}(\mathbf{x}, z, t) = 0. \tag{A.1}$$

Using further that the flow velocity is irrotational

$$\nabla \times \mathbf{v}_{orb}(\mathbf{x}, z, t) = 0, \tag{A.2}$$

allows to define a velocity potential $\Phi(\mathbf{x}, z, t)$, which is related to the flow velocity by

$$\mathbf{v}_{orb}(\mathbf{x}, z, t) = \nabla \Phi(\mathbf{x}, z, t). \tag{A.3}$$

This equation allows to rewrite equation (A.1) as

$$\nabla^2 \Phi(\mathbf{x}, z, t) = 0, \tag{A.4}$$

which is the Laplace equation.
To solve this equation, boundary conditions have to be defined. The first boundary condition is the so-called bottom boundary condition, which states that the vertical velocity has to be zero on the floor, hence

$$\left.\frac{\partial \Phi(\mathbf{x}, z, t)}{\partial z}\right|_{z=-H} = 0. \tag{A.5}$$

The kinematic boundary condition is due to the fact that particles on the surface stay on the surface, if wave breaking is not considered. Therefore, the velocity of the particles on the surface has to equal the velocity of the surface itself

$$\frac{\partial \eta(\mathbf{x}, t)}{\partial t} = \left.\frac{\partial \Phi(\mathbf{x}, z, t)}{\partial z}\right|_{z=0}, \tag{A.6}$$

where $\eta(\mathbf{x}, t)$ is the elevation function of the sea surface. Here the amplitudes of the waves are additionally assumed to be small, which allows to observe the vertical velocity at $z = 0$. The dynamic boundary condition assumes that the atmospheric pressure is equal to the pressure on the surface. Assuming them to be zero and using the Bernoulli equation to calculate the pressure on the surface allows to state the condition as

$$\left.\frac{\partial \Phi(\mathbf{x}, z, t)}{\partial t}\right|_{z=\eta(\mathbf{x},t)} + \frac{1}{2}||\mathbf{v}_{orb}(\mathbf{x}, \eta(\mathbf{x}, t), t)||^2 + g\eta(\mathbf{x}, t) = 0. \tag{A.7}$$

Because the velocity term is of second order, it is assumed to be much smaller than the other terms, and is therefore neglected. If only waves with small amplitudes are considered, the boundary condition can be stated as

$$\left.\frac{\partial \Phi(\mathbf{x}, z, t)}{\partial t}\right|_{z=0} = -g\eta(\mathbf{x}, t), \tag{A.8}$$

where g denotes the gravity constant.

Appendix B

Calculation of Scattering from Sea Surface

Here the detailed calculations are described to derive the magnetic scattering field of equation (3.19) from equation (3.18).
The normal vector can be calculated from

$$\mathbf{n}(\mathbf{x}) = \frac{\mathbf{v}_x(\mathbf{x}) \times \mathbf{v}_y(\mathbf{x})}{||\mathbf{v}_x(\mathbf{x}) \times \mathbf{v}_y(\mathbf{x})||}, \tag{B.1}$$

where $\mathbf{v}_x(\mathbf{x})$ and $\mathbf{v}_y(\mathbf{x})$ are vectors which span the plane to which $\mathbf{n}(\mathbf{x})$ is orthogonal. With the defined clutter position vector, the two vectors can be approximated by

$$\begin{aligned} \mathbf{v}_x(\mathbf{x_c}) &\approx dx \frac{\partial \mathbf{x}_c}{\partial x} \\ &= dx \left(1, 0, \frac{\partial \eta(x,y)}{\partial x}\right)^T \end{aligned} \tag{B.2}$$

and

$$\begin{aligned} \mathbf{v}_y(\mathbf{x}_c) &\approx dy \frac{\partial \mathbf{x}_c}{\partial y} \\ &= dy \left(0, 1, \frac{\partial \eta(x,y)}{\partial y}\right)^T. \end{aligned} \tag{B.3}$$

Because $dA = ||\mathbf{v}_x(\mathbf{x}_c) \times \mathbf{v}_y(\mathbf{x}_c)||$, the product of the normal vector and the infinitesimal area element equals

$$\mathbf{n}(\mathbf{x}_c) dA = dxdy \left(-\frac{\partial \eta(x,y)}{\partial x}, -\frac{\partial \eta(x,y)}{\partial y}, 1\right)^T. \tag{B.4}$$

For the following calculations, the free space Green's function is chosen

$$G(\mathbf{x}_p, \mathbf{x}_c) = \frac{\exp\{jk_r||\mathbf{x}_p - \mathbf{x}_c||\}}{4\pi||\mathbf{x}_p - \mathbf{x}_c||}, \tag{B.5}$$

where k_r is the wave number of the transmitted radar wave. For a derivation of this function, see for example [89]. The gradient of this function can be calculated as

$$\nabla G(\mathbf{x}_p, \mathbf{x}_c) = \frac{1}{4\pi}(\mathbf{x}_p - \mathbf{x}_c)\frac{\exp\{jk_r||\mathbf{x}_p - \mathbf{x}_c||\}}{||\mathbf{x}_p - \mathbf{x}_c||^3}(jk_r||\mathbf{x}_p - \mathbf{x}_c|| - 1). \tag{B.6}$$

The term, which contains $\frac{1}{||\mathbf{x}_p-\mathbf{x}_c||^3}$, is neglected, because it is assumed that $\frac{1}{||\mathbf{x}_p-\mathbf{x}_c||^3} << \frac{1}{||\mathbf{x}_p-\mathbf{x}_c||^2}$. Further, $\mathbf{x}_c$ is neglected in the amplitude, because it is chosen near the origin of the coordinate system. To calculate the phase, the approximation $||\mathbf{x}_p - \mathbf{x}_c|| \approx ||\mathbf{x}_p|| - \frac{\mathbf{x}_p^H\mathbf{x}_c}{||\mathbf{x}_p||}$ is used. This reduces the gradient of the free space Green's function to

$$\nabla G(\mathbf{x}_p, \mathbf{x}_c) = \frac{j}{4\pi}\frac{\mathbf{k}_r}{||\mathbf{x}_p||}\exp\{jk_r||\mathbf{x}_p||\}\exp\left\{-j\mathbf{k}_r^H\mathbf{x}_c\right\}. \tag{B.7}$$

Here additionally $\mathbf{k}_r = k_r\frac{\mathbf{x}_p}{||\mathbf{x}_p||}$ is defined.
To calculate the scattering field in equation (3.18), an assumption about the magnetic field at position $\mathbf{x}_c$ has to be made. Here the Kirchhoff assumption is used, which states that

$$\mathbf{B}(\mathbf{x}_c) = 2\mathbf{B}_r(\mathbf{x}_c), \tag{B.8}$$

where $\mathbf{B}_r(\mathbf{x})$ is the field, which is transmitted by the radar. It is assumed that the radar transmits a plane wave, which can be described as

$$\mathbf{B}_r(\mathbf{x}) = \mathbf{B}_0\exp\left\{-j\mathbf{k}_r^H\mathbf{x}\right\}, \tag{B.9}$$

where $\mathbf{B}_0$ is the amplitude vector of the magnetic field.
Using equations (B.4), (B.7) and (B.8) allows to state equation (3.18) as

$$\begin{aligned}\mathbf{B}_s(\mathbf{x}_p) = -\iint_A \left(\left(-\frac{\partial\eta(x,y)}{\partial x}, -\frac{\partial\eta(x,y)}{\partial y}, 1\right)^T \times 2\mathbf{B}_0\exp\left\{-j\mathbf{k}_r^H\mathbf{x}_c\right\}\right) \\ \times \frac{j}{4\pi}\frac{\mathbf{k}_r}{||\mathbf{x}_p||}\exp\{jk_r||\mathbf{x}_p||\}\exp\left\{-j\mathbf{k}_r^H\mathbf{x}_c\right\}\, dx\, dy.\end{aligned} \tag{B.10}$$

Using Lagrange's formula to calculate the triple cross product and considering that the magnetic field is orthogonal to the propagation direction ($\mathbf{B}_0^H\mathbf{k}_r = 0$), equation (B.10) can be rewritten as

$$\begin{aligned}\mathbf{B}_s(\mathbf{x}_p) = \frac{-j\mathbf{B}_0\exp\{jk_r||\mathbf{x}_p||\}}{2\pi||\mathbf{x}_p||}\iint_A \left(-\frac{\partial\eta(x,y)}{\partial x}k_{rx} - \frac{\partial\eta(x,y)}{\partial y}k_{ry} + k_{rz}\right) \\ \exp\{-j2(k_{rx}x + k_{ry}y)\}\exp\{-j2\eta(x,y)k_{rz}\}\, dx\, dy.\end{aligned} \tag{B.11}$$

It is shown in [90] that terms which include a derivative of $\eta(x, y)$ can be neglected, because they only change the result by a constant factor. Due to the assumption of a

small amplitude surface, the second exponential term can be approximated by a Taylor series as

$$\exp\{-j2\eta(x,y)k_{rz}\} \approx 1 - j2k_{rz}\eta(x,y). \tag{B.12}$$

The magnetic field resulting from the first term in equation (B.12) can be neglected, because it is the specular reflection.

Appendix C

Change of Basis and Eigenvalues of the Clutter Spectral Density Matrix

In this section the bases of the following approximated clutter spectral density matrix

$$\begin{aligned}\mathbf{C}_c(F) \approx \sigma_c^2 E\left\{\left|D\left(u_0(F)+\frac{V_s(u)}{v_p}\right)\right|^2\right\}\mathbf{e}\left(u_0(F)\right)\mathbf{e}^H\left(u_0(F)\right)\\ +\frac{\sigma_c^2}{v_p}E\left\{V_s(u)\left|D\left(u_0(F)+\frac{V_s(u)}{v_p}\right)\right|^2\right\}\mathbf{e}\left(u_0(F)\right)\mathbf{e}'^H\left(u_0(F)\right)\\ +\frac{\sigma_c^2}{v_p}E\left\{V_s(u)\left|D\left(u_0(F)+\frac{V_s(u)}{v_p}\right)\right|^2\right\}\mathbf{e}'\left(u_0(F)\right)\mathbf{e}^H\left(u_0(F)\right)\\ +\frac{\sigma_c^2}{v_p^2}E\left\{V_s^2(u)\left|D\left(u_0(F)+\frac{V_s(u)}{v_p}\right)\right|^2\right\}\mathbf{e}'\left(u_0(F)\right)\mathbf{e}'^H\left(u_0(F)\right)\end{aligned} \tag{C.1}$$

are changed.
Let $\mathbf{B}(F)$ be the $N \times N$ change of basis matrix

$$\mathbf{B}(F)=\left(\frac{\mathbf{e}(u_0(F))}{||\mathbf{e}(u_0(F))||}\frac{\mathbf{e}'(u_0(F))}{||\mathbf{e}'(u_0(F))||}\mathbf{b}_3(F)\dots\mathbf{b}_N(F)\right), \tag{C.2}$$

where all vectors are orthonormal to each other. The clutter spectral density matrix in the new bases can be calculated as

$$\begin{aligned}\mathbf{C}_B(F)&=\mathbf{B}^{-1}(F)\mathbf{C}_c(F)\mathbf{B}(F)\\ &=\sigma_c^2\begin{pmatrix}c_1(F) & c_2(F) & 0 & \dots & 0\\ c_2(F) & c_3(F) & 0 & \dots & 0\\ 0 & \dots & & & 0\\ \vdots & & & & \vdots\\ 0 & \dots & & & 0\end{pmatrix},\end{aligned} \tag{C.3}$$

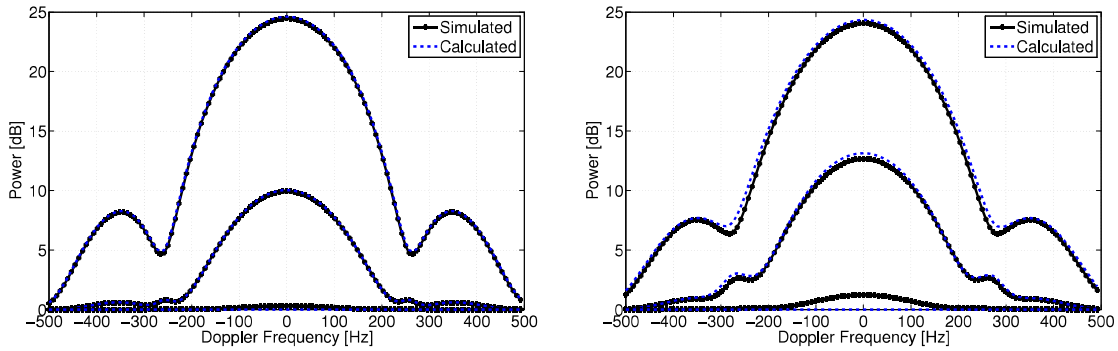

(a) $\sigma_s^2 = 0.2\ \mathrm{m}^2/\mathrm{s}^2$ (b) $\sigma_s^2 = 0.5\ \mathrm{m}^2/\mathrm{s}^2$

Figure C.1: Calculated and numerically computed eigenvalue distributions in dependence of the Doppler frequency. The eigenvalues are estimated from the numerically computed spectral density matrix from equation (5.8) and calculated from equation (C.4).

with $c_1(F) = E\left\{|D(u(F, V_s(u)))|^2\right\} ||\mathbf{e}(u_0(F))||^2$,
$c_2(F) = E\left\{\frac{V_s(u)}{v_p}|D(u(F, V_s(u)))|^2\right\} ||\mathbf{e}(u_0(F))||||\mathbf{e}'(u_0(F))||$ and
$c_3(F) = E\left\{\frac{V_s^2(u)}{v_p^2}|D(u(F, V_s(u)))|^2\right\} ||\mathbf{e}'(u_0(F))||^2$. The matrix $\mathbf{C}_B(F)$ is clearly a rank two matrix, and the eigenvalues can easily be calculated as

$$\lambda_{1/2}(F) = \frac{\sigma_c^2}{2}\left(c_1(F) + c_3(F) \pm \zeta(F)\right), \tag{C.4}$$

with $\zeta(F) = \sqrt{(c_1(F) - c_3(F))^2 + 4c_2^2(F)}$. Because the matrices $\mathbf{C}_c(F)$ in equation (C.1) and $\mathbf{C}_B(F)$ in equation (C.3) are similar matrices, their rank and eigenvalues are equal. Therefore $\mathbf{C}_c(F)$ is also a rank two matrix whose eigenvalues can be calculated from equation (C.4).
In figure C.1 eigenvalues are computed from the simulated clutter spectral density matrix of equation (5.8) and calculated with equation (C.4) for two different radial sea scatterer velocity variances. The expected value terms were evaluated with a Monte Carlo simulation. For both computations a Gaussian distribution of the radial sea scatterer velocity is assumed. Figure C.1 validates the calculation of the first two eigenvalues of the clutter spectral density matrix with equation (C.4).
To derive the eigenvalues from equation (C.4) analytically, a Gaussian distribution for the radial sea scatterer velocity

$$p^{V_s}(v_s) = \frac{1}{\sqrt{2\pi}\sigma_s}\exp\left\{-\frac{v_s^2}{2\sigma_s^2}\right\} \tag{C.5}$$

and a Gauss function for the absolute squared value of the two-way antenna pattern

$$|D(u(F, V_s(u)))|^2 = \exp\left\{-\frac{u^2(F, V_s(u))}{2\sigma_a^2}\right\} \tag{C.6}$$

are assumed. Then $c_2(F)$ from equation (C.3) can be evaluated from

$$c_2(F) = ||\mathbf{d}(u_0(F))||||\mathbf{d}'(u_0(F))||\frac{1}{\sqrt{2\pi}\sigma_s} \cdot \int_{-\infty}^{\infty} \frac{v_s}{v_p} \exp\left\{-\frac{u_0(F)v_s}{\sigma_a^2}\right\} \exp\left\{-av_s^2\right\} dv_s, \tag{C.7}$$

with $a = \frac{\left(\sigma_a^2 + \frac{\sigma_s^2}{v_p^2}\right)}{2\sigma_a^2\sigma_s^2}$.

If the eigenvalues are only calculated around the Doppler centroid, the first exponential function can be approximated by 1, which results in $c_2(F) \approx 0$.
Considering the outcome of equation (C.7) and estimating around the Doppler centroid to calculate $c_1(F)$ and $c_3(F)$, allows to state the eigenvalues from equation (C.4) as

$$\begin{aligned}\lambda_1(F) &\approx \sigma_c^2||\mathbf{d}(u_0(F))||^2\frac{1}{\sqrt{2\pi}\sigma_s}\int_{-\infty}^{\infty}\exp\left\{-av_s^2\right\}dv_s \\ \lambda_2(F) &\approx \frac{\sigma_c^2}{v_p^2}||\mathbf{d}'(u_0(F))||^2\frac{1}{\sqrt{2\pi}\sigma_s}\int_{-\infty}^{\infty}v_s^2\exp\left\{-av_s^2\right\}dv_s.\end{aligned} \tag{C.8}$$

The first eigenvalue is calculated by using the relationship $\int_{-\infty}^{\infty}\exp\left\{-av_s^2\right\}\ dv_s = \sqrt{\frac{\pi}{a}}$, which can for example be found in [79]. To calculate the integral of the second eigenvalue, a substitution with $t = av_s^2$ is chosen. Then the integral can be calculated by considering that the function inside the integral is even and that the integral corresponds to the Gamma function $\Gamma(\frac{3}{2}) = \frac{\sqrt{\pi}}{2}$.
The first two eigenvectors of the matrix $\mathbf{C}_B(F)$ can be calculated as

$$\begin{aligned}\mathbf{u}_1^B(F) &= \left(1, \frac{2c_2(F)}{c_1(F) - c_3(F) + \zeta(F)}, 0, \ldots, 0\right)^T \\ \mathbf{u}_2^B(F) &= \left(-\frac{2c_2(F)}{c_1(F) - c_3(F) + \zeta(F)}, 1, 0, \ldots, 0\right)^T.\end{aligned} \tag{C.9}$$

To compute the eigenvectors of $\mathbf{C}_c(F)$, the eigenvectors in equation (C.9) have to be multiplied with the change of basis matrix. If $\zeta(F)$ can be approximated as $\zeta(F) \approx c_1(F) - c_3(F)$ around the Doppler centroid, the eigenvectors of the clutter spectral density matrix are equal to

$$\begin{aligned}\mathbf{u}_1(F) &= \frac{\mathbf{e}(u_0(F))}{||\mathbf{e}(u_0(F))||} + \frac{c_2(F)}{c_1(F) + c_3(F)}\frac{\mathbf{e}'(u_0(F))}{||\mathbf{e}'(u_0(F))||} \\ \mathbf{u}_2(F) &= \frac{\mathbf{e}'(u_0(F))}{||\mathbf{e}'(u_0(F))||} - \frac{c_2(F)}{c_1(F) + c_3(F)}\frac{\mathbf{e}(u_0(F))}{||\mathbf{e}(u_0(F))||}.\end{aligned} \tag{C.10}$$

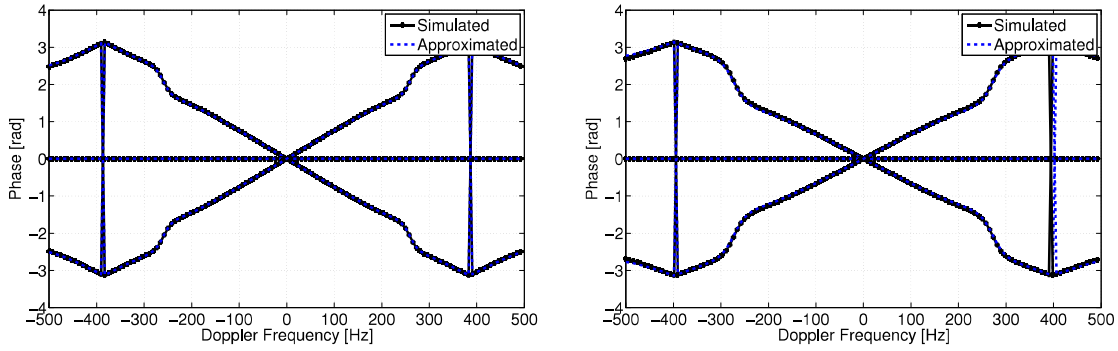

(a) $\sigma_s^2 = 0.2\ \mathrm{m}^2/\mathrm{s}^2$ (b) $\sigma_s^2 = 0.5\ \mathrm{m}^2/\mathrm{s}^2$

Figure C.2: Phase of the first eigenvector in dependence of the Doppler frequency. The eigenvector is estimated from the numerically computed spectral density matrix from equation (5.8) and analytically calculated from the approximations in equation (C.10).

In figure C.2 the phase of the first eigenvector is evaluated from the simulated spectral density matrix in equation (5.8) and compared to the phase of the approximated eigenvector from equation (C.10) for two different radial sea scatterer velocity variances. Also here a Gaussian distribution of the radial sea scatterer velocity is assumed and the expected value terms in equation (C.10) are computed in the same manner as for the eigenvalues in equation (C.4). Figure 5.3 demonstrates that for both radial sea scatterer velocity variances the calculated phase of the first eigenvector matches quite well the one of the simulated matrix.

Appendix D

Approximation of the Spectral Density Matrix with three Taylor terms

To approximate the spectral density matrix of sea clutter more accurately, the DOAvector is described by a Taylor series with three terms

$$\mathbf{d}_0\left(u_0(F)+\frac{V_s(u)}{v_p}\right)\approx \mathbf{d}_0\left(u_0(F)\right)+\frac{V_s(u)}{v_p}\mathbf{d}_0'\left(u_0(F)\right)+\frac{1}{2}\frac{V_s^2(u)}{v_p^2}\mathbf{d}_0''\left(u_0(F)\right). \quad \text{(D.1)}$$

Here $\mathbf{d}_0''(u_0(F))$ corresponds to

$$\mathbf{d}_0''(u_0(F))=\left(-\frac{4\pi^2}{\lambda_r^2}x_n^2\exp\left\{j\frac{2\pi}{\lambda_r}u_0(F)x_n\right\}\right)_{n=1}^{N}. \quad \text{(D.2)}$$

With this approximation, the spectral density matrix can be stated as

$$\begin{aligned}\mathbf{C}_c(F)\approx\sigma_c^2E\Bigg\{&\left|D\left(u_0(F)+\frac{V_s(u)}{v_p}\right)\right|^2\\&\left(\left(\mathbf{d}_0\left(u_0(F)\right)+\frac{V_s(u)}{v_p}\mathbf{d}_0'\left(u_0(F)\right)+\frac{1}{2}\frac{V_s^2(u)}{v_p^2}\mathbf{d}_0''\left(u_0(F)\right)\right)\right.\\&\left.\left(\mathbf{d}_0\left(u_0(F)\right)+\frac{V_s(u)}{v_p}\mathbf{d}_0'\left(u_0(F)\right)+\frac{1}{2}\frac{V_s^2(u)}{v_p^2}\mathbf{d}_0''\left(u_0(F)\right)\right)^H\right)\Bigg\}. \quad \text{(D.3)}\end{aligned}$$

For the following analysis the assumptions of $V_s(u)$ being a zero mean random variable and not influencing the antenna pattern are used. To calculate the spectral density matrix, terms in the order of $\frac{V_s^4(u)}{v_p^4}x_n^4$ are neglected, resulting in

$$\begin{aligned}\mathbf{C}_c(F)\approx{}&\sigma_c^2\mathbf{d}(u_0(F))\mathbf{d}^H(u_0(F))+\frac{1}{2}\frac{\sigma_c^2\sigma_s^2}{v_p^2}\mathbf{d}(u_0(F))\mathbf{d}''^H(u_0(F))\\&+\frac{1}{2}\frac{\sigma_c^2\sigma_s^2}{v_p^2}\mathbf{d}''(u_0(F))\mathbf{d}^H(u_0(F))+\frac{\sigma_c^2\sigma_s^2}{v_p^2}\mathbf{d}'(u_0(F))\mathbf{d}'^H(u_0(F)). \quad \text{(D.4)}\end{aligned}$$

The approximated spectral density matrix in equation (D.4) consists of a sum of four rank one matrices. It is assumed that the contribution of the first matrix to the spectral density matrix is much higher than the contributions of the second and the third matrix. The second matrix has the same eigenvector as the first one, while the third matrix has a different one. The first order contribution to the first eigenvalue of this matrix is calculated by using the perturbation method (for a detailed description of this method see appendix E) as

$$\delta\lambda_1(F) = \frac{1}{2}\frac{\sigma_s^2\sigma_c^2}{v_p^2}\mathbf{d}^H(u_0(F))\mathbf{d}''(u_0(F)). \tag{D.5}$$

It is assumed that the first eigenvector is not changed by the third matrix of equation (D.4). The first eigenvalue of the spectral density matrix can be calculated from the sum of the contributions of the first three matrices as

$$\lambda_1(F) = \sigma_c^2||\mathbf{d}(u_0(F))||^2 - \sigma_c^2\frac{\sigma_s^2}{v_p^2}||\mathbf{d}'(u_0(F))||^2. \tag{D.6}$$

Here for more clarity $\mathbf{d}^H(u_0(F))\mathbf{d}''(u_0(F)) = \mathbf{d}''^H(u_0(F))\mathbf{d}(u_0(F)) = -||\mathbf{d}'(u_0(F))||^2$ was used.
The fourth matrix of equation (D.4) corresponds to the second matrix of equation (5.15). It spans a second dimension of the clutter subspace. Its eigenvector and eigenvalue correspond to the ones in chapter 5.2. Only the fourth matrix of this equation contributes to the second eigenvalue of the clutter spectral density matrix, because its eigenvector is orthogonal to all the other eigenvectors of the matrices in equation (D.4).
Using the calculated eigenvalues and considering that $\mathbf{C}_c(F)$ is a symmetrical matrix, it can be represented as

$$\begin{aligned}\mathbf{C}_c(F) &= \lambda_1(F)\frac{\mathbf{d}(u_0(F))\mathbf{d}^H(u_0(F))}{||\mathbf{d}(u_0(F))||^2} + \lambda_2(F)\frac{\mathbf{d}'(u_0(F))\mathbf{d}'^H(u_0(F))}{||\mathbf{d}'(u_0(F))||^2} \\ &= \sigma_c^2\left(1 - \frac{\sigma_s^2}{v_p^2}\frac{||\mathbf{d}'(u_0(F))||^2}{||\mathbf{d}(u_0(F))||^2}\right)\mathbf{d}\left(u_0(F)\right)\mathbf{d}^H\left(u_0(F)\right) \\ &\quad + \sigma_c^2\frac{\sigma_s^2}{v_p^2}\mathbf{d}'\left(u_0(F)\right)\mathbf{d}'^H\left(u_0(F)\right).\end{aligned} \tag{D.7}$$

Because the trace of the spectral density matrix equals the sum of the two eigenvalues, no further eigenvalues have to be accounted for.

Appendix E

Perturbation Method for Eigenvalue Problems

Consider a matrix, which is a sum of an original matrix and a perturbation matrix. The eigenvalues and eigenvectors of this matrix are functions of the error δ, which is produced by the perturbation matrix. Now the clutter spectral density matrix $\mathbf{C}_c(F) = \mathbf{C}_s(F) + \mathbf{C}_f(F)$ is examined, where the spectral density matrix of slow scatterers $\mathbf{C}_s(F)$ is the original matrix and the spectral density matrix of fast scatterers $\mathbf{C}_f(F)$ is the perturbation matrix. The perturbation matrix $\mathbf{C}_f(F)$ causes the error $\Delta\delta$, which is assumed to be small, allowing to approximate the eigenvalue and eigenvector of dimension n by the first order Taylor series as

$$\lambda_n(F, \Delta\delta) \approx \lambda_n(F, 0) + \Delta\delta\lambda'_n(F, 0) \tag{E.1}$$

$$\mathbf{u}_n(F, \Delta\delta) \approx \mathbf{u}_n(F, 0) + \Delta\delta\mathbf{u}'_n(F, 0), \tag{E.2}$$

where $\lambda_n(F, 0)$ and $\mathbf{u}_n(F, 0)$ are the eigenvalue and eigenvector of matrix $\mathbf{C}_s(F)$ and $\lambda'_n(F, 0)$ and $\mathbf{u}'_n(F, 0)$ are their derivatives at $\delta = 0$.
Consider further the eigenproblem for the dimension n

$$\mathbf{C}_c(F)\mathbf{u}_n(F, \Delta\delta) = \lambda_n(F, \Delta\delta)\mathbf{u}_n(F, \Delta\delta). \tag{E.3}$$

With equations (E.1) and (E.2), equation (E.3) can be rewritten for first order perturbations as

$$\begin{aligned}&\mathbf{C}_f(F)\mathbf{u}_n(F, 0) + \mathbf{C}_s\Delta\delta\mathbf{u}'_n(F, 0)\\ &= \lambda_n(F, 0)\Delta\delta\mathbf{u}'_n(F, 0) + \mathbf{u}_n(F, 0)\Delta\delta\lambda'_n(F, 0).\end{aligned} \tag{E.4}$$

If the eigenvalues of matrix $\mathbf{C}_s(F)$ are distinct, the eigenvectors of this matrix span the whole N-dimensional space and can be chosen as a basis for the derived eigenvectors (see [91])

$$\Delta\delta\mathbf{u}'_n(F, 0) = \sum_i c_{in}(F)\mathbf{u}_i(F, 0), \tag{E.5}$$

where $c_{in}(F)$ are some constants. Using equation (E.5), equation (E.4) can be rewritten as

$$\begin{aligned}&\mathbf{C}_f(F)\mathbf{u}_n(F,0) + \mathbf{C}_s(F)\sum_i c_{in}(F)\mathbf{u}_i(F,0)\\ &= \Delta\delta\lambda_n'(F,0)\mathbf{u}_n(F,0) + \lambda_n(F,0)\sum_i c_{in}(F)\mathbf{u}_i(F,0).\end{aligned} \tag{E.6}$$

Multiplying both left sides of equation (E.6) with $\mathbf{u}_n^H(F,0)$ and assuming that $\mathbf{C}_s(F)$ is symmetric allows to calculate the change of the eigenvalue due to $\Delta\delta$ as

$$\Delta\delta\lambda_n'(F,0) = \frac{\mathbf{u}_n^H(F,0)\mathbf{C}_f(F)\mathbf{u}_n(F,0)}{||\mathbf{u}_n(F,0)||^2}. \tag{E.7}$$

To determine the constant $c_{kn}(F)$, equation (E.6) is multiplied on the left side with $\mathbf{u}_k^H(F,0)$, where $k \neq n$, which results in

$$c_{kn}(F) = \frac{\mathbf{u}_k^H(F,0)\mathbf{C}_f(F)\mathbf{u}_n(F,0)}{||\mathbf{u}_k(F,0)||^2(\lambda_n(F,0) - \lambda_k(F,0))}. \tag{E.8}$$

The constant $c_{nn}(F)$ is only certain if a normalization condition is imposed on the eigenvectors. These calculations were for example performed in [92] or [93].

Bibliography

[1] D. E. Barrick. HF Radio Oceanography- A Review. *Boundary Layer Meteorology*, 13:23–43, 1978.

[2] M. Skolnik. *Radar Handbook*. McGraw-Hill, 1990.

[3] D. D. Crombie. Doppler Spectrum of Sea Echo at -13.56 Mc/s. *Nature*, 175:201–227, 1955.

[4] S.O. Rice. Reflections of Electromagnetic Waves from Slightly Rough Surfaces. *Communications on Pure and Applied Mathematics*, 4:351–378, 1951.

[5] W. H. Peake. Theory of Radar Return from Terrain. *IRE International Convention Record*, 7:27–41, 1959.

[6] K. Hasselmann, R. K. Raney, W. J. Plant, W. Alpers, R. A. Shuchman, D. R. Lyzenga, C. L. Rufenach, and M. J. Tucker. Theory of Synthetic Aperture Radar Ocean Imaging: A MARSEN View. *Journal of Geophysical Research*, 90, No. C3:4659–4686, 1985.

[7] C. Brüning, W. R. Alpers, and J. G. Schröter. On the Focusing Issue of Synthetic Aperture Radar. *IEEE Transaction on Geoscience and Remote Sensing*, 29, No. 1:120–128, 1991.

[8] M. B. Kanevsky. On the Theory of SAR Ocean Wave Imaging. *IEEE Transaction on Geoscience and Remote Sensing*, 31, No. 5:1031–1035, 1993.

[9] J. W. Wright. A New Model for Sea Clutter. *IEEE Transactions on Antennas and Propagation*, 16:217–223, 1968.

[10] W. R. Alpers, D. B. Ross, and C. L. R. On the Detectability of Ocean Surface Waves by Real and Synthetic Aperture Radar. *Journal of Geophysical Research*, 86, No. C7:6481–6498, 1981.

[11] W. J. Plant. *Radar Scattering from Modulated Wind Waves*. Kluwer Academic Press, 1989.

[12] W. R. Alpers and C. Bruening. On the Relative Importance of Motion-Related Contributions to the SAR Imaging Mechanism of Ocean Surface Waves. *IEEE Transactions on Geoscience and Remote Sensing*, 24:873–885, 1986.

[13] M. J. Tucker. The Decorrelation Time of Microwave Radar Echoes from the Sea Surface. *Int. J. Remote Sensing*, 6:1075–1089, 1985.

[14] R. E. Carande. Estimating Ocean Coherence Time Using Dual-Baseline Interferometric Synthetic Aperture Radar. *IEEE Transactions on Geoscience and Remote Sensing*, 32:846–854, 1994.

[15] R. K. Raney. SAR Response to Partially Coherent Phenomena. *IEEE Transaction on Antennas and Propagation*, AP-28, No. 6:777–787, 1980.

[16] R. M. Goldstein and H. A. Zebker. Interferometric Radar Measurement of Ocean Surface Currents. *Nature*, 328, No. 20:707–709, 1987.

[17] T. L. Ainsworth, S. R. Chubb, R. A. Fusina, R. M. Goldstein, and R. W. Jansen. INSAR Imagery of Surface Currents, Wave Fields and Fronts. *IEEE Transactions on Geoscience and Remote Sensing*, 33, No. 5:1117–1123, 1995.

[18] R. Romeiser. Current Measurement by Airborne Along-Trck InSAR: Measuring Technique and Experimental Results. *IEEE Journal of Oceanic Engineering*, 30, No. 3:552–569, 2005.

[19] D. Kim, W. M. Moon, D. Moller, and D. A. Imel. Measurements of Ocean Surface Waves and Currents Using L- and C-Band Along Track Interferometric SAR. *IEEE Transactions on Geoscience and Remote Sensing*, 41, No, 12:2821–2832, 2002.

[20] G. O. Marmorino, D. R. Thompson, H. C. Graber, and C. L. Trump. Correlation of Oceanographic Signatures appearing in Synthetic Aperture Radar and Interferometric Synthetic Aperture Radar Imagery with In Situ Measurements. *Journal of Geophysical Research*, 102, No. C8:18,723–18,736, 1997.

[21] D. R. Thompson and J. R. Jensen. Synthetic aperture radar interferometry applied to ship-generated waves in the 1989 loch linnhe experiment. *Journal of Geophysical Research*, 98:10,259–10,269, 1993.

[22] R. Romeiser and D. R. Thompson. Numerical Study on the Along-Track Interferometric Radar Imaging Mechanism of Oceanic Surface Currents. *IEEE Transactions on Geoscience and Remote Sensing*, 38:446–458, 2000.

[23] S. Watts, C. J. Baker, and K. D. Ward. Maritime Surveillance Radar Part 2: Detection Performance Prediction in Sea Clutter. *IEE Proceedings*, 137, No. 2:63–72, 1990.

[24] E. Conte, M. Lops, and G. Ricci. Asymptotically Optimum Radar Detection in Compound-Gaussian Clutter. *IEEE Transactions on Aerospace and Electronic Systems*, 31, No. 2:617–625, 1995.

[25] F. Gini and A. Farina. Vector Subspace Detection in Compound-Gaussian Clutter Part I: Survey and New Results. *IEEE Transactions on Aerospace and Electronic Systems*, 38, No. 4:1295–1311, 2002.

[26] P. I. Herselman and H. J. de Wind. Improved Covariance Matrix Estimation in Spectrally Inhomogeneous Sea Clutter with Application to Adaptive Small Boat Detection. In *Radar 2008*, 2008.

[27] W. N. Dawber and N.M. Harwood. Comparison of Doppler Clutter Cancellation Techniques for Naval Multi-Function Radars. *Radar, Sonar and Navigation, IEE Proceedings*, 150:37–40, 2003.

[28] R. Klemm. *Principles of Space-Time Adaptive Processing*. IEE, 2006.

[29] J. R. Guerci. *Space-Time Adaptive Processing for Radar*. Artech House, 2003.

[30] J. Ward. Space-Time Adaptive Processing for Airborne Radar. Technical report, MIT, 1994.

[31] J. H. G. Ender and A. R. Brenner. PAMIR - a Wideband Phased Array SAR/MTI System. *Radar, Sonar and Navigation, IEE Proceedings*, 150:165–172, 2003.

[32] J. H. G. Ender. Detection and Estimation of Moving Target Signals by Multi-Channel SAR. *AEÜ Int. J. Electron. Commun.*, 50:150–156, 1996.

[33] J. H. G. Ender. Space-time processing for multichannel synthetic aperture radar. *Electronics and Communication Engineering Journal*, 11:29–38, 1999.

[34] E. C. Barile, R. L. Fante, and J. A. Torres. Some Limitations on the Effectiveness of Airborne Adaptive Radar. *IEEE Transactions on Aerospace and Electronic Systems*, Vol. 28, NO. 4:1015–1032, 1992.

[35] M. McDonald, D. Cerutti-Maori, and A. Damini. Characterisation and cancellation of medium grazing angle sea clutter. In *EuRAD*, 2010.

[36] V. Gracheva and D. Cerutti-Maori. STAP Performance of Sea Clutter Supression in Dependency of the Grazing Angle and Swell Direction for High Resolution Bandwidth. In *IET Radar*, 2012.

[37] V. Gracheva and D. Cerutti-Maori. Multi-channel analysis of sea clutter for stap applications. In *EUSAR 2012*, 2012.

[38] V. Gracheva and D. Cerutti-Maori. First Results of Maritime MTI with PAMIR Multichannel Data. In *International Conference on Radar (Radar)*, 2013.

[39] V. Gracheva and J. Ender. Multichannel analysis of medium grazing angle sea clutter. In *EUSAR 2014*, 2014.

[40] V. Gracheva and J. Ender. Channel Correlation of Sea Data for Microwave Radar Systems. In *International Geoscience and Remote Sensing Symposium (IGARSS)*, 2015.

[41] V. Gracheva and J. Ender. Multichannel Ananlysis and Suppression of Sea Clutter for Airborne Microwave Radar Systems. *Submitted to: IEEE Transactions on Geoscience and Remote Sensing*, 2015.

[42] McGraw-Hill, editor. *Fundamentals of Radar Signal Processing*. M. A. Richards, 2005.

[43] I. A. Cumming and F. H. Wong. *Digital Processing of Synthetic Aperture Radar Data, Algorithms and Implementation.* Artech House, 2005.

[44] J. H. G. Ender. Signal Processig for Multi Channel SAR applied to the Experimental SAR System "AER". In *International Conference on Radar*, 1994.

[45] F. G. Bass, I. M. Fuks, A. I. Kalmykov, I. E. Ostrovsky, and A. D. Rosenberg. Very High Frequency Radiowave Scattering by a Distributed Sea Surface. *IEEE Transactions on Antennas and Propagation*, 5:560–568, 1968.

[46] G. B. Airy. On Tides and Waves. *Encyclopaedia Metropolitania*, 5, Article 192:241–396, 1845.

[47] H. Lamb. *Hydrodynamics*. Cambridge University Press, 1916.

[48] J. N. Newman. *Marine Hydrodynamics*. MIT Press, 1977.

[49] M. E. McCormick. *Ocean Engineering Mechanics*. Cambridge University Press, 2010.

[50] O. M. Phillips. *The Dynamics of the Upper Ocean*. Cambridge University Press, 1977.

[51] Blair Kinsman. *Wind Waves: Their Generation and Propagation on the Ocean Surface*. Prentice-Hall, 1965.

[52] J. F. Böhme. *Stochastische Signale*. Teubner-Studienbücher, 1998.

[53] M. B. Kanevsky. *Radar Imaging of the Ocean Waves*. Elsevier, 2009.

[54] W. J. Pierson and L. Moskowitz. A Proposed Spectral Form for Fully Developed Wind Seas Based on the Similarity Theory of S. A. Kitaigorodskii. *Journal of Geophysical Research*, 69:5181–5190, 1964.

[55] F. M. Monaldo and D. R. Lyzenga. On the Estimation of Wave-Slope- and Height-Variance Spectra from SAR Imagery. *IEEE Transactions on Geoscience and Remote Sensing*, GE-24:543–551, 1986.

[56] K. D. Ward, R. J. A. Tough, and S. Watts. *Sea Clutter: Scattering, the K Distribution and Radar Performance*. The Institution of Engineering and Technology, 2006.

[57] J. A. Stratton and L. J. Chu. Diffraction Theory of Electromagnetic Waves. *Physical Review*, 56:99–107, 1939.

[58] D. Holliday. Resolution of a Controversy Surrounding the Kirchoff Approach and the Small Perturbation Method in Rough Surface Scattering Theory. *IEEE Transactions on Antennas and Propagation*, 35:120–122, 1987.

[59] G. R. Valenzuela and M. B. Laing. Study of Doppler Spectra of Radar Sea Echo. *Journal of Geophysical Research*, 75:551–563, 1970.

[60] G. S. Brown. A Comparison of Approximate Theories for Scattering from Rough Surfaces. *Wave Motion*, 7:195–205, 1985.

[61] W. J. Plant and W. C. Keller. Evidence of Bragg Scattering in Microwave Doppler Spectra of Sea Return. *Journal of Geophysical Research*, 95:16,299–16,310, 1990.

[62] M. K. Gaughan, P. D. Komar, and J. H. Nath. *Breaking Waves: A Review of Theory and Measurements*. School of Oceanography, Oregon State University, 1973.

[63] S. R. Massel. *Ocean Wave Breaking and Marine Aerosol Fluxes*. Springer, 2007.

[64] T. Lamont-Smith, T. Waseda, and C. K. Rheem. Measurements of the Doppler Spectra of Breaking Waves. *IET Radar Sonar Navigation*, 1:149–157, 2007.

[65] O. M. Phillips. Radar Returns from the Sea Surface- Bragg scattering and Breaking Waves. *Journal of Physical Oceanography*, 18:1065–1074, 1988.

[66] T. Lamont-Smith, K. D. Ward, and D. Walker. A Comparison of EM Scattering Results and Radar Sea Clutter. In *Radar Conference*, 2002.

[67] M. Perlin, W. Choi, and Z. Tian. Breaking Waves in Deep and Intermediate Waters. *Annual Review Fluid Mechanics*, 45:115–145, 2013.

[68] J. W. Wright. Backscattering from Capillary Waves with Application to Sea Clutter. *IEEE Transaction on Antennas and Propagation*, AP-14, No. 6:749–754, 1966.

[69] P. W. Vachon, R. B. Olsen, and C. E. Livingstone. Airborne SAR Imagery of Ocean Surface Waves Obtained During LEWEX: Some Initial Results. *IEEE Transactions on Geoscience and Remote Sensing*, 26, No. 5:548–561, 1988.

[70] A. D. Rozenberg, D. C. Quigley, and W. K. Melville. Labratory Study of Polarized Scattering by Surface Waves at Grazing Incidence: Part I- Wind Waves. *IEEE Transactions on Geoscience and Remote Sensing*, 33, No. 4:1037–1046, 1995.

[71] R. Romeiser and W. Alpers. An Improved Composite Surface Model fro the Radar Backscattering Cross Section of the Ocean Surface 1. Theory of the Model and Optimization/Validation by Scatterometer Data. *Journal of Geophysical Research*, 102, No. C11:25,237–25,250, 1997.

[72] R. K. Raney and P. W. Vachon. Phase versus Orbital Velocity in SAR Wave Imaging: Paradox Lost. In *Proceedings of IGARSS '88 Symposium*, 1988.

[73] M.S. Longuet-Higgins. The Statistical Analysis of a Random, Moving Surface. *Philosophical Transactions of the Royal Society of London. Series A, Mathematical and Physical Sciences*, 249, No. 966:321–387, 1957.

[74] N. J. Higham. *Accuracy and Stability of Numerical Algorithms, Second Edition*. SIAM, 2002.

[75] M. Marom. *Interferometric Synthetic Aperture Radar Imaging of Ocean Surface Currents and Wavefields*. PhD thesis, Naval Postgraduate School, 1990.

[76] C. H. Gierull. Digital Channel Balancing of Along-Track Interferometric SAR Data. Technical report, Defence R&D Canada, 2003.

[77] P. A Rosen, S. Hensley, I. R. Joughin, F. K. Li, S. N. Madsen, E. Rodriguez, and R. M. Goldstein. Synthetic Aperture Radar Interferometry. *Proceedings of the IEEE*, 88:333–382, 2000.

[78] U. Nickel. On the Influence of Channel Errors on Array Signal Processing Methods. *AEÜ*, 47:209–219, 1993.

[79] M. Abramowitz and I. A. Stegun. *Handbook of Mathematical Functions with Formulas, Graphs and Mathematical Tables*. Dover, 1964.

[80] M. Lefebvre. *Applied Probability and Statistics*. Springer, 2006.

[81] E. J. Hinch. *Perturbation Methods*. Cambridge University Press, 1991.

[82] T. Kato. *Perturbation Theory for Linear Operators*. Springer, 1980.

[83] L. Rosenberg and N. J. Stacy. Analysis of Medium Grazing Angle X-band Seaclutter Doppler Spectra. In *Radar Conference 2008*, 2008.

[84] L. Shemer and M. Marom. Estimates of Ocean Coherence Time by an Interferometric SAR. *Int. J. Remote Sensing*, 14:3021–3029, 1993.

[85] I. C. Sikaneta and C. Gierull. On the Determination of Temporal Reflectivity Fading with Multi-Aperture SAR. In *European Conference on Synthetic Aperture Radar (EUSAR), Dresden*, 2006.

[86] K. Hasselmann et .al. Measurements of Wind-Wave Growth and Swell Decay during the Joint North Sea Wave Project (JONSWAP). *Zusatzheft zur Deutschen Hydrographischen Zeitschrift*, A:1–95, 1973.

[87] S. J. Frasier and A. J. Camps. Dual-Beam Interferometry for Ocean Surface Current Vector Mapping. *IEEE Transactions on Geoscience and Remote Sensing*, 39, No. 2:401–413, 2001.

[88] R. C. DiPietro. Extended Factored Space-Time Processing for Airborne Radar Systems. *Signnals, Systems and Computers*, 1:425–430, 1992.

[89] Tom Rother. *Electromagnetic Wave Scattering on Nonspherical Particles*. Springer, 2009.

[90] D. R. Thompson. Calculation of Radar Backscatter Modulations From Internal Waves. *Journal of Geophysical Research*, 93, No. C10:12,371–12,380, 1988.

[91] L. C. Rogers. Derivatives of Eigenvalues and Eigenvectors. *AIAA Journal*, 8, No. 5:943–944, 1970.

[92] D. V. Murthy and R. T. Haftka. Derivatives of Eigenvalues and Eigenvectors of a General Complex Matrix. *International Journal for Numerical Methods in Engineering*, 26:293–311, 1988.

[93] R. B. Nelson. Simplified Calculation of Eigenvector Derivatives. *AIAA Journal*, 15, No. 9:1201–1205, 1976.